

PEOPLE'S DEMOCRATIC REPUBLIC OF ALGERIA

MINISTRY OF HIGHER EDUCATION

AND SCIENTIFIC RESEARCH

UNIVERSITY CONSTANTINE1

FACULTY OF EXACT SCIENCES

DEPARTMENT OF PHYSICS

Order N°:

Re:

Dissertation Submitted in Partial Fulfillment of Requirements for the Degree of
Doctorate LMD

In Physics

Specialty: **Science of Materials**

Option: **Thin Films and interface**

THEME

**Study of ZnO nanorods decorated by Cu₂O, CdS and PbS for
Photoelectrochemical Application**

Submitted by: LAKEHAL SIHEM

To be defended on: 11/12/ 2014

Committee members:

Chairman:	A. BOUABELOU	Prof. University- Constantine 1
Reporter :	S. ACHOUR	Prof. University- Constantine 1
Examiners :	S. ZERKOUT	Prof. University- Skikda
	A. NOURI	Prof. University- Oum elbouagui
	M. BOUDISSA	Prof. University- Sétif

Acknowledgement

With deep sense of gratitude, I wish to express my sincere thanks to my guides Pr. S. Achour of The Department of Physics, Ceramic Laboratory of Constantine 1, for his excellent guidance and support throughout the work I received very useful and excellent academic training from him, which has stood in good stead while writing this thesis. His unique inimitable style has left an indelible impression on me. His constant encouragement, help and review of the entire work during the course of the investigation are invaluable. Nevertheless, it helped me acquire and develop some of the skills and intricacies of good independent research.

I must express my deep appreciation and gratitude to Pr A. Bouabelou Professor at Constantine1 university, Pr A. Nouiri Professor at Oum el-Bouagui university, Pr M.S. Zerkout Professor at Skikda university and Pr M. Boudissa Professor at Sétif university.

My sincere thanks to Mr Claudio Ferrari from IMEM Institute, Parma Italy, and all the Institute members for their encouragement and kind help extended toward me.

Last but not the least I am very thankful to my batch mates and all my hall mates for their immense cooperation without whom my stay here would not have been memorable.

Finally, I would like to share this moment of happiness with my family members for whom I do what I do.

LAKEHAL SIHEM

Contents

General Introduction.....	1
---------------------------	---

Chapter:1 Generality

1. Introduction.....	4
2. Nanotechnology	4
3. Nanomaterials	4
4. Semiconductor nanomaterials.....	5
4.1 Electronic properties	5
A. Band Gap Tuning and Quantum Confinement.....	5
✚ Density of states	5
✚ Exciton	6
B. Quantum Confinement in Quantum Dots	6
4.2 Luminescence Properties	7
4.3 General applications of semiconductor nanocrystal.....	8
a. Biological Applications	8
b. Energy Storage	8
c. Fuel Cells	8
d. Computing	8
e. Lubricants.....	9
f. The design of lighter stronger materials	9
g. Visual Displays	9

f. Plastic and Colloids.....	9
5. One Dimensional Nanostructures	9
5.1 Core-Shell Structure	10
6. Materials and properties	10
6.1 Zinc Oxide	10
6.2 Copper (II) Oxide	12
6.3 Lead and Cadmium Sulfide	14
• Properties of bulk lead sulphide (PbS)	14
• Application.....	15
• Properties of bulk cadmium sulphide (CdS)	16
• Application.....	15

Chapter 2: The Photoelectrochemical cells

1. The Photoelectrochemical Cell	21
2. Semiconducting Photoelectrode Materials	21
3. Charge Carriers and Doping	21
4. Defect Chemistry	23
5. Space Charges and Band Bending	23
5.1 Potential Distribution in the Depletion Layer	23
6. The Semiconductor–Liquid Junction	23
6.1 The Semiconductor/Electrolyte Interface	23
6.2 Applying a Bias Potential	24

6.3 The Flat Band Potential	24
6.4 Surface and Interface States	24
7. The Photoelectrochemical Cell under Operating Conditions	25
7.1 The Quasi-Fermi Level	25
7.2 Photocurrent–Voltage Characteristics.....	26
7.3 Reaction Mechanisms	27
7.4 Photocorrosion	27
8. Nanostructured Electrodes	28

Chapter 3: Synthesis and Characterization

1.Introduction	30
----------------------	----

I.Elaboration Techniques

2.Hydrothermal/Solvothermal Synthesis	30
3.Spin-Coating process	31
Ø Dip coating	31
Ø Sol-gel film formation.....	32

II. Characterization Techniques

4. Scanning Electron Microscopy	33
5. X-ray diffraction	35
6. Atomic force microscope	36
7.Transmission Electron Microscopy	36

8. Raman Spectroscopy	37
9. UV/VIS Spectroscopy	39
10. Cathodoluminescence Spectroscopy (CL)	39

Chapter 4: Experimental

1. Introduction	41
2. Synthesis of ZnO nanorods	41
2.1 Substrate pre-treatment	41
2.1.1 Substrate pre-cleaning.....	41
2.1.2 Seed layer for ZnO nanostructures	41
2.2 ZnO hydrothermal growth	42
2.2.1 Synthesis of ZnO nanorods	43
2.2.2 Synthesis of ZnO core-shell and flowers-like	43
3. Synthese of Lead Sulfide (PbS) and Cadmium Sulfide (CdS) nanoparticles	44
4. Synthesis of silver (Ag) nanoparticles	44
5. Synthesis of Cu ₂ O nanostructures	45
6. Synthesis of heterostructures	45
6.1 Synthesis of ZnO/CuO film	45
6.2 Synthesis of ZnO/Cu ₂ O film	45
6.3 Synthesis of ZnO/PbS core-shell nanorods	45
6.4 Synthesis of ZnO/CdS nanorods core shell.....	46

Chapter 5: Results and Discussion

1. Introduction	47
2. Characterization of ZnO nanorods.....	47
3.Characterization of Lead Sulfide and Cadmium Sulfide nanoparticles	54
4. Characterization of silver (Ag) nanoparticles	58
5. Characterization of Cu ₂ O nanostructures	61
6. The synthesis of heterostructures	62
6.1 Characterization of ZnO/CuO film	63
6.2 Characterization of ZnO/Cu ₂ O	69
6.2 Characterization of ZnO/PbS core shell nanorods	71
6.4 Characterization of ZnO/CdS nanorods core shell.....	78
7.Photoelectrochemical Cells.....	82
Conclusions	84
General Conclusion	85
Reference.....	87

GENERAL INTRODUCTION

During the last few decades, nanomaterials have been the subject of extensive interest because of their potential use in a wide range of fields like, optoelectronics, catalysis, sensing and photoelectronchemical applications etc... The physical and chemical properties of nanomaterials can differ significantly from their bulk counterpart because of their small size. In general, nanomaterials comprised novel properties that are typically not observed in their conventional, bulk counterparts. Nanomaterials have a much larger surface area to volume ratio than their bulk counterparts, which is one of the bases of their novel physical and/or chemical properties. Nanomaterials are classified into one-dimensional (1D), two-dimensional (2D) and three dimensional (3D). At present, research on nanomaterials is intensified and is expanding rapidly. In addition, metal oxide nanomaterials have drawn a particular attention because of their excellent structural flexibility combined with other attractive properties. These metal oxides nanostructures not only inherit the fascinating properties from their bulk such as piezoelectricity, chemical sensing, and photodetection, but also possess unique properties associated with their highly anisotropic geometry and size confinement [1]. The combinations of the new and the conventional properties with the unique effects of nanostructures make the investigation of novel metal oxide nanostructures a very important issue in research and development both from fundamental and industrial standpoints. Among the various metal oxides, zinc oxide (ZnO) possessed a considerable attention due to its unique properties and applications. In particular, ZnO nanostructures (NSs) are of intense interest since they can be grown by a variety of methods with different morphologies. Among the different growth methods, the hydrothermal method is a low temperature, simple, inexpensive and environment friendly method. These are all factors which further contribute to the resurgent attention in ZnO. Specifically, one-dimensional ZnO nanorods (NRs) amongst other nanostructures are attractive components for manufacturing nanoscale electronics and photonic devices as well as their biomedical applications because of their interesting chemical and physical properties [2, 3]. Also ZnO NRs can easily be grown on a variety of substrates like metal surface, semiconductors, glass, plastic and disposable paper substrates etc. [4-7]. Furthermore, direct wide band gap ~ 3.37 eV and relatively large excitonic binding energy ~ 60 meV of ZnO along with many radiative deep level defects, makes ZnO attractive for its emission

tendency in blue/ultraviolet and full color lighting [8, 9]. To utilize these properties of ZnO which is a wide band gap, in several applications, another narrow band gap material such as Lead sulfide (PbS) and Cadmium sulfide (CdS) which are p and n-type respectively, can be a better choice to use with ZnO NRs to fabricate a flexible device that utilizes the properties of both materials for large area lighting and display application [10, 11] and photoelectrochemical cells. On the other hand, natural abundance of copper (II) oxide (CuO or Cu₂O) as well as its low production cost, good electrochemical and catalytic properties makes the copper oxide to be one of the best materials for various applications. CuO also has a variety of nanostructures and can be grown using low temperature aqueous chemical method. It is one of the most important catalysts and is widely used in environmental catalyst.

Objective and outline of this thesis

The objective of this thesis is to synthesize metal oxide semiconductor nanostructures and utilize them for photoelectronchemical applications. For the ease of gathering all presented work, the thesis is divided into parts:

- i) Synthesis of ZnO nanorods and the quantum dots of CdS, PbS, CuO-Cu₂O and Ag.

The morphology, crystal structure and crystallinity of the nanostructures were monitored by using scanning electron microscope (SEM), transmission electron microscope (TEM), x-ray diffraction (XRD) and optical properties (Raman, UV-vis and Photoluminescence (PL) spectroscopy).

- ii) Fabrication of p-n heterostructure of ZnO NRs/CdS or PbS or Cu₂O-CuO on flexible substrates (ITO or FTO).

ZnO nanorods semiconductor have already shown higher surface area, tubular structure with higher charge carriers generation and transfer efficiency. In order to improve the performance for photoelectrochemical applications of ZnO nanorods synthesized by the hydrothermal method, modifications with another semiconductor, narrow bandgap of CdS, PbS and Cu₂O-CuO nanoparticles, which may expand the light absorption range to the visible region, were deposited on ZnO nanorods arrays by exchange ion method to form core-shell p-n heterojunction.

- iii) Photoelectrochemical application

outline

The outline of this thesis is as follow: the general introduction contains fundamental information of semiconductor nanomaterial and some basic properties of ZnO, CuO, CdS and PbS studied in the this work. Chapter 2 provides background information on photoelectrochimecal process. The synthesis of ZnO, CdS, PbS, CuO and their composite nanostructures together with characterization is the subject of chapter 3 and 4. Their characterization results, using different techniques, and their applications were demonstrated in the chapter 5 and finally the conclusion of whole work and possible future prospects.

Chapter 1: Generality

1. Introduction

In this chapter, we will introduce background information and general concepts in nanomaterials. A few questions will be answered through the literature review. Some basic properties of ZnO nanorods, PbS, Cds, Cu_xO and Ag nanoparticles were presented. In the end of this chapter, we will introduce the potential application of nanomaterials.

2. Nanotechnology

The concept of —nanotechnology² was first introduced in a famous talk given by Richard Feynman in 1959: —There's Plenty of Room at the Bottom—. In his talk, Dr. Feynman pointed out how scaling issues would affect many physical properties [12]. In the 1980s, Nano-based concepts had become more and more popular since there were some important nano-characterization instrumentation developments, which made it easier to study nanoscale materials. Since research on nanoscale materials became easier, nanotechnology has been expanding into several fields.

The properties, such as electronic, optical, and chemical characteristics of nanoscale materials are distinct from those of bulk materials [13].

3. Nanomaterials

Nanomaterials typically refer to the materials which have at least one dimension in nanometer scale (~ 0.1-100 nm). Because of their nanoscale, nanomaterials have relatively large surface area which might result in different properties from bulks. However, conductivity of nanomaterials sometimes can also be increased by doping with different elements [14].

4. Semiconductor nanomaterials

When the size of semiconductor materials reduces to nanoscale, their physical and chemical properties change dramatically, resulting in unique properties due to their large surface area or quantum size effect.

4.1 Electronic properties

One of the defining features of a semiconductor is the energy gap separating the conduction and the valence energy bands. The color of light emitted by the semiconductor material is determined by the width of the gap.

A. Band Gap Tuning and Quantum Confinement

Density of states

It is important here to introduce the concept of the density of states (DOS) as it helps to highlight the effect of quantum confinement on the electronic properties of a low dimensional system. The density of states of a particular system describes the density of available energy states per unit energy [15, 16]. The electron density of states, $g(E)$, for a three dimensional (3D) system of volume L^3 is directly proportion to the square root of the energy, i.e.:

$$g(E) = \frac{1}{2\pi^2} \left(\frac{2m^*}{\hbar^2}\right)^{3/2} \sqrt{E}, \dots\dots\dots(1.1)$$

so the electron can occupy a continuum of energy levels. Reducing the dimensionality of the system to 2D, e.g. for a quantum well where an electron is confined in one direction and free to move in the other two spatial dimensions, the DOS exhibits a step-like dependence. Each step in the DOS is described by:

$$g(E) = \frac{m^*}{\pi \hbar^2} \dots\dots\dots(1.2)$$

These equal height staircases correspond to the quantized electronic states in the direction of confinement. In 1D systems, where electron is only free to move along one direction, for example in nano-wires, the density of states resembles an array of spikes, each representing a quantized electronic state in the direction of confinement, i.e.

$$g(E) = \frac{1}{\hbar\pi} \sqrt{\frac{m^*}{2E}} \dots\dots\dots(1.3)$$

For a 0D system, such as quantum dots, where the electron is confined in the three spatial dimensions, the DOS is described by δ -functions. The electron confinement produces a series of discrete energy levels, which explain the atomic-like behavior of quantum dots and their unique optical and electrical properties.

 Exciton

In semiconductors, an electron-hole pair created by the absorption of a photon is known as an exciton. The energy required for the exciton creation is slightly lower than the material band gap energy due to the Coulomb interaction between the electron and hole. Eventually the exciton vanishes through electron-hole recombination. In a direct band gap semiconductor, a photon with energy higher than E_g is needed in order to create a free electron and a free hole. On the other hand, the phonon energy is subtracted from the energy threshold in an indirect band gap semiconductor where a phonon contribution is needed to fulfill the transition [15, 17]. The electron and hole in an exciton are held together by an attractive Coulomb interaction.

B. Quantum Confinement in Quantum Dots

The atomic-like behavior of QDs arise from the discrete energy levels that emerge from the electron confinement in the three spatial dimensions. Also, the confinement induces a shift of the optical absorption towards higher energies.

Confinement effects can be probed by optical experiments, e.g. by photoluminescence or absorption in single QDs or ensembles of QDs. Valuable information about the basic physics of a QD can be also extracted by modeling the system as a semiconductor sphere surrounded

by a matrix. Figure 1.1 sketches a single spherical QD, its capping matrix and the energy levels diagram [18].

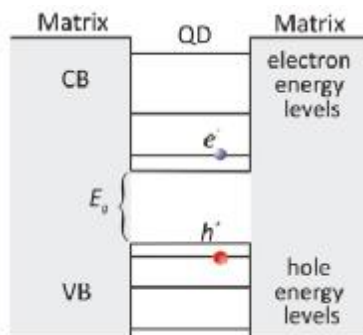


Figure 1.1 A schematic of a single colloidal QD with its surrounding matrix (capping ligands). The diagram on the right represents the potential well for each of the three spatial dimensions, and the quantized energy levels of electrons and holes in a QD.

4.2 Luminescence Properties

Luminescent properties i.e. emission color, quantum yield, luminescent lifetime and stability must be strictly controlled to realize a wide range of potential applications of the semiconductor nanocrystals.

The role of surface in determining the luminescence quantum yields of semiconductors is fundamental and has long been recognized and ascribed to the higher concentration of defects at the surface e.g. unsaturated bonds, ion vacancies, disorder due to adsorbed impurities, or uncommon oxidation states, which gives rise to high density mid-gap states acting as electron and hole states. The surface properties are expected to have large influence on the optical properties of the semiconductor nanocrystals because of the high surface to volume ratio. When a nanocrystal size is reduced such that the particle is essentially all the surface, the curvature of the surface is so high that virtually all the surface atoms have slightly different coordination or effective oxidation state [19-22].

In the case of nanorods, there are two additional factors that might further reduce the luminescence band edge states when compared to spherical nanocrystals. In nanorods, the surface-to-volume ratio is higher than in spheres and this increases the occurrence of surface trap states. In larger dots the increased delocalization of carriers reduces the overlap of the

electron and hole wave functions, lowering the probability of radiative combination. The delocalization of carriers should be particularly higher in nanorods, where they are free to move throughout the length of the rod thereby leading to reduced luminescence in nanorods.

4.3. General applications of semiconductor nanocrystal

a. Biological Applications

In order for the nanoparticles to function as biological labels or tags, the particles have to interact with the biological targets, which can be done through the attachment of a molecular coat or layer which acts as a bioinorganic interface. Antibodies, biopolymers or monolayers of small molecules that make nanoparticles compatible are examples of biological coatings.

b. Energy Storage

The fundamental pathways for enhancing the conversion efficiency can be accessed through photovoltaic cells composed of nanocrystal arrays, through the dispersion of nanoparticles in organic semiconductor polymer matrices or through nanocrystal sensitized TiO₂ and ZnO solar cells also known as Gratzel cells [23-25].

c. Fuel Cells

Nanotechnology offers different possibilities to increase the conversion efficiencies of fuel cells, in particular, within the ranges of catalysts, membranes and hydrogen storage, which in many cases is critical for the employment of fuel cell technology in space.

d. Computing

Techniques such as soft lithography and bottom-up approaches to forming nanoscale components by self-assembly could produce cheap and effective microscale circuits. Molecular electronics, with molecular switches and circuits only a few atoms wide, offers the possibility of

using molecular components in electronic devices, greatly reducing their size, although there are many practical issues to be addressed before this technique can be fully developed.

e. Lubricants

In mechanical systems much of the energy is required to overcome friction between surfaces. The use of nanoscale lubricants and high-precision surface engineering on a nanometer scale should substantially reduce the energy requirements. Reduction of the material content of products is a key issue for sustainability.

f. The design of lighter stronger materials

The design of lighter, stronger materials can also lead to savings in energy and raw materials, especially in the transport sector. Nanotechnology contributes to material design by altering the types of materials that can be produced.

g. Visual Displays

Visual displays can be made more efficient by using carbon nanotubes and band-gap engineering using nanostructured materials that optimize the emission spectrum of Light Emitting Diodes.

f. Plastic and Colloids

Nanoparticles are also used in colloids, which in turn are being used in sunscreens, printer ink, and paints. Zinc and titanium oxide sunscreens, for instance, use nanoparticles that are so small they do not scatter light, leaving the end product clear instead of white.

5. One Dimensional Nanostructures

In 1991, a Japanese researcher, Sumio Iijima, discovered nanotubes at NEC, which brought more attention to the one dimensional nanostructures due to their distinct properties

from bulks or three-dimensional (3D) materials [26]. These one dimensional nanostructures have diameters range from one nanometer to hundreds of nanometer. Nanorods and nanowires are all considered as one dimensional nanostructures, but nanorods generally have much smaller aspect ratio than nanorods.

5.1 Core-Shell Structure

Recently, core-shell nanorods have brought much attention because of the possibility to tune the properties of core nanocrystal with addition of the shell. By choosing appropriate core and shell materials, the emission wavelength can be tuned in a larger range than both of materials alone [27].

6. Materials and properties

ZnO is a wide bandgap material possessing many interesting properties and probably the richest family of nanostructures. Moreover, Cu_xO , CdS, PbS are a narrow bandgap materials and has been studied extensively. In this part we aim to narrate some properties of ZnO and Cu_xO , CdS, PbS in a comprehensive manner, as well as discuss the Ag quantum dots features which are used in this work.

6.1. Zinc Oxide

Zinc oxide (ZnO) is a metal oxide semiconductor with wurtzite structure under ambient condition. The wurtzite structure has hexagonal unit cell as shown in figure 1.2. In this crystal structure, two interpenetrating hexagonal-close-pack (hcp) sublattices are alternatively stacks along the c-axis. One sublattice consists of four Zn atoms and the other sublattice consists of four Oxygen O atoms in one unit cell; every atom of one kind is surrounded by four atoms of the other kind and forms a tetrahedron structure [28].

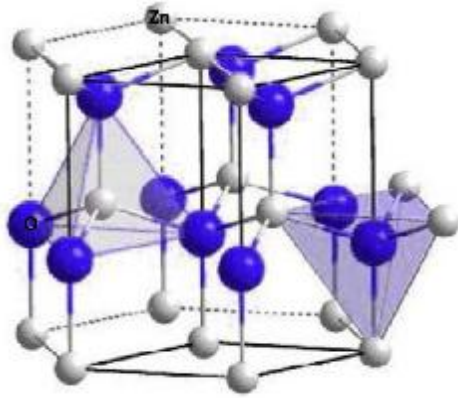


Figure 1.2. The hexagonal wurtzite structure of ZnO [reproduced from wikipedia].

ZnO commonly consists of polar (0001) and non-polar (10-10), (11-20) surfaces. The surface energy of the polar surface is higher than the non-polar surfaces and therefore the preferential growth direction of ZnO nanorods (NR) is along the $\langle 0001 \rangle$. Figure 1.3 shows the schematic diagram of a ZnO NR growing along the $\langle 0001 \rangle$ direction or along the c-axis.

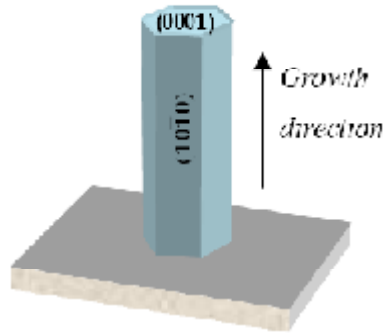


Figure 1.3 Schematic diagram of ZnO NR showing the growth direction.

The enormous interest of using ZnO in optoelectronic devices is due to its excellent optical properties. The direct wide band gap of ZnO ~ 3.4 eV is suitable for short wavelength optoelectronic applications, while the high exciton binding energy ~ 60 meV allows efficient excitonic emission at room temperature [29]. Moreover ZnO, in addition to the ultraviolet (UV) emission, emits covering the whole visible region i.e. containing green, yellow and red emission peaks [30-32]. The emission in the visible region is associated with deep level defects. Generally oxygen vacancies (V_o), zinc vacancies (V_{Zn}), zinc interstitials (Zn_i), and the incorporation of hydroxyl (OH) groups in the crystal lattice during the growth of ZnO are most common sources

of the defects related emission [33-35]. ZnO naturally exhibits n-type semiconductor polarity due to native defects such as oxygen vacancies and zinc interstitials. P-type doping of ZnO is still a challenging problem that is hindering the possibility of a p-n homojunction ZnO devices. Furthermore, the remarkable properties of ZnO like being bio-safe, bio-compatible, having high-electron transfer rates and enhanced analytical performance are suitable for intra/extra-cellular sensing applications [36-37]. Some basic physical parameters of ZnO at the room temperature are presented in the table 1.1.

Table 1.1 Some basic properties of wurtzite ZnO.

Property	Value	Reference
Lattice Parameters	a= b=3.25 Å c=5.21 Å	52, 55
Stable crystal structure	wurtzite	54
Density	5.606 gm/cm ³	52
Melting point	1975 °C	
Dielectric constant	8.66	54
Refractive index	2.008	52
Energy gap	3.4 eV, direct	52, 65
Exciton binding energy	60 meV	66
Effective mass	0.24 m _e /0.59 m _e	52
Electron/Hole		
Electron mobility	100-200 cm ² /Vs	53
Hole mobility	5-50 cm ² /Vs	
Bulk young modulus	111.2±4.7 GPa	67

6.2 Copper (II) Oxide

Copper (II) oxide (CuO) is another metal oxide semiconductor having narrow bandgap ~ 1.2 eV in bulk. CuO has monoclinic crystal structure as shown in figure 1.4, and belongs to the space group 2/m. The copper atom is coordinated by four oxygen atom in a square planer configuration [38]. It is intrinsically p-type semiconductor. CuO draw much attention since the

starting growth material is inexpensive and easy to get, and the methods to prepare these materials are of low cost [39].

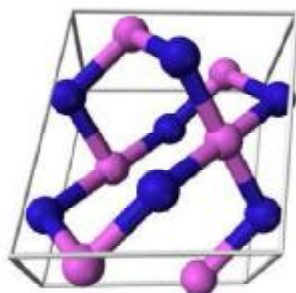


Figure 1.4 The monoclinic crystal structure of CuO [reproduced from wikipedia].

CuO nanostructures (NSs) have stimulated intensive research due to their high surface area to volume ratio. CuO NSs are a good candidate for sensing owing to its exceptional electrochemical activity and the possibility of promoting electron transfer at low potentials [40]. Due to the photoconductive and photochemical properties, CuO NSs are also promising materials for the fabrication of solar cells [41,42]. CuO based materials are well known with regard to their high temperature superconductivity and the relatively huge magneto-resistance [43-45]. Additionally, this compound is well-known for its excellent performance as a sensing material for hazardous gas detection and as negative electrode in lithium ions batteries [38-40]. CuO is very important from the standpoint of the catalytic usage and the morphology affects the properties of a catalyst in general [46]. It is therefore significant to synthesize novel sizes and shapes of the CuO NSs and to further improve its application as a catalyst. Some of the physical features of CuO are summarized in table 1.2.

Table 1.2 Some basic properties of CuO at room temperature.

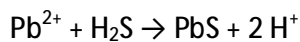
Property	Value	Reference
Lattice parameters	a=4.68 Å b=3.42 Å c=5.13 Å	72
Crystal structure	Monoclinic	73
Density	6.32 g/cm ³	74
Melting point	1134 °C	74
Dielectric constant	18.1	74
Refractive index	1.4	74
Energy gap	1.2 eV, direct	75
Hole mobility	0.1-10 cm ² /Vs	74

6.3 Lead and Cadmium Sulfide

- Properties of bulk lead sulphide (PbS)

Lead(II) sulfide (also spelled *sulphide*) is an inorganic compound with the formula PbS. It finds limited use in electronic devices. PbS, also known as galena, is the principal ore, and most important compound of lead.

Addition of hydrogen sulfide or sulfide salts to a solution of lead ions gives a poorly soluble black product consisting of PbS:



The equilibrium constant for this reaction is 3×10^6 M.[47] This reaction, which entails a dramatic color change from colourless or white to black, was once used in qualitative inorganic analysis. The presence of hydrogen sulfide or sulfide ions is still routinely tested using "lead acetate paper." Table 1.3 summarizes key properties of bulk PbS.

Table 1.3 Electronic properties of bulk PbS.

E_g (Energy gap)	0.286 eV at 4.2K 0.420 eV at 300K
$\frac{\partial E}{\partial T}$	+0.52 meV/K for $T = 100 - 400$ K
E_b (bulk exciton binding energy)	3.968 meV (calculated)
m_e^* (electron effective mass)	0.080 m_0
m_h^* (hole effective mass)	0.075 m_0
R_{ex} (exciton Bohr radius)	20 nm
$\epsilon_r(0)$ (dielectric constant)	169
$\epsilon_r(\infty)$	17

Pb^{++} and S^{--} ions occupy the lattice sites in the rock-salt crystal structure alternatively [13]. Each Pb atom is surrounded by 6 atoms of S, which are arranged at the corners of the surrounding octahedron and vice versa. The PbS lattice is shown in Figure 1.12a. The Bravais lattice has a fcc Brillouin zone with a Pb ion at (0 0 0) and a S ion at (1/2, 1/2, 1/2). Figure 2.2a shows the first Brillouin zone. The highly symmetrical points of the lattice are denoted in the graph as white circles. Γ is the centre of the Brillouin zone, while L is the centre of an hexagonal face. Dashed and solid lines represent the main directions and vectors in K space.

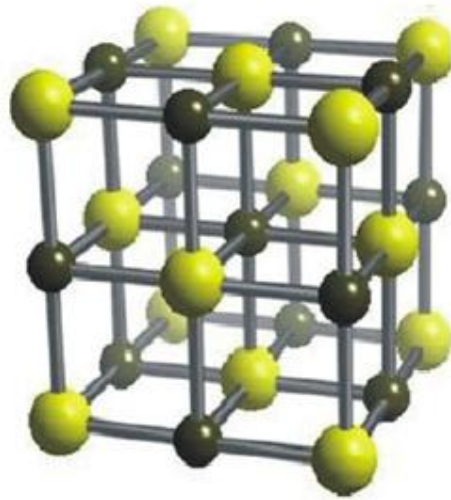
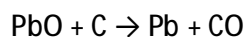
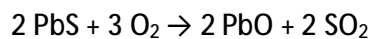


Figure 1.5 Rock salt crystal structure.

Like the related materials PbSe and PbTe, PbS is a semiconductor.[48] In fact, lead sulfide was one of the earliest materials to be used as a semiconductor.[49] Lead sulfide crystallizes in the sodium chloride motif, unlike many other IV-VI semiconductors.

Since PbS is the main ore of lead, much effort has focused on its conversion. A major process involves smelting of PbS followed by reduction of the resulting oxide. Idealized equations for these two steps are:[50]



The sulfur dioxide is converted to sulfuric acid.

- Application

PbS was once used as a black pigment, but current applications exploit its semiconductor properties, which have long been recognized.[51] PbS is one of the oldest and most common detection element materials in various infrared detectors. As an infrared detector, PbS functions as a photon detector, responding directly to the photons of radiation, as opposed to

thermal detectors, which respond to a change in detector element temperature caused by the radiation.

A PbS element can be used to measure radiation in either of two ways: by measuring the tiny photocurrent the photons cause when they hit the PbS material, or by measuring the change in the material's electrical resistance that the photons cause. Measuring the resistance change is the more commonly used method.

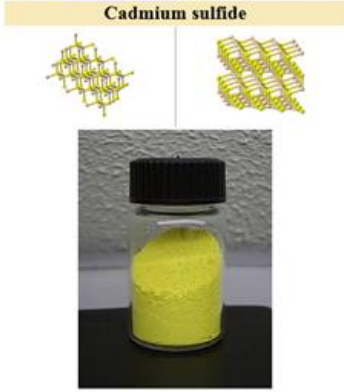
At room temperature, PbS is sensitive to radiation at wavelengths between approximately 1 and 2.5 μm . This range corresponds to the shorter wavelengths in the infra-red portion of the spectrum, the so-called short-wavelength infrared (SWIR). Only very hot objects emit radiation in these wavelengths.

Cooling the PbS elements, for example using liquid nitrogen or a Peltier element system, shifts its sensitivity range to between approximately 2 and 4 μm . Objects that emit radiation in these wavelengths still have to be quite hot—several hundred degrees Celsius—but not as hot as those detectable by uncooled sensors. Other compounds used for this purpose include indium antimonide (InSb) and mercury-cadmium telluride (HgCdTe), which have somewhat better properties for detecting the longer IR wavelengths. The high dielectric constant of PbS leads to relatively slow detectors (compared to silicon, germanium, InSb, or HgCdTe).

- *Properties of bulk cadmium sulphide (CdS)*

Cadmium sulfide is the inorganic compound with the formula CdS. Cadmium sulfide is a yellow solid [88]. It occurs in nature with two different crystal structures as the rare minerals greenockite and hawleyite, but is more prevalent as an impurity substituent in the similarly structured zinc ores sphalerite and wurtzite, which are the major economic sources of cadmium. As a compound that is easy to isolate and purify, it is the principal source of cadmium for all commercial applications [52].

Properties	
<u>Molecular formula</u>	CdS
<u>Molar mass</u>	144.48 g mol ⁻¹
<u>Appearance</u>	Yellow-orange to brown solid.
<u>Density</u>	4.826 g/cm ³ , solid.
<u>Melting point</u>	1,750 °C (3,180 °F; 2,020 K) 10 MPa
<u>Boiling point</u>	980 °C (1,800 °F; 1,250 K)
<u>Solubility in water</u>	insoluble ^[1] soluble in acid
<u>Solubility</u>	very slightly soluble in <u>ammonium hydroxide</u>
<u>Refractive index</u> (n _D)	2.529
Structure	
<u>Crystal structure</u>	Hexagonal, Cubic



The figure shows two ball-and-stick models of cadmium sulfide (CdS) crystal structures: a hexagonal structure on the left and a cubic structure on the right. Below these models is a photograph of a small glass vial with a black cap, containing a bright yellow powder, which is cadmium sulfide.

Figure 1.6 Some basic properties of CdS at room temperature.

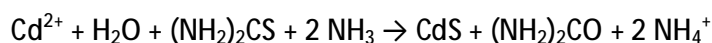
- *Production*

Cadmium sulfide can be prepared by the precipitation from soluble cadmium (II) salts with sulfide ion and this has been used in the past for gravimetric analysis and qualitative inorganic analysis [53]. The preparative route and the subsequent treatment of the product, affects the polymorphic form that is produced (i.e., cubic vs hexagonal). It has been asserted that chemical precipitation methods result in the cubic zinc-blende form [54].

Pigment production usually involves the precipitation of CdS, the washing of the precipitate to remove soluble cadmium salts followed by calcination (roasting) to convert it to the hexagonal form followed by milling to produce a powder [55]. When cadmium sulfide selenides are required the CdSe is co-precipitated with CdS and the cadmium sulfoselenide is created during the calcination step [55].

- *Routes to thin films of CdS*

Thin films of CdS are components in some photoresistors and solar cells. In the chemical bath deposition method, thin films of CdS have been prepared using thiourea as the source of sulfide anions and an ammonium buffer solution to control pH: [56]



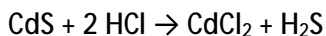
Cadmium sulfide can be produced using metalorganic vapour phase epitaxy and MOCVD techniques [56]. This process requires volatile cadmium and sulfur precursors. A common example is the reaction of dimethylcadmium with diethyl sulfide: [57]

Other methods include

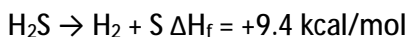
- Sol gel techniques [58].
- Sputtering [59].
- Electrochemical deposition [60].
- Spraying with precursor cadmium salt, sulfur compound and dopant [61].
- Screen printing using a slurry containing dispersed CdS [62].

Reactions

Cadmium sulfide is soluble in (actually degraded by) acids and this conversion has been investigated as a method of extracting the pigment from waste polymers e.g. HDPE pipes: [63]

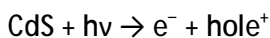


When sulfide solutions containing dispersed CdS particles are irradiated with light hydrogen gas is generated: [64]

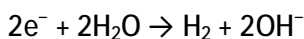


The proposed mechanism involves the electron/hole pairs created when incident light is absorbed by the cadmium sulfide [65] followed by these reacting with water and sulfide: [64]

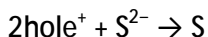
Production of an electron hole pair



Reaction of electron



Reaction of hole



- *Structure and physical properties*

Cadmium sulfide has, like zinc sulfide, two crystal forms; the more stable hexagonal wurtzite structure (found in the mineral Greenockite) and the cubic zinc blende structure

(found in the mineral Hawleyite). In both of these forms the cadmium and sulfur atoms are four coordinate [102]. There is also a high pressure form with the NaCl rock salt structure [66].

Cadmium sulfide is a direct band gap semiconductor (gap 2.42 eV [65]). The magnitude of its band gap means that it appears coloured [52].

As well as this obvious property others properties result:

- the conductivity increases when irradiated with light [88] (leading to uses as a photoresistor)
- When combined with a p-type semiconductor it forms the core component of a photovoltaic (solar) cell and a CdS/Cu₂S solar cell was one of the first efficient cells to be reported (1954) [67], [68].
- When doped with for example Cu⁺ ("activator") and Al³⁺ ("coactivator") CdS luminesces under electron beam excitation (cathodoluminescence) and is used as phosphor [69].
- Both polymorphs are piezoelectric and the hexagonal is also pyroelectric [71].
- Electroluminescence [72].
- CdS crystal can act as a solid state laser [73], [74].

Ø Applications

CdS is predominantly used as a pigment. About 2000 tons are produced annually [75].

CdS and cadmium selenide are used in manufacturing of photoresistors (light dependent resistors) sensitive to visible and near infrared light.

In thin-film form, CdS can be combined with other layers for use in certain types of solar cells [76]. CdS was also one of the first semiconductor materials to be used for thin-film transistors (TFTs) [77]. However interest in compound semiconductors for TFTs largely waned after the emergence of amorphous silicon technology in the late 1970s. Thin films of Cadmium Sulfide can be piezoelectric and have been used as transducers which can operate at frequencies in the GHz region.

- *Pigment*

CdS is known as cadmium yellow [52] (CI pigment yellow 37 [78]). By adding varying amounts of selenium as selenide, it is possible to obtain a range of colors, for example CI pigment orange 20 and CI pigment red 108 [78]. Synthetic cadmium pigments based on cadmium sulfide are valued for their good thermal stability, light and weather fastness, chemical resistance and high opacity [55], but with

problems of biocompatibility when used as colors in tattoos [79]. The general commercial availability of cadmium sulfide from the 1840s led to its adoption by artists, notably Van Gogh, Monet (in his London series and other works) and Matisse (Bathers by a river 1916–1919) [80]. The presence of cadmium in paints has been used to detect forgeries in paintings alleged to have been produced prior to the 19th century [81]. CdS is used as pigment in plastics [81].

Chapter 2:

The Photoelectrochemical cells

1. The Photoelectrochemical Cell

The main component of the PEC cell is the semiconductor, which converts incident photons to electron-hole pairs. These electrons and holes are spatially separated from each other due to the presence of an electric field inside the semiconductor. The photogenerated electrons are swept toward the conducting back contact, and are transported to the metal counter-electrode via an external wire. At the metal, the electrons reduce water to form hydrogen gas.

2. Semiconducting Photoelectrode Materials

Some of the key requirements for a semiconductor photoelectrode are efficient absorption of visible light and good charge transport. It is not easy to determine these parameters from an experiment on a particular material.

The bonding in metal oxide semiconductors is very different in nature. Since oxygen has a much higher electronegativity than any metal, the valence electrons are either fully or partially transferred from the oxygen to the metal ion. The bonding character of metal oxides is therefore highly polar or even ionic.

3. Charge Carriers and Doping

Semiconductors for practical applications are often doped, mainly with the aim to improve the conductivity. In metal oxide photoelectrodes, shallow donors and acceptors are almost always necessary because of the low intrinsic charge carrier mobilities. The conductivity of the

material is given by $\sigma = n_e\mu_e + p_e\mu_h$, so increasing n or p will compensate for a small value of μ_e or μ_h .

The extra valence electron introduced by the donor atom is loosely bound to the donor nucleus, and can be excited to the conduction band where it then contributes to the conductivity. Conversely, holes in acceptor-type dopants can be excited to the valence band. Since a hole is equivalent to a missing electron, one can also picture this as an electron being excited from the valence band into the energy level of the acceptor species.

4. Defect Chemistry

Semiconducting photoelectrodes are almost always doped to improve their properties. In most cases, the aim is to enhance the n- or p-type conductivity. Certain dopants may enhance the optical absorption of wide bandgap semiconductors [1], increase the minority carrier diffusion length [2, 3], or enhance the catalytic activity at the surface of the semiconductor [4]. Other dopants adversely affect the properties, for example, by introducing midgap bulk or surface states that act as recombination centers [5, 6]. In addition to foreign cation and anion dopants, native point defects are also usually present in the material.

5. Space Charges and Band Bending

In most semiconductor textbooks, the formation of a space charge is explained by a semiconductor being brought into contact with a metal or another semiconductor [7]. When both materials have different Fermi levels (i.e., electrochemical potentials), charge is transferred between them until an equilibrium is established.

In metal oxide semiconductors, a built-in electric field can even be formed at the surface without making contact with another solid. When a metal oxide is exposed to air, water molecules from the air can dissociatively adsorb at its surface, resulting in -OH surface termination. Since the symmetry of the bulk lattice is broken at the surface, these -OH groups form electronic surface states within the bandgap of the semiconductor.

The energy levels of these surface states are below the conduction band minimum, and free electrons from the bulk will occupy these levels. The ionized donors from which the free electrons originated will of course stay behind in the bulk, where they form a positive space

charge. An electric field now forms and the charge transfer from bulk to surface will continue until the potential barrier becomes too large for bulk electrons to cross. At this point, a dynamic equilibrium establishes at which no net electron transport takes place. The Fermi level at the surface is then located somewhere halfway the DOS of the surface state.

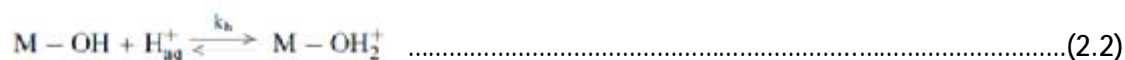
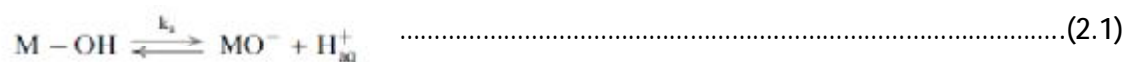
5.1 Potential Distribution in the Depletion Layer

The potential distribution and width of space charge depend on the amount of charges transferred to the surface and the density of shallow donors in the material.

The actual values of the dopant density and the depletion layer width can be determined by impedance measurements.

6. The Semiconductor–Liquid Junction

When a semiconductor is immersed in an aqueous solution, H^+ and OH^- ions in the solution will continuously adsorb and desorb from the surface. A dynamic equilibrium will be established, which can be described by the following protonation and deprotonation reactions:



The equilibrium of these reactions depends on the pH of the solution and the Bronsted acidity of the surface. Depending on these conditions, the net total charge adsorbed at the surface will be positive, zero, or negative. The pH at which the net adsorbed charge is zero is called the point of zero charge (PZC) of the semiconductor.

6.1. The Semiconductor/Electrolyte Interface

The charges at the surface consists of electrons (or holes) trapped in surface states. The counter charges are provided by ionized donors or acceptors in the solid, plus an accumulation of oppositely charged ions in the solution. Due to the large dipole moment of water, all ions in

the solution are surrounded by a solvation cloud of water molecules. This cloud prevents them from approaching the surface closer than a few Angstroms. The region between the specifically adsorbed ions and the closest ions in the solution is called the Helmholtz layer.

6.2. Applying a Bias Potential

The operation of a PEC cell can be influenced by applying an external bias potential to the semiconductor. When the bias is applied with respect to a reference electrode, the potential difference will be distributed over the space charge layer and the Helmholtz layer. These layers act as two capacitances in series [8]:

$$\frac{1}{C_{tot}} = \frac{1}{C_{SC}} + \frac{1}{C_H} \dots\dots\dots(2.3)$$

Applying a positive bias to an n-type semiconductor results in an increase of the depletion layer. For a p-type semiconductor, a negative bias is required to increase the depletion layer. The ability to change the band bending in a semiconductor electrode is immensely useful in the characterization of these materials.

6.3. The Flat Band Potential

The position of the band edges with respect to the redox potentials in the electrolyte is conveniently expressed by the so-called “flatband potential”, f_{FB} . As the word suggests, this is the potential that needs to be applied to the semiconductor to reduce the band bending to zero. It is important to realize that the flatband potential denotes the position of the Fermi level of the semiconductor with respect to the potential of the reference electrode. This means that f_{FB} is slightly below the conduction band edges, and that it accurately reflects the thermodynamic ability of an n-type semiconductor to reduce water to hydrogen.

6.4. Surface and Interface States

Illumination of a semiconductor can lead to a change in the flatband potential, even at constant pH. This can be explained by the presence of surface states that trap photogenerated

minority carriers [10]. The change in charge density at the interface (more specifically: the inner Helmholtz plane) results in a change in the Helmholtz potential and, therefore, the flatband potential. This is usually referred to as “unpinning of the band edges.”

The presence of surface states can also affect the band bending in the dark. If a high density of partially filled mono-energetic surface states is present, the Fermi level will be located somewhere halfway the surface state DOS. Any change in pH or applied potential will then be accommodated by a change in the occupation of this state and a concomitant change in the potential across the Helmholtz layer.

7. The Photoelectrochemical Cell under Operating Conditions

We now explore how the system behaves under illumination.

7.1. The Quasi-Fermi Level

Figure 2.20 shows the energy diagram of a PEC cell in the dark and under illumination. In this example, the $\text{H}_2\text{O}/\text{O}_2$ redox couple is assumed to be the most

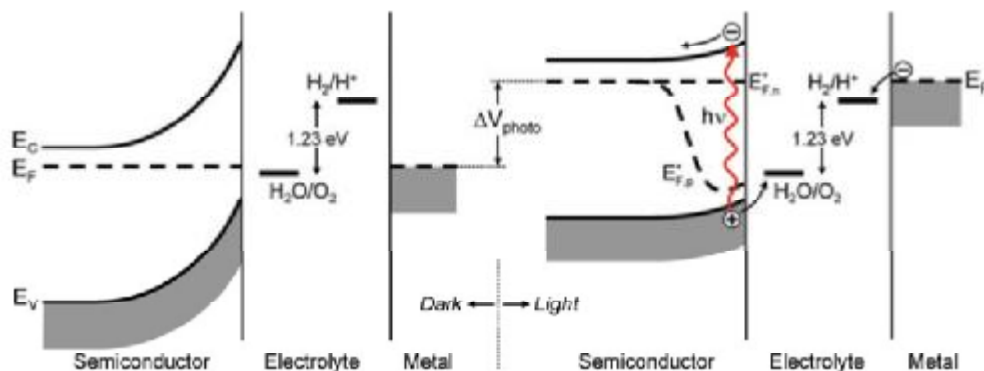


Figure 2.1 Band diagram for a PEC cell based on an n-type semiconducting photoanode that is electrically connected to a metal counter electrode; in equilibrium in the dark (left) and under illumination (right). Illumination raises the Fermi level and decreases the band bending. Near the semiconductor/electrolyte interface, the Fermi level splits into quasi-Fermi levels for the electrons and holes

active species and therefore dominates the electrochemical potential of the solution in the dark. The Fermi levels of the semiconductor and metal, which are electrically connected, adjust to a value close to E_{ox} . Upon illumination, electron–hole pairs are created and the Fermi level increases with ΔV_{photo} , the internal photovoltage. Since the system is no longer in equilibrium,

particularly in the SCR where the electrons and holes are generated, the use of a single Fermi level is no longer appropriate. Instead, the concept of quasi-Fermi levels is more useful. The quasi-Fermi levels are a direct measure of the concentration of electrons and holes at a certain point x in the semiconductor, and are defined as:

$$n = n_0 + \Delta n = N_C e^{-(E_C - E_{F,n}^*)/kT} \dots\dots\dots(2.4)$$

$$p = p_0 + \Delta p = N_V e^{-(E_{F,p}^* - E_V)/kT} \dots\dots\dots(2.5)$$

Here, n_0 and p_0 are the equilibrium carrier concentrations in the dark, and Δn and Δp are the additional carriers created by illumination. For an n-type semiconductor, $n = n_0 + \Delta n \approx n_0$ and $p = p_0 + \Delta p \approx \Delta p$ so that $E_{F,n}^*$ remains horizontal whereas $E_{F,p}^*$ departs from the bulk Fermi level in the active region. The quasi-Fermi level is often interpreted as a thermodynamic driving force.

7.2. Photocurrent–Voltage Characteristics

One of the most often used models of semiconductor photocurrent–voltage characteristics was reported by Gartner [9], who derived the following expression for the photocurrent in a semiconductor under reverse bias:

$$j_G = j_0 + e\Phi \left(1 - \frac{\text{Exp}(-\alpha W)}{1 + \alpha L_p} \right) \dots\dots\dots(2.6)$$

Here, Φ is the incident light flux, α is the absorption coefficient (assuming monochromatic illumination), W is the depletion layer width, L_p is the hole diffusion length, and j_0 is the saturation current density. The model assumes that there is no recombination in the SCR and at the interface.

Gartner’s model was improved by Reichman [9], who used more appropriate boundary conditions for his derivation of the total valence band photocurrent in an n-type semiconductor:

$$j_V = \frac{j_G - j_0 \text{Exp}\left(\frac{-eV}{kT}\right)}{1 + \frac{j_0}{j_V} \text{Exp}\left(\frac{-eV}{kT}\right)} \dots\dots\dots(2.7)$$

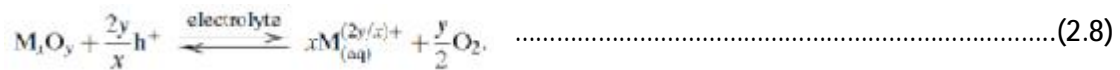
Here, J_V^0 is the hole transfer rate at the interface, and j_0 is the saturation current density, i.e., the hole current in the valence band at $x = W$ when $\Phi = 0$. η is the over-potential, which is defined as the difference between the applied potential and the open-circuit potential under illumination. Reichman's model includes the possibility of recombination in the SCR, which he showed could become important when the photovoltage becomes large enough for the bands to flatten.

7.3. Reaction Mechanisms

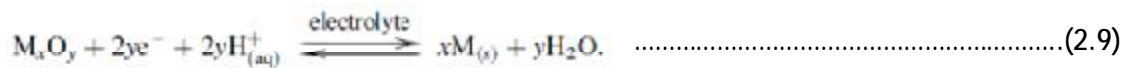
One of the main bottlenecks for water splitting is the oxidation half-reaction, which is a complicated process involving four separate electron transfer steps. Little is known about the exact molecular reaction mechanism of water oxidation on metal oxide surfaces.

7.4. Photocorrosion

Photocorrosion occurs when the photogenerated holes do not oxidize water, but the semiconductor itself. The general form of this anodic decomposition reaction can be written as



A well-known oxide that suffers from severe photocorrosion in aqueous environments is ZnO. For p-type oxides, cathodic photoreduction can lead to the formation of metal deposits:



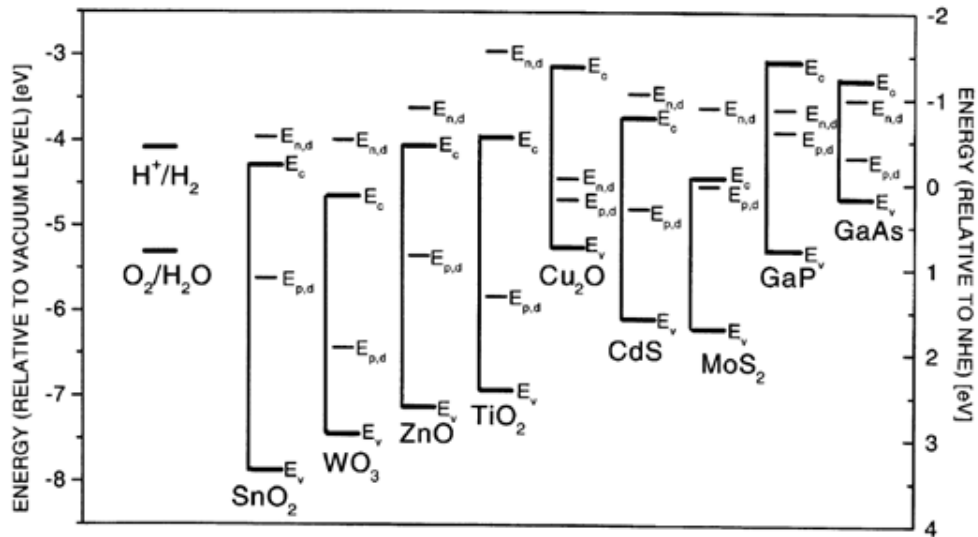
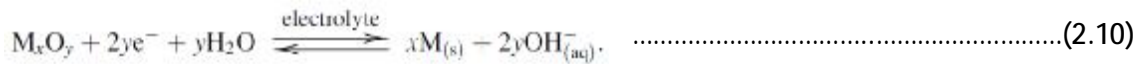


Figure. 2.2 Position of decomposition potentials of selected semiconductors. Reprinted from [70]

In an alkaline environment, the reaction can be written as



This has been observed for, e.g., Cu₂O. Alternatively, protons can enter the metal oxide lattice when free electrons are available at or near the surface, a process known as intercalation.

8. Nanostructured Electrodes

The most obvious advantage of nanostructured morphology is:

- The increase in specific surface area. The concomitant increase in the number of surface sites greatly enhances the overall charge transfer kinetics at the semiconductor/electrolyte interface.
- The shorter diffusion path lengths for the photogenerated charge carriers.

This is illustrated by the nanowire array photoelectrode shown in Fig. 2.3 (left).

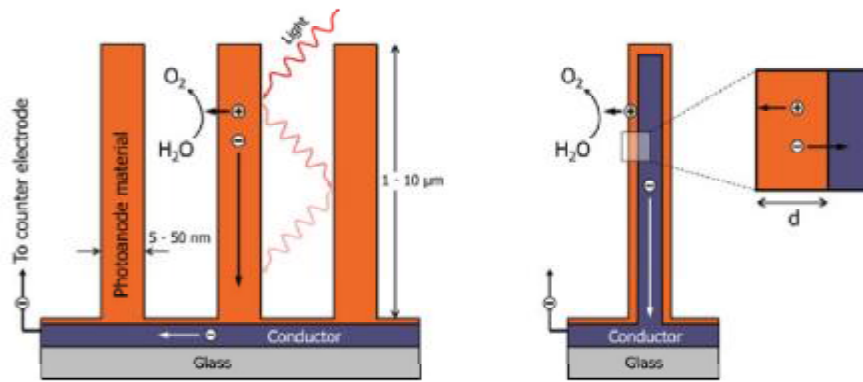


Figure 2.3 Nanowire array photoanode (left), and an array based on highly conducting nanowires coated with a thin photoanode film (right)

- The occurrence of quantum size effects. As first described by Brus in the early 1980s, spatial confinement of charge carriers to a volume that is less than their De Broglie wavelength results in a widening of the bandgap [11].

It should be noted that quantum size effects are difficult to induce in most metal oxides.

Chapter 3: Synthesis and Characterization

1. Introduction

The preparation procedure of the ZnO, Cu_xO, CdS, PbS and Ag nanostructures are described in this chapter. The sol-gel, dip-coating, polyol and hydrothermal methods were chosen for the growth of ZnO NRs and their composite nanostructures. After the growth, diverse characterization techniques were used to probe the morphology and structural aspects of the as grown nanomaterials. The techniques used during this work are: scanning electron microscope (SEM), transmission electron microscope (TEM), x-ray diffraction analysis (XRD), Raman spectroscopy, UV-vis, Photoluminescence (PL) .

I. Elaboration Techniques

2. Hydrothermal/Solvothermal Synthesis

A hydrothermal/solvothermal process can be defined as “a chemical reaction in a closed system in the presence of a solvent (aqueous and non aqueous solution) at a temperature higher than the boiling point of such a solvent”. [1-3] As a result, a hydrothermal/solvothermal process involves high pressures. The selected temperature (sub- or supercritical domains) is determined by the required reactions for obtaining the target-material. Because hydrothermal/solvothermal synthesis utilizes water/solvent under elevated pressures and temperatures to increase the solubility of a solid and to speed up reactions between solids, it provides another commonly used methodology for generating nanostructures. Hydrothermal/solvothermal reactions have been used in Materials Chemistry or Materials Science for developing soft processing in advanced inorganic materials. [4-6] Moreover, the interest of hydrothermal/solvothermal reactions in a large domain of applications (material synthesis, crystal growth, thin films deposition...) has promoted the development of new processes involving original technologies such as hydrothermal-electrochemical methods, [7-10] microwave-hydrothermal method [11-16].

3. Spin-Coating process

Spin Coating is a method to produce thin organic films that are uniform over large areas ($\varnothing \geq 30$ cm). There are four different stages of the process:

- Ø Deposition of the coating fluid onto the wafer or a flat substrate
- Ø The substrate is accelerated up to its final, desired, rotation speed
- Ø The substrate is spinning at a constant rate and fluid viscous forces dominate the fluid thinning behavior

The substrate is spinning at a constant rate and solvent evaporation dominates the coating thinning behavior. After evaporation of the whole solvent, a solid film is generated.

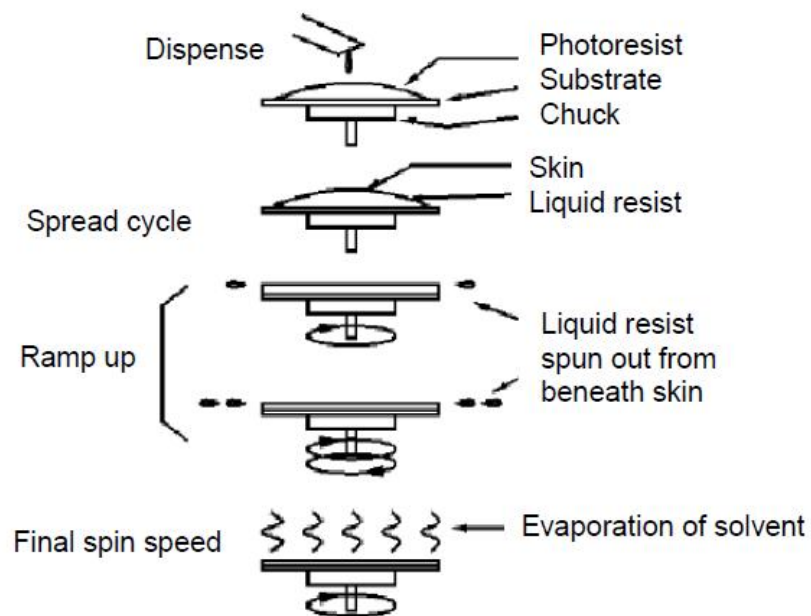


Figure 3.1 Scheme of the Spin Coating process.

Ø Dip coating

In dip coating, the substrate is normally withdrawn vertically from the liquid bath at a speed U_0 . The moving substrate entrains the liquid in a fluid mechanical boundary layer that

splits in two above the liquid bath surface, the outer layer returning to the bath [17]. Since the solvent is evaporating and draining, the fluid film terminates at a well-defined drying line.

When the receding drying line velocity equals U_0 , the process is steady state with respect to the liquid bath surface. A non-constant evaporation rate in the vicinity of the drying line (due to geometrical factors affecting the diffusion of solvent vapor from the liquid surface) results in a parabolic thickness profile [18]:

$$h(x) \propto x^{1/2} \dots\dots\dots(3.1)$$

where $h(x)$ is the film thickness as a function of position x below the drying line.

Ø Sol-gel film formation

Deposition of the inorganic film occurs as the entrained inorganic precursors (polymers or particles) are rapidly concentrated on the substrate surface by gravitational draining and evaporation often accompanied by continued condensation reactions. The increasing concentration forces the precursors into close proximity, causing reactive species to aggregate and gel, while repulsive particles appear to assemble into liquid- or crystal-like structures depending on the withdrawal rate. For reactive precursors a competition is established between solvent evaporation which compacts the structure and continuing condensation reactions which stiffen the structure, increasing its resistance to compaction. Unlike conventional bulk gel formation, the drying stage overlaps the aggregation-gelation stages, establishing only a brief time span (several seconds) for condensation reactions to occur. A common result is rather compliant structures that are collapsed at the final stage of drying by the capillary pressure P created by the liquid-vapor menisci as they recede into the film interior:

$$P = 2 \gamma_{LV} \cos(\theta) / r \dots\dots\dots(3.2)$$

where θ is the wetting angle and r is the hydraulic radius of the pore at the moment the meniscus recedes into the gel interior. Because r may be very small (less than 1.0 nm) [19], P may exceed 60 MPa even for liquids with low surface tensions such as ethanol. The draining and evaporation which accompany dipping cause the thickness h and volume fraction Φ of

solids of the depositing film to change continuously with distance above the liquid bath surface. Above the stagnation point where all fluid elements are moving upward, steady state conditions require that the solids mass in any horizontal slice must be constant:

$$h(x)\Phi(x) = \text{constant} \dots\dots\dots(3.3)$$

so Φ varies inversely with h in the thinning film. Since for a planar substrate there is a parabolic thickness profile [33] ($h(x) \sim x^{1/2}$), q should vary as $1/h \sim x^{-1/2}$ [18].

II. Characterization Techniques

After the preparation of the samples, different characterization techniques were used to investigate their structure and optical properties. Scanning electron microscope (SEM) and Transmission electron microscope (TEM) was used to get the morphology of the samples. An atomic force microscope (AFM) was utilized to detect the morphology of pretreated substrates. The detailed information about the structure of the samples can be obtained from XRD measurement. The optical properties were investigated by Cathodoluminescence (CL), Raman and UV-vis spectroscopy. In this section, we will briefly introduce all the techniques.

4. Scanning Electron Microscopy

The scanning electron microscope (SEM) is a type of electron microscope that images the sample surface by scanning it with a high-energy beam of electrons in a raster scan pattern. The electrons interact with the atoms to make the sample producing signals that contain information about the sample's surface topography, composition and other properties such as electrical conductivity. The types of signals produced by an SEM include secondary electrons, back scattered electrons (BSE), characteristic x-rays, light (cathodoluminescence), specimen current and transmitted electrons. These types of signal all require specialized detectors for their detection that are not usually all present on a single machine.

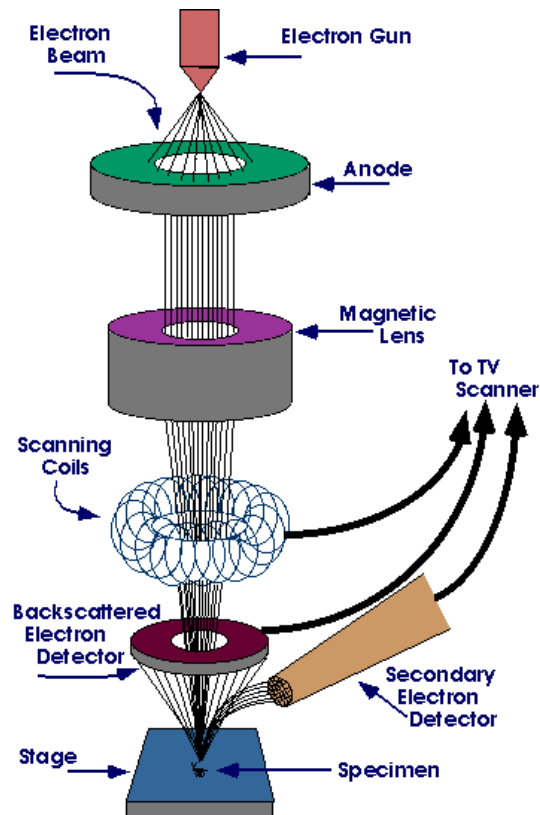


Figure 3.2 Schematic image of SEM

The schematic image of SEM is illustrated in figure 3.2 in order to show how it works. The SEM uses electrons instead of light to form an image. A beam of electrons is produced at the top of the microscope by heating of a metallic filament. The electron beam follows a vertical path through the column of the microscope. It makes its way through electromagnetic lenses which focus and direct the beam down towards the sample. Once it hits the sample, other electrons such as backscattered or secondary are ejected from the sample. Detectors collect the secondary or backscattered electrons, and convert them to a signal that is sent to a viewing screen similar to the one in an ordinary television, producing an image. The SEM gives information on the morphology of the surface of the sample, which implies that it is possible to determine if any growth has taken place.

The SEM images allow us to examine the diameter, length, shape and density of the ZnO nanostructures.

5. X-ray diffraction

X-rays are electromagnetic radiation of wavelength about 1 \AA (10^{-10} m), which is about the same size as an atom. When X-rays interact with a crystalline substance (phase), one gets a diffraction pattern. About 95% of all solid materials can be described as crystalline. Each crystalline solid has its unique characteristic X-ray diffraction (XRD) pattern which may be used as a "fingerprint" for its identification.

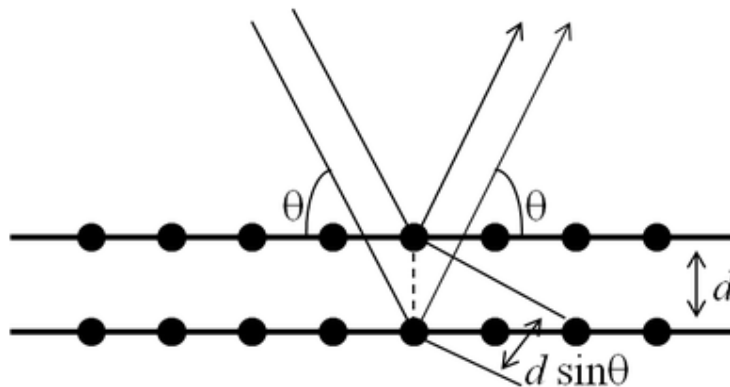


Figure 3.3. Reflection of X-rays from two planes of atoms in a solid.

A crystal lattice is a regular three-dimensional distribution (cubic, rhombic, etc.) of atoms in space. These are arranged so that they form a series of parallel planes separated from one another by a distance d , which varies according to the nature of the material. For any crystal, planes exist in a number of different orientation spacing. When a monochromatic X-ray beam with wavelength λ is projected onto a crystalline material at an angle θ , diffraction occurs only when the distance traveled by the rays reflected from successive planes differs by a complete number n of wavelengths, which leads to famous Bragg's Law:

$$n\lambda = 2d\sin(\theta)$$

where n is an integer 1,2,3.....(usually equal 1), λ is wavelength in angstroms (1.54 \AA for copper), d is interatomic spacing in angstroms, and θ is the diffraction angle in degrees. Where a mixture of different phases is present, the resultant diffractogram is formed by addition of the individual patterns. Based on the principle of X-ray diffraction, a wealth of structural, physical and chemical information about the material investigated can be obtained.

6. Atomic force microscope

The atomic force microscope (AFM) is a very high-resolution type of scanning probe microscope, with demonstrated resolution of fractions of a nanometer, more than 1000 times better than the optical diffraction limit.

The AFM consists of a microscale cantilever with a sharp tip (probe) at its end that is used to scan the specimen surface. The cantilever is typically silicon or silicon nitride with a tip radius of curvature on the order of nanometers.

The AFM works by scanning a fine ceramic or semiconductor tip over a surface much the same way as a phonograph needle scans a record. When the tip is brought into proximity of a sample surface, Vander Waals forces between the tip and the sample lead to a deflection of the cantilever. The magnitude of the deflection is captured by a laser that reflects at an oblique angle from the very end of the cantilever. A plot of the laser deflection versus tip position on the sample surface provides the resolution of the hills and valleys that constitute the topography of the surface. The AFM can work with the tip touching the sample (contact mode), or the tip can tap across the surface (tapping mode) much like the cane of a blind person.

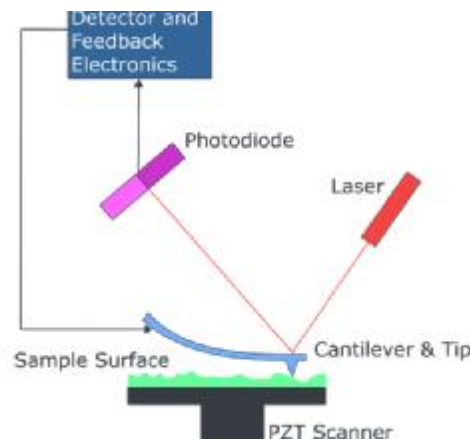


Figure 3.4 Block Diagram of Atomic Force Microscope

7. Transmission Electron Microscopy

In TEM, a focused electron beam is incident on a thin (less than 200 nm) sample. The signal in TEM is obtained from both undeflected and deflected electrons that penetrate the

sample thickness. A series of magnetic lenses at and below the sample position are responsible for delivering the signal to a detector, usually a fluorescent screen, a film plate, or a video camera. Accompanying this signal transmission is a magnification of the spatial information in the signal by as little as 50 times to as much as a factor of 106. This remarkable magnification range is facilitated by the small wavelength of the incident electrons, and is the key to the unique capabilities associated with TEM analysis.

TEM offers two methods of specimen observation, diffraction mode and image mode. In diffraction mode, an electron diffraction pattern is obtained on the fluorescent screen, originating from the sample area illuminated by the electron beam. The diffraction pattern is entirely equivalent to an X-ray diffraction pattern: a single crystal will produce a spot pattern on the screen, a poly-crystal will produce a powder or ring pattern (assuming the illuminated area includes a sufficient quantity of crystallites) and a glassy or amorphous material will produce a series of diffuse halos.

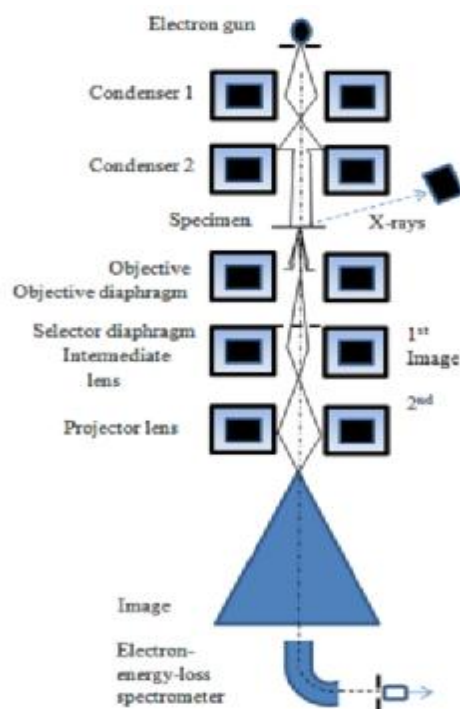


Figure 3.5 Schematic electron ray path for TEM equipped for additional x-ray and electron loss spectroscopy.

8. Raman Spectroscopy

Raman scattering is a powerful light scattering technique used to diagnose the internal structure of molecules and crystals. In a light scattering experiment, light of a known frequency

and polarization is scattered from a sample. The scattered light is then analyzed for frequency and polarization. Raman scattered light is frequency shifted with respect to the excitation frequency, but the magnitude of the shift is independent of the excitation frequency. This "Raman shift" is therefore an intrinsic property of the sample.

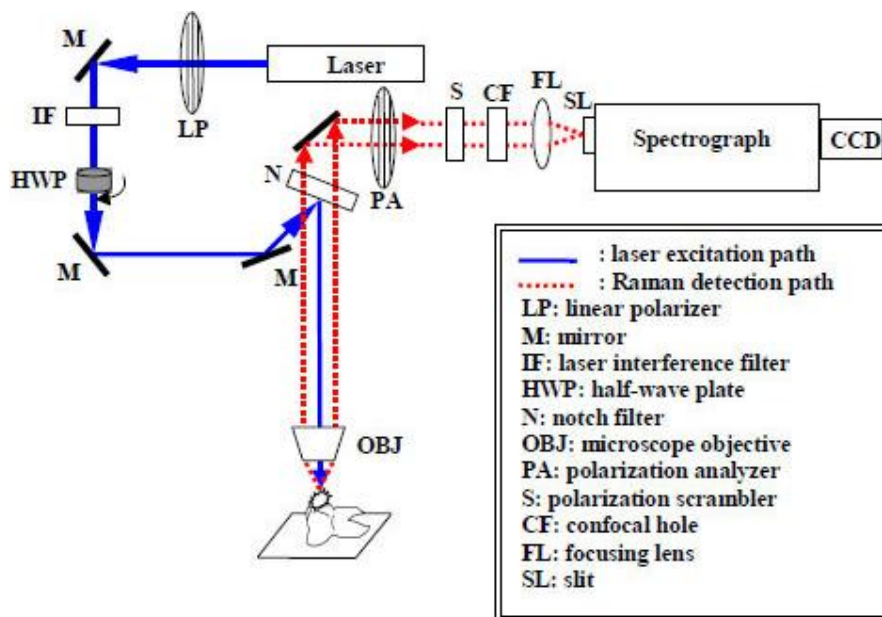


Figure 3.6 Schematic images of Raman spectroscopy

Raman spectroscopy usually consists of three parts: Laser, spectrometer and charge-coupled device array (CCD) detector. The spectrometer itself is a commercial "triple-grating" system. Physically, it is separated into two stages, i.e. monochromator and spectrograph, which are shown schematically in figure 3.6. The laser beam from the laser is filtered for monochromatic and directed by a system of mirrors to a focusing/collecting lens. The beam is focused onto the sample; the scattered light which passes back through the same lens is then passed through a second lens into the monochromator of the spectrometer. Finally the light is refocused and sent out to the spectrograph of the spectrometer to focus the filtered light on the final grating. The dispersed light is now analyzed as a function of position, which corresponds to wavelength. The signal as a function of position is read by the system detector. In the present case the detector is a multichannel charge-coupled device array (CCD) in which the different positions (wavelengths) are read simultaneously. The wavelength/intensity

information is then read to a computer and converted in software to frequency/intensity. This is the Raman spectrum which appears as the raw data.

9. UV/VIS Spectroscopy

UV/Vis spectroscopy is routinely used in the quantitative determination of solutions of transition metal ions and highly conjugated organic compounds.

The Beer-Lambert law states that the absorbance of a solution is directly proportional to the solution's concentration. Thus UV/VIS spectroscopy can be used to determine the concentration of a solution. It is necessary to know how quickly the absorbance changes with concentration. This can be taken from references (tables of molar extinction coefficients), or more accurately, determined from a calibration curve. A UV/Vis spectrophotometer may be used as a detector. The presence of an analyte gives a response which can be assumed to be proportional to the concentration. For accurate results, the instrument's response to the analyte in the unknown should be compared with the response to a standard; this is very similar to the use of calibration curves. The response (e.g., peak height) for a particular concentration is known as the response factor. The method is most often used in a quantitative way to determine concentrations of an absorbing species in solution, using the Beer-Lambert law:

$$A = -\log_{10}(I/I_0) = \epsilon \cdot c \cdot L$$

Where A is the measured absorbance, I_0 is the intensity of the incident light at a given wavelength, I is the transmitted intensity, L the path length through the sample, and c the concentration of the absorbing species. For each species and wavelength, ϵ is a constant known as the molar absorptivity or extinction coefficient. This constant is a fundamental molecular property in a given solvent, at a particular temperature and pressure, and has units of $1 / M \times \text{cm}$ or often AU / M x cm.

10. Cathodoluminescence Spectroscopy (CL)

Most natural materials give off colored light (emit photons) in the visible spectrum when they interact with an energetic electron beam. The process is known as "cathodoluminescence"

(CL). The fundamental emission process involves an electronic transition from an excited state (E_e) to a lower energy level or ground state (E_g). The causes of cathodoluminescence (CL) or the emission of photons by minerals are generally grouped into two types: intrinsic and extrinsic. The intrinsic CL center is native to host materials and involves band-to-band recombination of electron and hole pairs. Intrinsic CL emission may also associate with lattice defects (anion vacancies) within the minerals. This type of CL is also said to be a "defect" CL center. The most common CL center in the minerals is extrinsic, and it is attributed to the presence of trace amounts of impurities, transition metal and rare earth ions. This type of origin is referred to as an "impurity" CL center. Natural minerals and synthetic materials are not pure but always contain optically active dopant ions.

Chapter 4: Experimental

1. Introduction

As mentioned in previous section, there are many ways to synthesize 1D nanostructure. At the first section of this chapter, three main synthesis methods will be introduced, including sol-gel dip-coating, hydrothermal and polyol process' to prepare ZnO nanorods and colloidal solution of PbS, CdS, CuO and Ag nanoparticles. Second part is the formation of heterojunction of core-shell structure of ZnO/PbS and ZnO/CdS using ion exchange technic for photoelectrochimecal application.

2. Synthesis of ZnO nanorods

2.1 Substrate pre-treatment

The pre-treatment conditions of the substrate for the growth process, such as the pre-cleaning, concentration of the seed colloid, spin coating times, and annealing treatment of the substrate were the most important steps and have their respective influence on the morphology and quality of the ZnO nanostructures.

2.1.1 Substrate pre-cleaning

Prior to growth we immerse the substrate in ethanol and acetone in an ultrasonic bath each for 10 min and subsequently washing them with ultra pure water and then flushing them with air.

2.1.2 Seed layer for ZnO nanostructures

One of the advantages of the hydrothermal method is the use of a seed layer prior to the growth in the form of nanoparticles or thin films. This provides the nucleation sites for the growth of ZnO nanorods. Different solvents and precursors are being used for the preparation of the seed solution. We have chosen two different seed solutions in our work for making the seed layers. First, we prepared the seed solution by dissolving 5 mM of zinc acetate dihydrate ($\text{Zn}(\text{CH}_3\text{COO})_2 \cdot 2\text{H}_2\text{O}$) in pure ethanol solution. The use of this seed is preferred for hard substrate like ITO, FTO and glass because these substrates with spin coated seed layer need annealing at 340°C for 10 min to decompose $\text{Zn}(\text{CH}_3\text{COO})_2 \cdot 2\text{H}_2\text{O}$

into ZnO nanoparticles. Afterwards, we use sol-gel method, by dissolving 5 mM of $\text{Zn}(\text{CH}_3\text{COO})_2 \cdot 2\text{H}_2\text{O}$ together with diethanolamine (DEA) in pure isopropanol solution under temperature of 70 °C for 1h, and using dip-coating process to depose this film. In this case annealing at $T = 540$ °C for 1h is required for formation of ZnO nanoparticles. In order to achieve ZnO nanostructures growth, we first spun coat (four times) the ZnO nucleation layer, at a speed of 3000 rpm for 30 seconds. During the growth, the ZnO nanostructures preferentially nucleate from the top of the nanoparticles grains. Tuning the spin speed enables the control of the density of nanoparticles on the substrate. In simple words, controlling the seed layer thickness or surface coverage can provide a good control of the alignment for the growth and density of the nanostructures.

2.2 ZnO hydrothermal growth

There are several high and low temperatures ZnO nanostructures growth methods and both have some advantages and disadvantages. Comparatively hydrothermal methods are attractive, it attained much interest in the scientific community when Vayssieres et al [1]. successfully demonstrated the growth of ZnO microstructures on a glass substrate. It does not require sophisticated equipment; it is low cost, environment friendly, and thus suitable for scale-up. Different morphologies of the nanostructures can be readily obtained by tuning the hydrothermal conditions. In addition, the hydrothermal growth occurs at very low temperature and therefore holds great promise for nanostructures synthesis on a variety of substrates. The hydrothermal method has been demonstrated as a powerful and versatile method for synthesizing metal oxide nanostructures and so has been reported in the fabrication of electronic and sensing devices. The functioning of these devices is critically linked to the morphology of the nanostructures and hence requires tuning of the growth parameters for the optimal performance. In this work, we have synthesized ZnO nanorods, nanotubes, flower-like, and ZnO/CuO corals shape structures by this method. The schematic diagram of the hydrothermal growth procedure is shown in Figure 4.1.



Figure 4.1 Illustration of the hydrothermal growth method.

2.2.1 Synthesis of ZnO nanorods

As long as the ZnO nanorods are concerned, the fabrication was carried out on different substrate such as glass, ITO and FTO. Before finalizing the optimal conditions for ZnO nanorods growth on different substrates we have faced the problem of poor reproducibility, along with difficulty to control the size and the morphology. After systematic investigation, we used the following optimized conditions.

The growth solution used in this method contained 10 mM of zinc nitrate hexahydrate ($\text{Zn}(\text{NO}_3)_2 \cdot 6\text{H}_2\text{O}$) and 10 mM of Hexamethylenetetramine (HMT, $\text{C}_6\text{H}_{12}\text{N}_4$). While keeping their volume ratio at 1:1, We took the pre-seeded substrate and immersed it into an autoclave containing the nutrient solution. These were then kept for several hours in an ordinary laboratory oven at a temperature of 90 °C for 6 h. After the growth process, the samples were cleaned with ultra pure water several times, and dried in air.

2.2 Synthesis of ZnO core-shell and flowers-like

Dramatic change in the ZnO nanorods structure could occur by heating the obtained ZnO nanorods (with one step preparation) at 350 °C (10 min), adding seed NPs and subsequently applying hydrothermal growth with a diaminopropane (DAP) aqueous solution at low temperature of 90 °C during 6h.

3. Synthese of Lead Sulfide (PbS) and Cadmium Sulfide (CdS) nanoparticles

The aqueous PbS and CdS nanoparticles was prepared according to the two methods in PVA and PEG 200. For chemical synthesis of PbS or CdS quantum nanoparticules in polyvinyl alcohol (PVA), we followed the method published elsewhere [2-4].

Typically, a 5 wt% PVA solution was prepared in double distilled water, by stirring it in magnetic stirrer with the rate ~200 rpm at a constant temperature of 70°C until a transparent solution is formed. To this solution 0.01 M PbCl₂ or CdCl₂ solution was added in the volume ratio 2:1 followed by stirring at the same rate and the same temperature for three hours. To this solution, 0.01 M H₂S solution was added drop wise, until the whole solution turns dark brown for PbS nanoparticles and yellow color for CdS nanoparticles.

The second method: a sample of 0.1M of Lead acetate was dissolved in 60 ml of PEG 200 with 0.1M of sulfur powder. The final solution was irradiated with a microwave oven for several minutes. The color was dark brown.

4. Synthesis of silver (Ag) nanoparticles

Many chemical reduction methods have been used to synthesize silver nanoparticles from silver salts [5]. The reactions described here use silver nitrate as the starting material. Chemical reduction methods that have been used to synthesize silver nanoparticles from silver nitrate vary in the choice of reducing agent, the relative quantities and concentrations of reagents, temperature, mixing rate, and duration of reaction. The diameters of the resulting particles depend upon the conditions. An excess of reductor agent is needed both to reduce the ionic silver and to stabilize the silver nanoparticles that form.

In the present work, PVP (36,000 g/mole) (or glycose) and ethanol, DEG or PEG 600 is poured into a 100 mL pyrex flask. The solution is mixed by a magnetic stirrer until PVP (or glycose) is dissolved. Silver nitrate was added to the solution and stirring continues until the silver nitrate was dissolved. All solutions are made by dissolving 1.0 g of PVP (or glycose) and 0.1g of silver nitrate in 40 mL of EtOH, DEG or PEG 600. All this solution was irradiated by microwave oven untill the solution color change from transparant to brown if we used PVP and clear yellow when using glycose.

5. Synthesis of Cu₂O nanostructures

The protocol for Cu₂O nanoparticles preparation has been previously described in [6]. In a typical procedure, 0.03 g of Cu(OAc)₂·H₂O was added into an 80 mL round-bottomed flask, and then 36 mL of DEG and 4 mL of ultra pure water was added into the same flask. The reactants dissolved in the previous aqueous solution, after we irradiated in microwave oven for 3 min. The final product was yellow solution.

6. Synthesis of heterostructures

6.1. Synthesis of ZnO/CuO film

The ZnO NRs/CuO composite were fabricated by a simple hydrothermal method. The CuO nanoparticles were grown on the ZnO NR substrates by immersing them in a closed autoclave containing 0.05 mol/l ZnCl₂, 0.1 mM CuCl₂ and a proper quantity of ammonia (25 wt%). The pH value of the solution was adjusted by ammonia addition and kept at 10. The solution was slowly heated up to 95 °C, then the temperature was kept constant for 8 h. Subsequently, the as-prepared substrates were washed repeatedly with ultra pure water and dried at 100 °C for 1 h to remove any residual reactants. Finally, the substrates were annealed at 300 °C for 1 h to obtain a uniform dark-brown layer.

6.2. Synthesis of ZnO/Cu₂O film

Upon successfully fabricating homogeneous ZnO NRs and Cu&Cu₂O NPs colloidal, thin film of ITO/ZnO NRs/Cu₂O were fabricated in this study. Cu&Cu₂O NPs in DEG were spin-coated on as-prepared ZnO NRs and annealed at 200 °C for 30 minutes. This step was repeated to produce Cu₂O film with varied thicknesses.

6.3. Synthesis of ZnO/PbS core-shell nanorods

To prepare ZnO/PbS CS NRs, the ITO glass substrates with highly-ordered ZnO NRs arrays on them were transferred into a glass bottle containing 0.2 M of Na₂S·9H₂O to form in a first

step ZnS on ZnO. The bottle was heated at 50 °C for 3 h. The final products on the substrates were washed repeatedly and then dried at 60 °C before being used for the next step reaction. To complete the final preparation, the metal cation exchange process of ZnS to PbS was initiated by transferring the as-prepared highly-ordered ZnO/ZnS NRs arrays into a 50 mM aqueous lead acetate solution for several minutes. The color of the film changed from white to brown color for the ZnO/PbS CS NRs. A ZnO/PbS CS NRs heterostructure was synthesized using a two-step solution reaction.

6.4.Synthesis of ZnO/CdS nanorods core shell

To prepare ZnO/CdS CS NRs, the ITO glass substrates with ZnO NRs arrays on them were transferred into a glass bottle containing 0.2 M of Na₂S.9H₂O. The bottle was heated at 50 °C for 3 h. The final products on the substrates were washed repeatedly and then dried at 60 °C before being used for the next step reaction. To complete the final preparation, the metal cation exchange process of ZnS to CdS was initiated by transferring the as-prepared ZnO/ZnS NRs arrays into a 50 mM aqueous cadmium acetate solution for one hour. The color of the film changed from white for bare ZnO NRs to yellow color for the ZnO/CdS CS NRs.

Chapter 5: Results and Discussion

1. Introduction

This chapter describes the basic experimental setups and techniques used to study the systems under investigation in this thesis. The measurements were performed at IMEM Laboratory (Parma, Italy) and the University of Constantine 1.

2. Characterization of ZnO nanorods

The morphology and crystallographic structure of the as-grown ZnO seed layer nanograin was also analyzed by high resolution atomic force microscopy (AFM), as shown in figure (5.1).

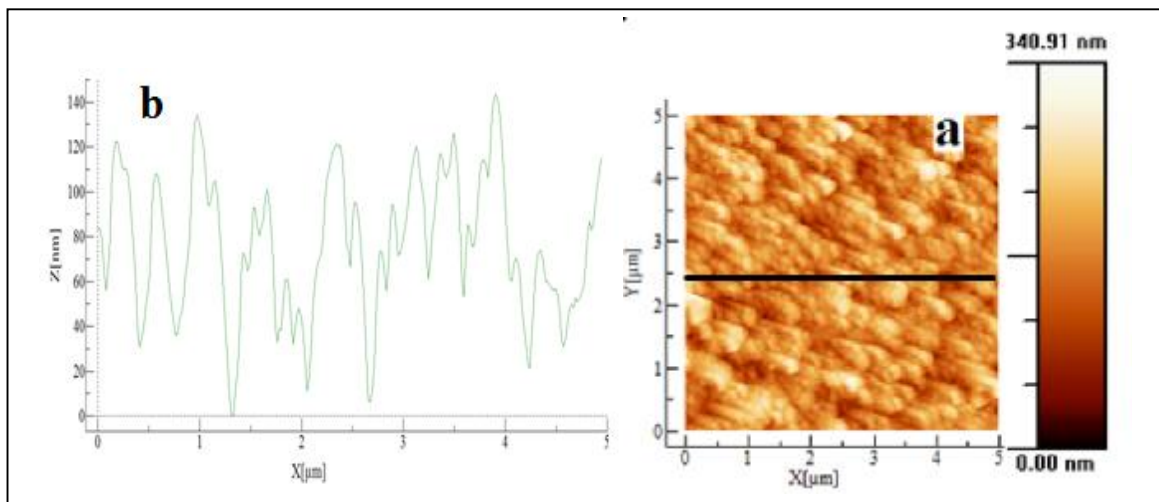


Figure 5.1 (a) AFM image of the ZnO seed layer and (b) the height profile (left) along the line.

By taking AFM image, the real structure of the ZnO surface can be probed as illustrated in Fig 5.1. It is obvious from Fig.5.1.(a) that the deposited seed layers are crystalline and consist of grains with an average size between 50 nm to 150 nm and the ultrathin nanorods were possibly grown by oriented coalescence of ZnO quantum dots.

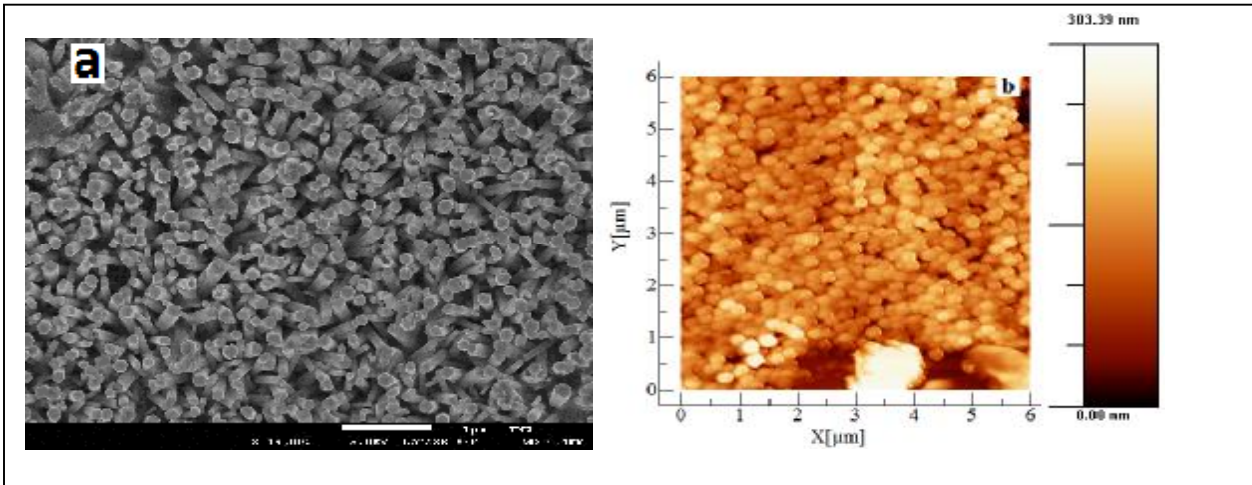


Figure 5.2. Top-view of (a) SEM and (b) AFM images of ZnO nanorods grown on ITO substrates with one step hydrothermal reaction

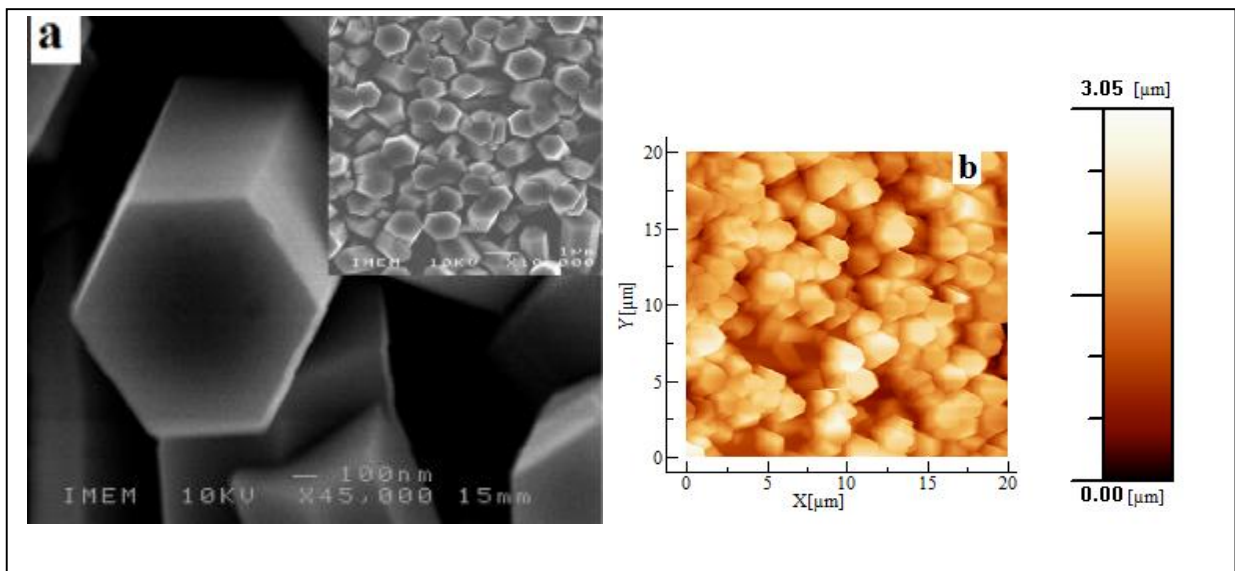


Figure 5.3 Top-view of (a)-SEM and (b)-AFM images of ZnO nanorods grown on ITO substrates with a second hydrothermal reaction.

The oriented attachment of preformed quasi-spherical ZnO nanoparticles should be a major reaction path during the formation of single crystalline ZnO NRs [1] as shown in Fig 5.1 (a). As can be seen from Fig 5.2, which shows the plane view of the ZnO NRs arrays grown on ZnO/ITO seeded substrates, when the reaction time was fixed at 6h, the ZnO NRs grew in a direction almost perpendicular to the surface of the substrate. Most of the nanorods exhibited hexagonal rod shape, implying good qualities of these ZnO crystals that grew along the [0002] direction. These nanorods also grew in a very high density with an average diameter of about 100 nm for one setup reaction and about 500 nm for a second hydrothermal reaction as shown

in Fig. 5.2(a). Apparently, prior seeding of the surface by ZnO layer leads to nucleation sites on which ZnO NRs arrays can grow in a highly aligned fashion and has significant influence on the morphology of ZnO NRs [2].

The possible mechanism of nanorods morphology elongated along one direction (c-axis) and shaped with a hexagonal cross-section can be explained from the wurtzite crystal structure of ZnO, which have a partial ionic nature. The (002) plane in ZnO is polar and hence have the highest surface energy among the low index planes. As a result, the highest growth rate is along the [0001] direction, and well oriented nanorods are easily formed in the c-axis orientation.

Fig. 5.4 presents the XRD pattern of ZnO nanorod. The peak at 34.42° indicates the (0 0 2) plane reflections from hexagonal ZnO. The single orientation and narrow full width at half maximum (FWHM) of (0 0 2) peak indicate an excellent crystalline structure of ZnO film, and that all nanorod arrays are preferentially grown along (0 0 2) orientation of ZnO film.

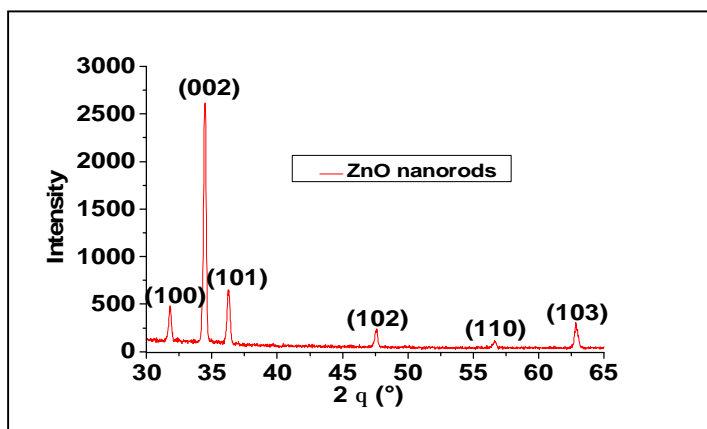


Figure 5.4 XRD pattern of ZnO nanorods.

Cathodoluminescence (CL) is a valuable technique for studying the optical emission properties of semiconductor and insulating materials at a very good spatial resolution. Change in CL spectra can lead to information about the formation of defect states or the change in defect populations. CL microscopy allows locations of defects or features to be mapped with resolution that can approach tens of nanometers, and is an indispensable tool for the study of light emission from materials and the factors that improve or degrade it in the semiconductor and optoelectronic industries



Figure 5.5 The room-temperature CL spectra of lateral surface and face of ZnO nanorods.

Fig 5.5 presents the room-temperature CL spectra of the lateral surface and face of ZnO nanorods. These spectra are consisted of an UV emission peak (3.2 eV) and a broad defect-related emission band in the visible light region ranging from green to red (and centered at 2.2 eV). The UV emission, also called as near band edge emission, is generated by the free-exciton recombination while the green emission, also known as deep level emission, appeared because of the impurities and structural defects in the deposited structures. The green emission is because of the recombination of electrons in single occupied oxygen vacancies in ZnO while the UV emission is because of the recombination of a photogenerated hole with an electron occupying the oxygen vacancies. It has been reported that the crystal quality of deposited ZnO is important factor for the high UV emission and hence betterment in the crystal quality (less structural defects and impurities such as oxygen vacancies and zinc interstitials) may enhance the intensity of UV emission [3]. Compared to the top surface, an intense defect emission from the lateral surface of ZnO nanorods is observed. This may be due to adsorption of hydroxyls to the polar lateral surface of the nanorods.

Therefore, heating followed by a second seed step and hydrothermal process can lead to more complex ZnO nanorods structuring as shown in Figure 5.6.

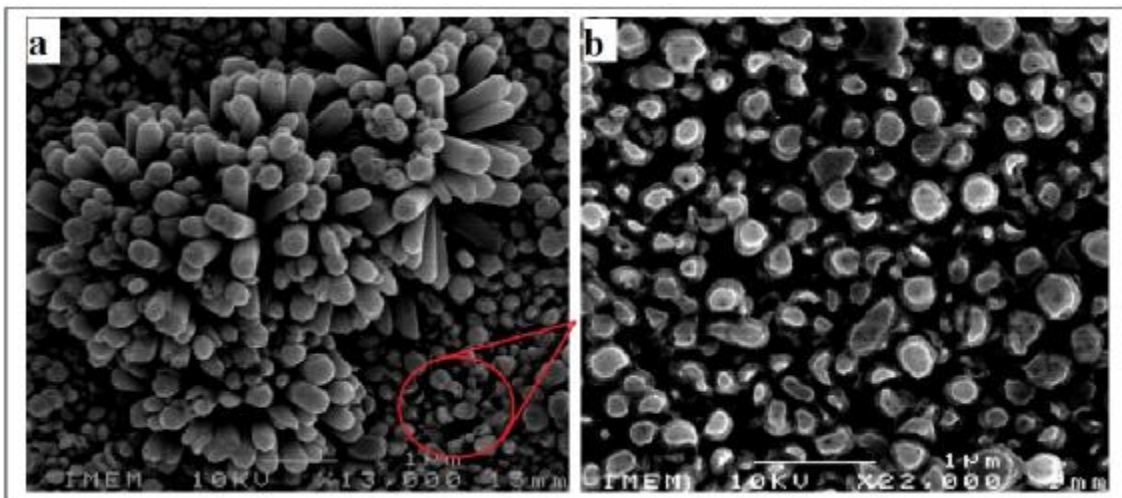


Figure 5.6 SEM images of ZnO (a) flower-like and (b) core-shell grown on ZnO seeded substrate, (b) is an enlarged local part of (a).

Zinc acetate was dissolved in ethanol and drop casted on a pre-prepared ZnO nanorod substrate to form uniform seeds. After each coating, the samples were annealed at 340 °C for 5 min. Through the seed pre-coating process on the ZnO nanorods, crystalline nanoparticles with a diameter of 10-20 nm were formed on the backbone nanorods. After the second growth step, shells of secondary ZnO emanated from the seeds, as shown in Fig. 5.7 (a-b), were formed. As can be seen, the nanorods shown in Fig. 5.7 (a) reveals a nanorod core surrounded by a shell. Thus the nanorods have a core-shell structure. The backbone of nanorods have diameter in the range of 150-200 nm, whereas the shell has diameter ranging from 10 to 20 nm. According to the present results, the core shell ZnO nanorods can be fabricated by the infiltration of moderate concentrated $Zn(OAc)_2$ solution into interstitial voids between backbone ZnO nanorods in a second step of growth. However, the shells were not produced on the surface of each ZnO backbone. The lack of uniformity of shells can be interpreted as the results of rough dip-coating processes that cause non-uniform infiltration and finally lead to randomly disturbed seed layers upon the backbone ZnO nanorods. These conditions would mostly occur when using more concentrated $Zn(OAc)_2$ solution and also when the substrates were heated during dip-coating. The fast crystallization would lead the aggregation of ZnO seed layers and consequently blocked the infiltration of subsequent aqueous solutions [4].

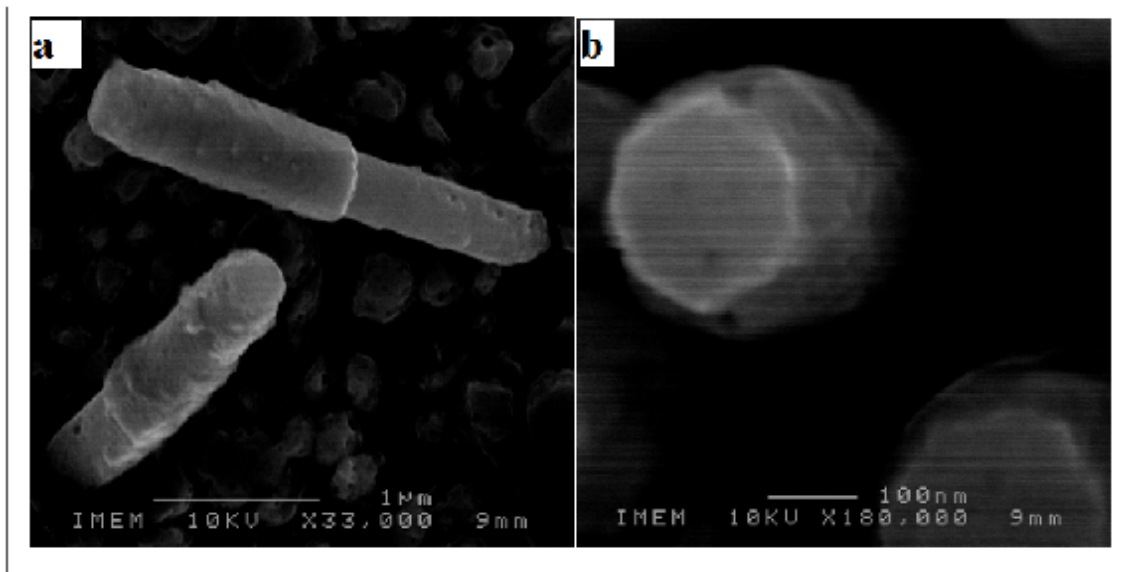


Figure 5.7 SEM images of ZnO core-shell (a) and (b).

Cathodoluminescence (CL) spectra of the ZnO nanorods, after hydrothermal second step growth, were recorded as shown in Fig. 5.8. The excitonic CL band of ZnO nanorods grown in the second step becomes more intense compared to the defect related emission. In addition the defect related band is red-shifted, demonstrating the presence of an additional intra-gap state, not found in the pure rod spectrum.

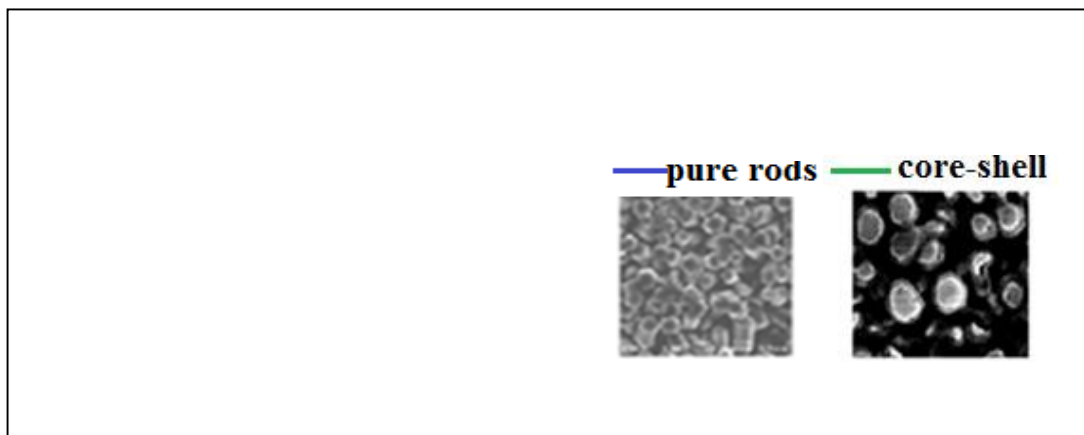


Figure 5.8 The room-temperature CL spectra of pure and core-shell ZnO NRs.

Wurtzite ZnO belongs to $C6v4$ ($P63mc$) space group, with two formula units per primitive cell. At the point of the Brillouin zone, group theory predicts the existence of the following phonon modes: $\Gamma = 2A_1 + 2B_1 + 2E_1 + 2E_2$. Among these modes, there are acoustic modes with $\Gamma_{aco} = A_1 + E_1$ and optical modes with $\Gamma_{opt} = A_1 + 2B_1 + E_1 + 2E_2$. The B_1 modes are silent modes. For the

long-range electrostatic forces, both A1 and E1 modes are polar and are split into transverse (TO) and longitudinal optical (LO) phonons, all being Raman and infrared active. The A1 phonon vibration is polarized parallel to the C-axis; the E1 phonon is polarized perpendicular to the C-axis. The two E2 modes (E2(high), E2(low)) are nonpolar modes and are Raman active only. Every mode corresponds to a band in the Raman spectrum. Figure 5.9. illustrates the room temperature Raman spectrum of ZnO nanorods. All the modes of ZnO can be seen from this figure. The intensity of these bands depends on the scattering cross section of these modes. For the polar modes, the scattering cross section of TO modes only depends on the deformation potential, but that of the LO modes depends, in addition, on the linear optoelectric effect. The linear optoelectric effect is attributed to polar phonon-induced macroscopic electric field coupled with excited electrons [7].

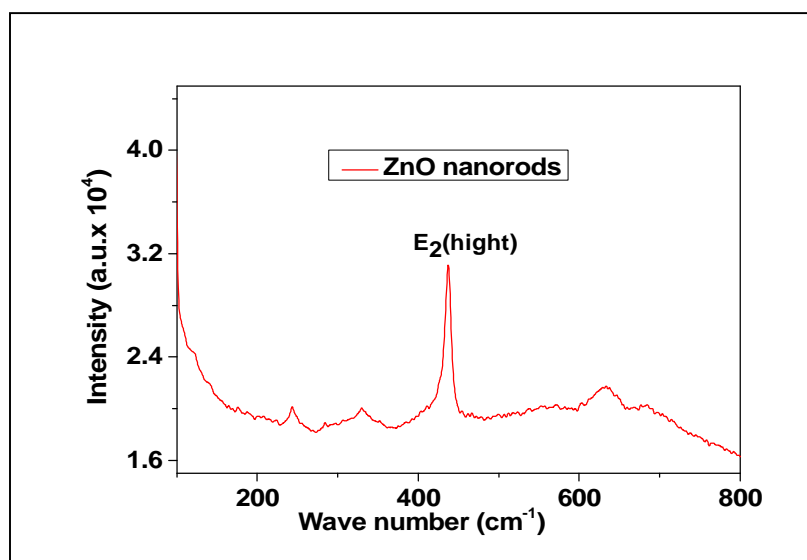


Figure 5.9 Raman spectra of ZnO nanorods.

In the ZnO NRs spectrum, the peak at 436 cm^{-1} corresponds to E2(high), which is shifted by 3 cm^{-1} compared to bulk. The peak at 582 cm^{-1} is positioned between A1(LO) and E1(LO), which is in a good agreement with the theoretical calculations of Fonoberov and Balandin [8, 9, 10]. The broad peak at about 330 cm^{-1} is attributed to the second-order Raman processes.

3. Characterization of Lead Sulfide (PbS) and Cadmium Sulfide (CdS) nanoparticles

Structural identification of PbS and CdS films was carried out with X-ray diffraction in the range of angle 2θ between 10 to 100 . The XRD patterns in Fig.5.10 show that the products obtained are the cubic phase for PbS nanoparticles and hexagonal symmetry for CdS nanoparticles. The observed broad hump in XRD pattern is due to amorphous glass substrate. The peaks are corresponding to hkl values of (111), (200), (220), (311) and (222), which match well with literature patterns (JCPDF card No. 6-0261 and 5-0592) as shown in Fig 5.10 (a) and most typical diffraction peaks of hexagonal CdS, such as the (1 0 0), (0 0 2), (1 1 0), (1 0 3), and (1 1 2) peaks can be found in this pattern, which indicates there is no preferred grainorientation in the thin film as demonstrated in Fig 5.10 (b).

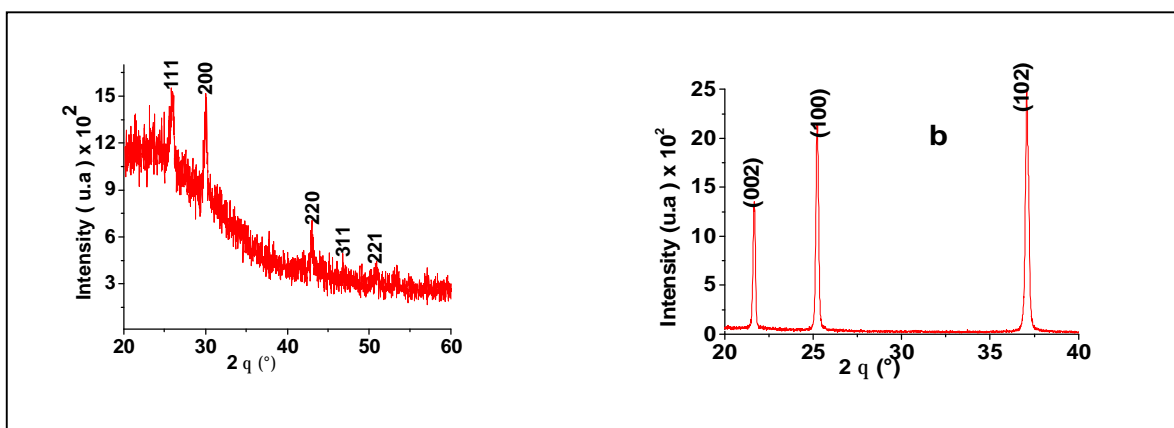


Figure 5.10 XRD pattern of (a) PbS and (b) CdS nanoparticles

The Raman measurement was employed to investigate the composition and purity of the prepared PbS and CdS nanoparticles as shown in Fig. 5.11.

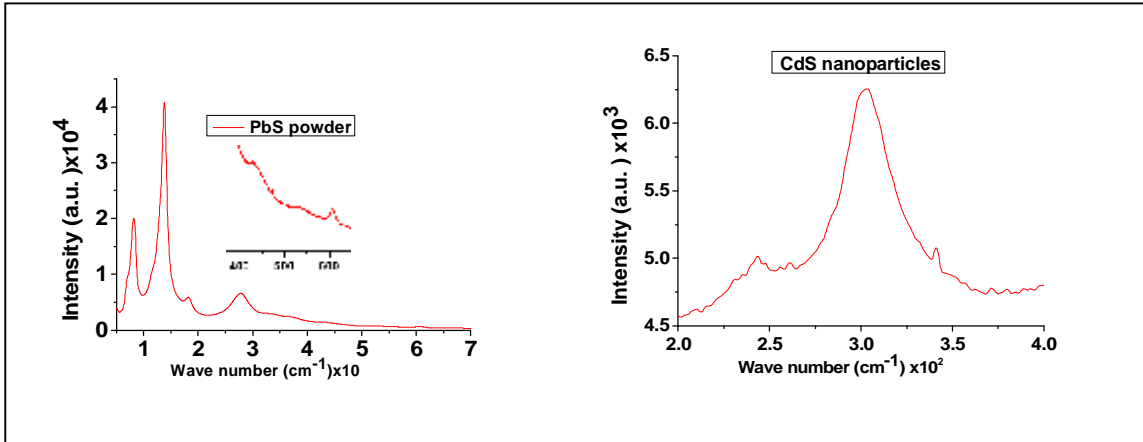


Figure 5.11 Raman spectra of CdS and PbS nanoparticles

The Raman spectrum of PbS nanoparticles is shown in Fig. 5.11 (PbS). The sharp strong peak located at 140 cm^{-1} originates from the combination of longitudinal and transverse acoustic [LA(L)+TA(L)] modes of PbS [10]. And the other two peaks at 190 cm^{-1} and 270 cm^{-1} due to Longitudinal Optical (LO) phonon of PbS layers [11].

From figure 5.11 (CdS) it is seen that the first order Longitudinal Optical (LO) Raman line is not only broadened, but also it shows an asymmetric broadening towards the low frequency side. The 1 LO phonon frequency for a single crystal of CdS was reported as 300 cm^{-1} [12], while the value obtained in the present study is around 300 cm^{-1} . This frequency shift of the 1 LO Raman peak in CdS nanoparticles has been studied before and is mainly ascribed to the grain size effect [13].

The TEM observation for PEG 200 capped PbS nanoparticles is shown in Fig.5.12 (a). The resolution of this image was taken at the scale of 10 nm. From the micrograph, it is seen that the size distribution of the nanoparticles are quite uniform. It clearly shows that these particles are unaggregated in the solution. The average size of the PbS nanoparticles, observed from TEM are in the range of 5-10 nm respectively.

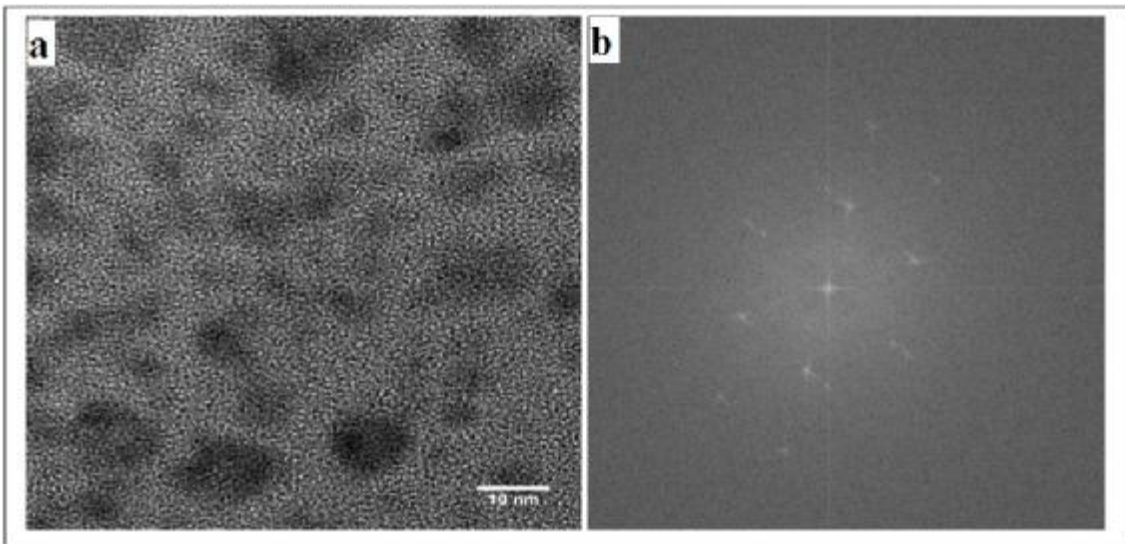


Figure 5.12 (a) TEM image and (b) electron diffraction pattern of the PbS nanoparticles in PEG 200

The electron diffraction pattern as shown in figure 5.12 (b) was used for the determination of the crystalline structure of the nanoparticles and therefore for their classification. In this pattern, the bright spots are due to the electron diffraction from the PbS crystalline planes. It can be concluded that the nanoparticles embedded in PEG 200 observed in the TEM image are PbS crystalline nanoparticles with a cubic structure.

UV visible spectrum has been widely used to characterize the semiconductor nanoparticles. As the particle size decrease, absorption wavelength (λ_{max}) will be shifted to shorter wavelength, since the band gap increases for the nano sized particles [14]. This is the quantum confinement effect of the semiconductor nanoparticles. The absorption coefficient of the bulk PbS is 3020 nm and for the CdS is 540 nm. UV-vis pectrum of both PVA capped PbS and CdS nanoparticles is shown in Fig. 5.13. In this spectrum, λ is observed at 550 nm for PbS and 450 nm for CdS nanoparticles. This indicates that the absorption shift towards the shorter wavelength (significant blue shift), because of the particle size reduction and the result of the quantum dimensional effect (strong quantum confinement) [15]. This result is in agreement with previously reported data for colloidal PbS prepared in the presence of PVA where position of absorption bands were found to be 2.08, 3.22 and 4.26 eV [16]. It shows that the optical band gap of these materials was highly enhanced. This reveals that, when the size of the particles is reduced to very low size, the energy states separation is too high (i.e, energy gap).

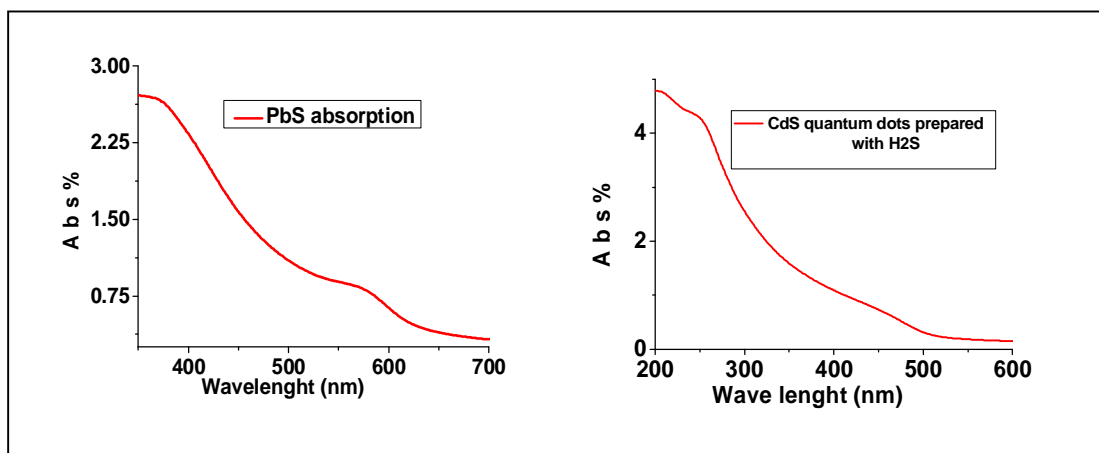
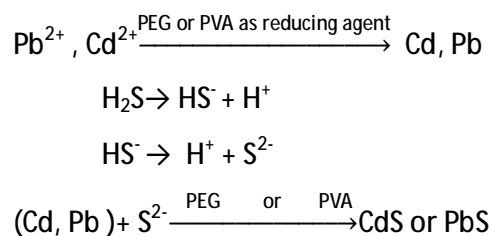


Figure 5.13 Absorption spectrum of PbS and CdS prepared with H₂S.

It was found in the preparation of CdS and PbS using PEG 200 or PVA, that the conditions would influence the formation of this nanoparticles. The reaction was carried out in different precuseur and time. On one hand, the reaction could not fully proceed with low power and short reaction time. On the other hand, due to the insolubility of reactants in PEG 200, excessive high power could lead to the agglomeration of the reactants, therefore, pure final products could hardly be obtained. Change the precursors lead to change the morphology and size of the final products. The probable reaction mechanism could be described as follows:



In the first step, CdCl₂ and PbCl₂ were reduced to metal Cd and Pb as the intermediate of the whole reaction. The process is known as the preparation process and temperature is a dominant factor in affecting the reactivity. In the second step, metal particles were directly combined with S from H₂S, leading to the formation of the final product. Then, uniform CdS and PbS nanosized particles could be formed.

4. Characterization of silver (Ag) nanoparticles

Many chemical reduction methods have been used to synthesize silver nanoparticles from silver salts [17]. The reactions described here use silver nitrate as the starting material. Chemical reduction methods that have been used to synthesize silver nanoparticles from silver nitrate vary in the choice of reducing agent, the relative quantities and concentrations of reagents, temperature, mixing rate, and duration of reaction. The diameters of the resulting particles depend upon the conditions. An excess of reductor agent is needed both to reduce the ionic silver and to stabilize the silver nanoparticles that form.

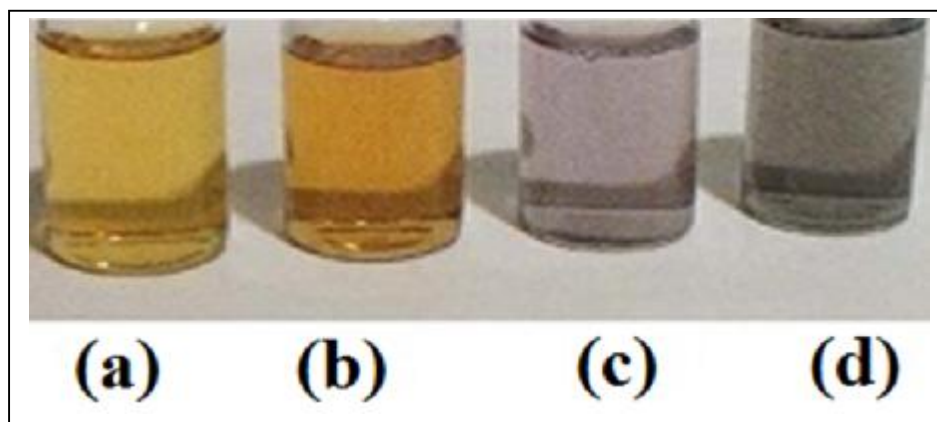


Figure 5.14 Colloidal silver in various stages of aggregation, (a) clear yellow sol, (b) dark yellow, (c) violet, and (d) Grayish, as aggregation proceeds

Reaction conditions, including stirring time and relative quantities of reagents, must be carefully controlled to obtain stable yellow and brownish colloidal silver. If stirring is continued once all of the silver nitrate has been added, aggregation begins as the yellow sol first turns darker yellow, then violet and eventually grayish, after which the colloid breaks down and particles settle out. Similar aggregation may also occur if the reaction is interrupted before all of the silver salt has been added.

Silver nanoparticles were examined using UV-vis, Raman spectroscopy and TEM microscopy. The distinctive colors of colloidal silver are due to a phenomenon known as plasmon absorbance. Incident light creates oscillations in conduction electrons on the surface of the nanoparticles and electromagnetic radiation is absorbed. The spectrum of the colloidal silver from the synthesis above is shown in Figure 5.15. The plasmon resonance produces a peak near 400 nm for PVP, DEG and PEG 600, with PWHM of 50 to 70 nm and about 280 nm

for the Glycose. The wavelength of the plasmon absorption maximum in a given solvent can be used to indicate particle size.

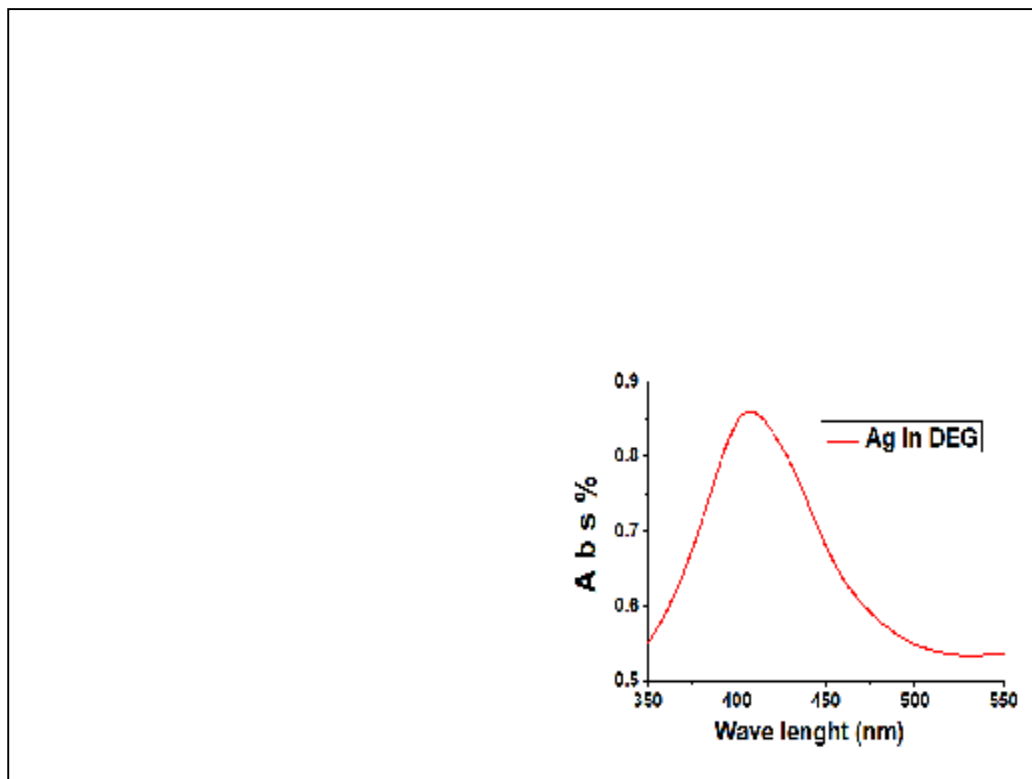


Figure 5.15 UV-VIS absorption spectrum of colloidal Ag, using different precursor.

The produced silver nanoparticles were examined using transmission electron microscopy (TEM). A sample of silver nanoparticles from a freshly synthesized sol was prepared by drying a small drop on a carbon-coated 200-mesh copper grid.

Table 4.1 Particle size and spectral features of silver nanoparticles

	Particle size (nm)	λ_{\max} (nm)	PWHM
DEG	5-12	408	68
PEG(600)	8-12	405.5	47.5
Glucose	5	278	13
PVP	5-10	432	43

The TEM images of one region of the samples is shown in Figure 5.16. These images show that the silver nanoparticles are spherical with sizes of 5 to 12 nm. In general, as the particles become larger the absorption maximum shifts to longer wavelengths and the peaks broaden. The peak width at half the absorption maximum (PWHM), silver nanoparticle size, and plasmon maxima, are listed in table 4.1

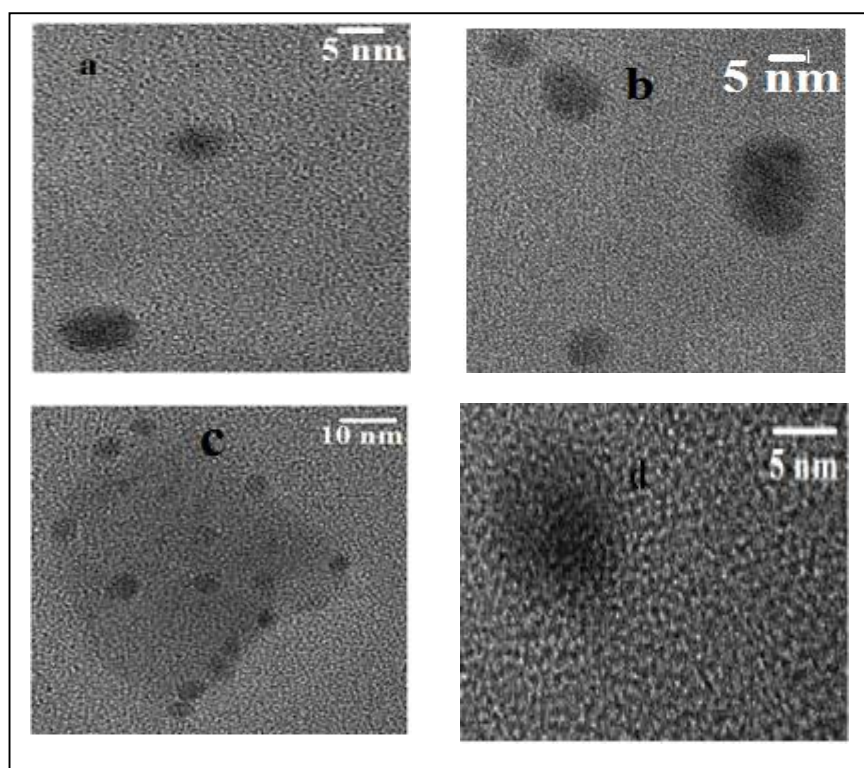


Figure 5.16 TEM images of Ag nanoparticles synthesized by polyol method using silver nitrate with: (a) Di-ethylene glycol, (b) Ethanol + PVP, (c) Glucose, (d) poly-ethylene glycol (600)

5. Characterization of Cu₂O nanostructures

The transmission electron micrographs (TEM) display the pictorial view of size, shape and the surface morphology of the nanoparticles.

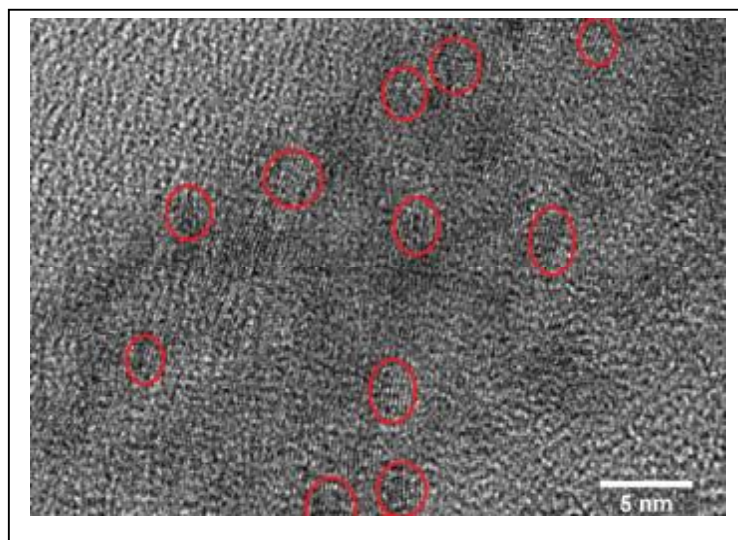


Figure 5.17 TEM image of Cu₂O nanoparticles, synthesized by polyol method

The TEM image of the obtained Cu₂O shows well dispersed roughly spherical particles, the mean sizes of this particles are about 5 to 10 nm for the surfactants of DEG as shows in Fig. 5.17. The X - ray Diffraction (XRD) patterns of the samples are shown in Fig. 5.18.



Figure 5.18 XRD pattern of: (a)- ZnO NRs thin film, (b)- Cu&Cu₂O nanoparticles deposited on glass substrate after precipitation.

The diffraction peaks correspond to the reflection of both cubic phase of Cu_2O and Cu metal. The positions of the peaks are in good agreement with literature values. Moreover, The peaks at 2θ values of 29.5° , 36.4° , 42.3° , 61.6° , 73.8° and 77.6° , within experimental error, correspond to (110), (111), (200), (220), (311), (222) lattice planes of standard crystalline Cu_2O and Cu, respectively. In order to investigate the optical properties of Cu & Cu_2O NPs in comparison with bulk crystalline films, the absorbance was measured as a function of wavelength in the range of 200-600 nm as shown in Fig. 5.19.

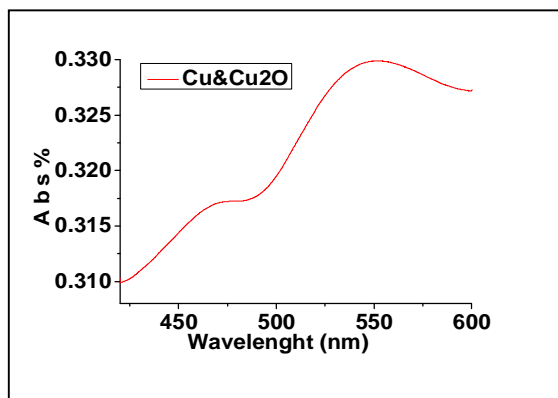


Figure 5.19 Absorption spectra of Cu_2O & Cu dispersed in DEG.

It can be seen from this figure that intensive absorptions are present in the visible range of about 400 to 550 nm. The UV-Vis absorption spectra showed that the absorption peaks of analysed Cu_2O particles are at 470 nm relative blue-shift to the band gap of bulk Cu_2O (~ 2 eV). The peaks positions can be related with the mean diameter of particles, smaller diameter meaning lower wavelength. The results showed the effect of quantum confinement (quantum size effect, QSE). The QSE in direct-gap semiconductors nanocrystals is well understood; such a shift of the optical absorption edge to higher energies with decreasing size, can explain the UV-Vis blue-shift effect. At first, the precursor solution was green in color, a typical feature of copper acetate, afterwards, two peaks appeared at 470 nm, corresponding to the formation of the yellow Cu_2O and at 570 nm belong to some intermediate states corresponding to a mixture of Cu metal and Cu_2O .

6. Characterization of heterostructures

ZnO photoactive requires ultraviolet radiation (UV light source energy exceeding the band gap of ZnO which is 3.2 eV). Therefore, only 3-4% of the solar spectrum that reaches

Earth can be utilized. Effective utilization of visible light for Photoelectrochemical operations would suggest that a larger fraction of energy from the sun could be used. Hence, much research attention has been toward the development of renewable energy that are activated by the absorption of visible light. Sensitizer like PbS, CdS, CuO-Cu₂O and noble metal such as silver with certain modifications of the reaction medium shows a significant photoactivity under the visible spectrum of light [18]. Hence further researches were carried out to modify the ZnO photosensitivity by extending their photoactive response under the visible spectrum of light. Recently several methods used by researchers to improve the charge separation for extending the photoactive response to the visible light is by coupling a narrow band gap semiconductor with a higher bandgap material [19]. By this approach, charge injection from the narrowband gap semiconductor to the conduction band of higher bandgap material occurs. This can lead to efficient and longer charge separation by minimizing the electron-hole recombination. The noble metal functions as a sink for photo generated electrons and maximises the efficiency of photoelectrochemical reactions.

6.1. Characterization of ZnO/CuO film

The ZnO NRs/CuO composite were fabricated by a simple hydrothermal method. The CuO nanoparticles were grown on the ZnO NR substrates by immersing them in a closed autoclave containing 0.05 mol/l ZnCl₂, 0.1 mM CuCl₂ and a proper quantity of ammonia (25 wt%). The pH value of the solution was adjusted by ammonia addition and kept at 10. The solution was slowly heated up to 95 °C, then the temperature was kept constant for 8 h. Subsequently, the as-prepared substrates were washed repeatedly with ultra pure water and dried at 100 °C for 1 h to remove any residual reactants. Finally, the substrates were annealed at 300 °C for 1 h to obtain a uniform dark-brown layer (Fig. 5.20) [20].

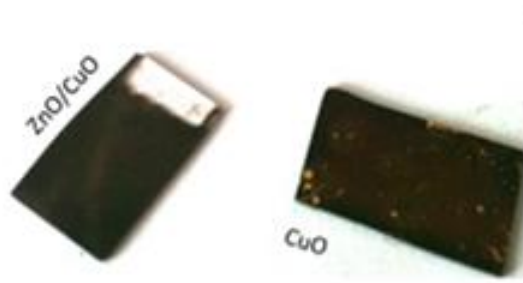


Figure 5.20 Optical photograph images showing CuO, and nanohybrid ZnO/CuO structures grown by the hydrothermal method.

The ZnO NRs and ZnO/CuO bilayer films before and after annealing at $T = 300\text{ }^{\circ}\text{C}$ were characterized by XRD analysis to assess the crystallinity of the films. In general, the XRD analysis reveals information about the crystallographic structure of the thin films. Figure 5.20 shows the XRD pattern of the ZnO NRs film which is in good agreement with the diffraction pattern of the standard wurtzite structured ZnO (zincite syn, JCPDS file no. 36-1451). This shows that the ZnO NRs film has wurtzite structure and the sharp diffraction peaks suggests that the ZnO NRs film has good crystallinity.

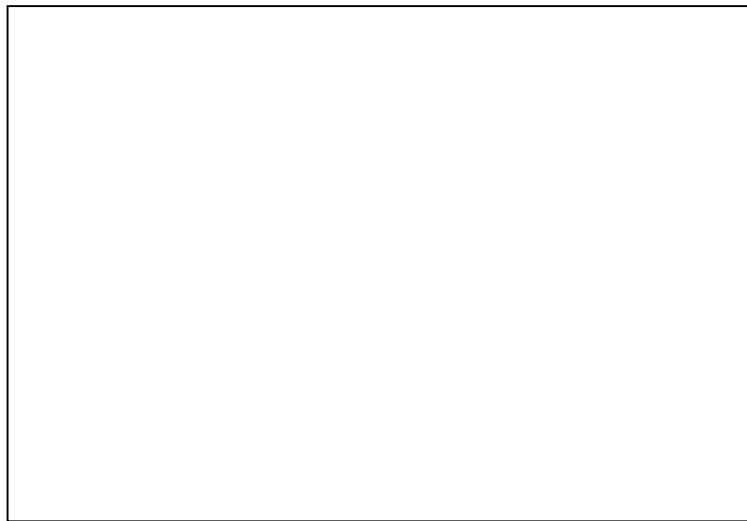


Figure 5.21 XRD spectra of pure ZnONRs and CuO/ ZnONRs heterostructure before and after annealing at $300\text{ }^{\circ}\text{C}$

In the case of ZnO NRs/CuO film, XRD studies showed that before and after the CuO capping, the wurtzite structure of ZnO did not change. No other composite phase was found, probably, because of very low amount of CuCl_2 precursor.

The addition of CuO to the pure ZnO nanorods film changes its region of absorbance from the UV to the visible (at about 530 nm) for the ZnO NRs/CuO film. Figure 5.22 shows that the ZnO film has an absorption edge at 370 nm, this absorbance corresponds to a bandgap of 3.3 eV. This value is in good agreement with which was formerly reported for wurtzite structured transparent ZnO film. Absorption spectra of the CuO/ZnO NRs films shows UV absorption of ZnO NRs and absorption edge at 530 nm it corresponds to a bandgap of 2.2 eV, which is in good accordance with literature that reports 2.2 eV as the band gap of CuO films.

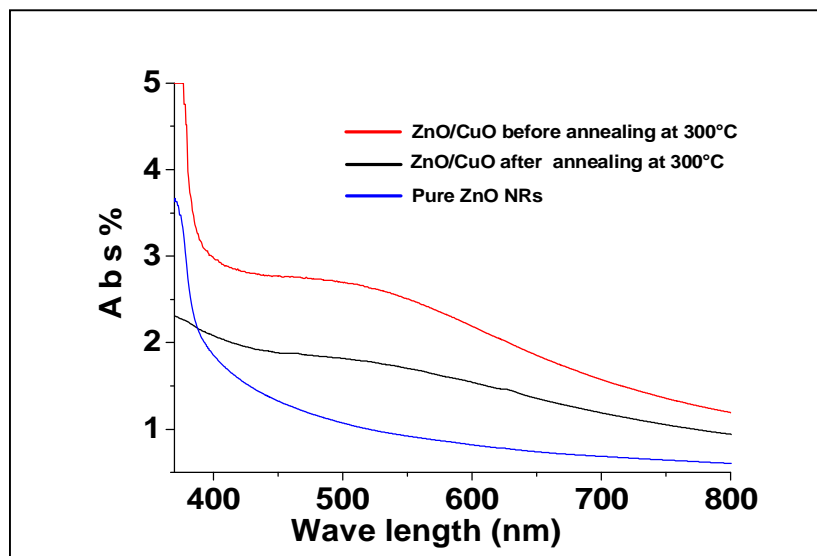


Figure 5.22 Absorption spectrum of pure ZnO NRs and CuO/ZnONRs before and after annealing at 300 °C

The annealing process at 300 °C for 1 h reduces this absorbance (Fig. 4.24). At this temperature we observe considerable degradation of the absorbance in the UV region which may be explained by a possible inter-diffusion between ZnO and CuO. The decoration of ZNRs with CuO nanoparticles is observed clearly in Fig. 5.23.

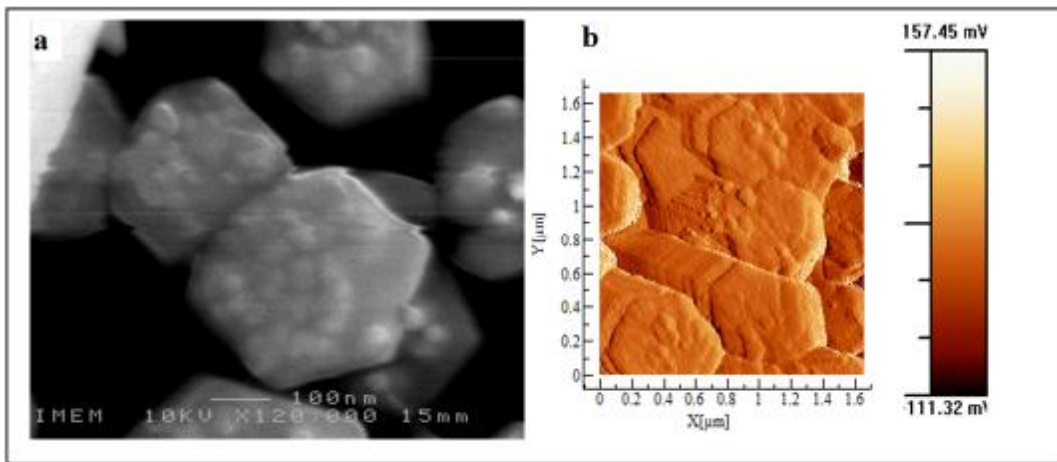


Figure 5.23 Top-view of (a) SEM image of ZnO-CuO film grown on ITO substrate. (b) AFM images of composite ZnO-CuO film grown on ITO substrates, affected by tip astigmatism due to the columnar shape of the rods.

The SEM columnar image indicates that the composite film is assembled by many grain-like structures made on nanorods. The size of the grains can reach 20 nm.

The CuO coated ZnO nanorods present interesting and different optical properties before and after annealing at 300 °C as shown in Fig. 5.24 and Fig. 5.25.

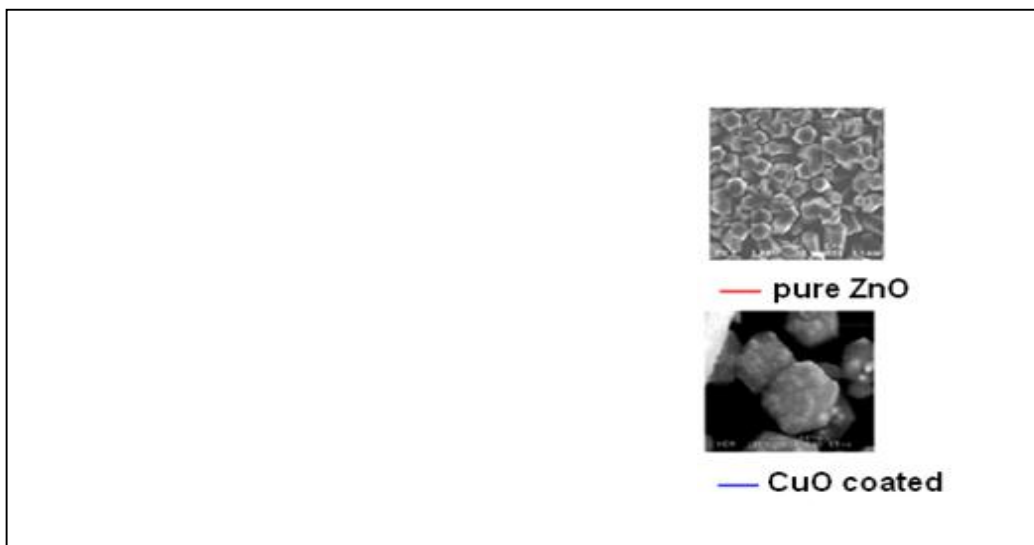


Figure 5.24 The room-temperature CL spectra of the pure ZnO NRs (red) and after CuO coating (blue)

When excited with electron beam, both of the near-band-edge emission and the defect emission are quenched after CuO capping of the pristine ZnO nanorods, as shown in the Fig.

5.23. The band-edge emission of CuO coated ZnO centered around 3.2 eV disappears completely indicating either a strong interaction between CuO precursor by-products and ZnO or a high coverage of ZnO surface with these by-products.

After annealing at 300 °C for 1h, the composite CuO-ZnO presents a different CL behavior, where the defect related emission completely disappears, while the excitonic emission reappears, as shown in Fig. 5.25.

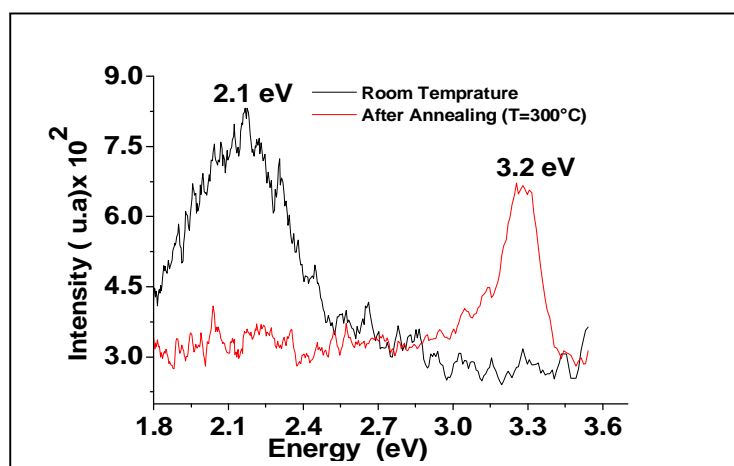


Figure 5.25 The room-temperature CL spectra of the composite CuO-ZnO NRs at room temperature and after annealing

Figure 5.25 shows the room temperature Raman spectra of the CuO/ZnO NRs heterostructures. As we know, the Raman spectra of the pure ZnO nanorods arrays exhibited four peaks at 202, 330, 436 and 574 cm^{-1} . Among these peaks, the three peaks at 436 and 576 cm^{-1} are assigned to E_2 High and A_1 Low modes, respectively, while the peaks at 202, 330 and 574 cm^{-1} emerged due to the multiphonon processes. The three peaks were assigned to $2E_2L$, $[E_2L - E_2H]$ and $[E_2L + B_1H]$ modes, respectively. Compared to pure ZnO nanorods, the Raman spectrum of the CuO/ZnONRs heterostructure shows two additional peaks at 286 and 627 cm^{-1} . These two peaks correspond to the A_{1g} and B_{2g} modes of crystalline CuO due to the vibrations of the oxygen atoms. However, compared to the literature [21], a red shift of the Raman peaks is observed. This may be due to the introduction of the stress during the growth process of the composite nanostructures. The coexistence of the CuO and ZnO Raman modes in the Raman spectra further confirms that the structure is a composite nanostructure, consistent with the XRD and TEM results.

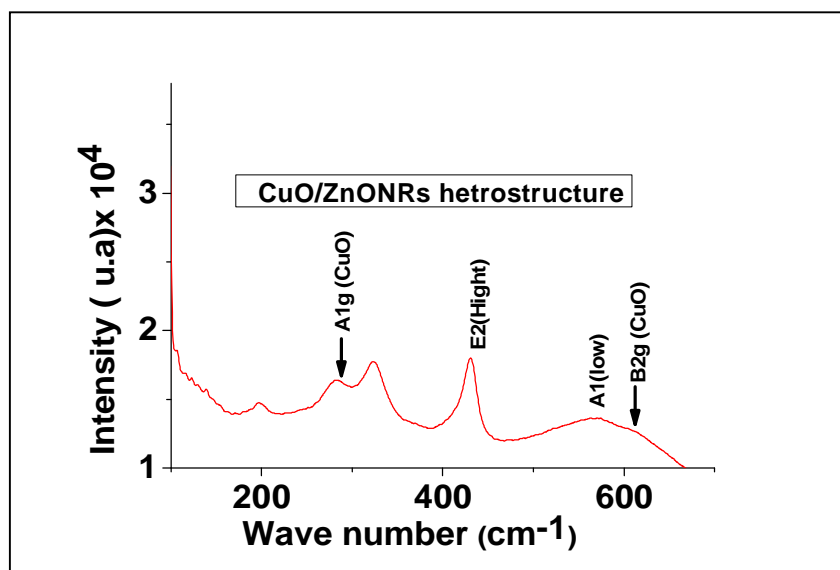


Figure 5.26 Raman spectra of ZnO nanorods coated CuO

The ZnO/CuO/Ag film were obtained by adding a simple Ag film using spin-coating of Ag colloidal solution prepared with ethanol and PVP precursors on as-prepared CuO/ZnO film.

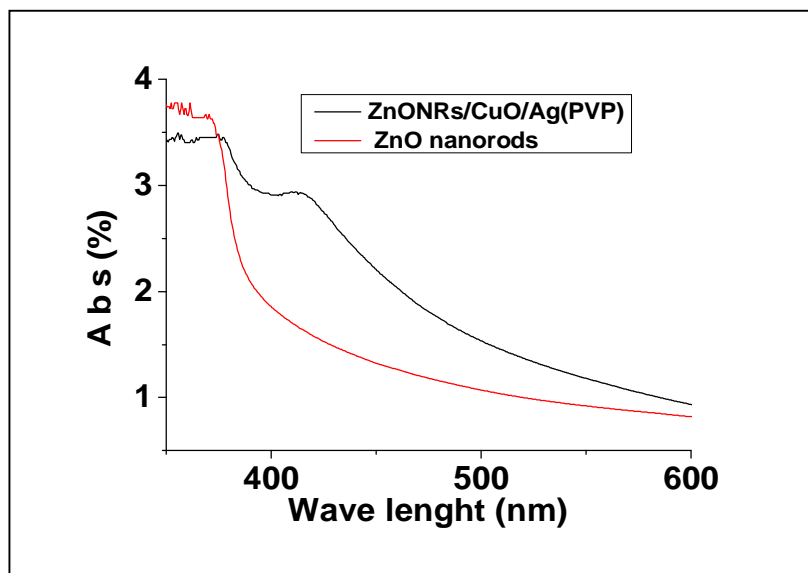


Figure 5.27 Absorption spectra of ZnO nanorods and ZnONRs/CuO/Ag film.

This film is highly absorbing in visible region between 400 to 500 nm as shown in Figure 5.27, due to the surface plasmon resonance of the Ag nanoparticles. The band at about 370 nm has been associated with the absorption of ZnO NRs.

6.2. Characterization of ZnO/Cu₂O film

The surface morphology of this film was determined by scanning electron microscopy (SEM). Fig 5.28 shows the SEM image of the ZnO NRs/Cu₂O composite. The growth of the film of Cu₂O was observed to be a globe-like structure overgrown on the nanorods of ZnO.

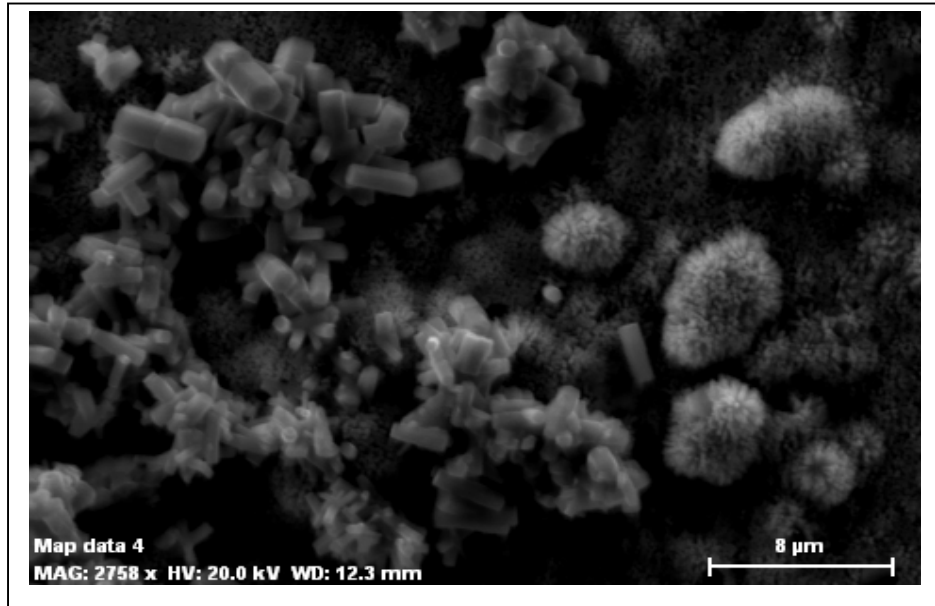


Figure 5.28 SEM image of ZnO NRs/Cu₂O composite film.

To check the chemical composition of the as-grown ZnO NRs/Cu₂O composite film, an energy dispersive X-ray (EDX) microanalysis was performed on the film. Fig. 5.29 shows a typical EDX spectrum of ZnO NRs/Cu₂O grown on seeded-ITO substrate. Three main peaks have been clearly observed from the spectrum, which are related to zinc, oxygen and Cu. The analysis confirms the presence of Zn, O and Cu in the composite film with Zn ≈ 60%, O ≈ 11.5% and Cu ≈ 1.24% as investigated above.

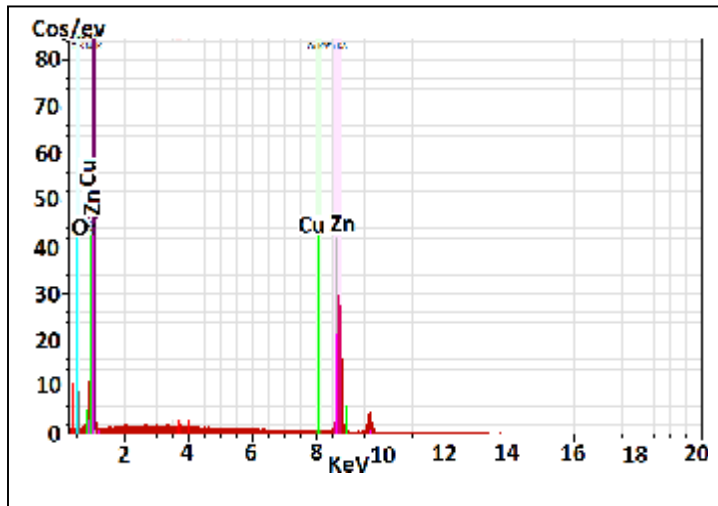


Figure 5.29 EDX spectrum of ZnO NRs/Cu₂O composite, indicating the presence of Zn, O and Cu.

The oxidation of Cu NPs [22] is interesting to study because Cu possesses multiple oxidation states and usually forms the stable oxides for example Cu₂O. Solid NPs were obtained after altering the oxidation process. To induce further oxidation, Cu&Cu₂O NPs were deposited on a ZnO NRs and annealed at 200 °C.

The lattice dynamics of a crystal are reflected in its phonon dispersion relation. To further investigate the optical properties of ZnO NRs/Cu₂O composite, Raman spectroscopy was carried out and the spectra was shown in Fig 5.30. The ZnO zone-center optical mode frequencies lie between 100 cm⁻¹ (12.5 meV) and 600 cm⁻¹ (75 meV). Obviously, in the highest frequency range (550 cm⁻¹ to 600 cm⁻¹), a group of 3 modes occurs. These are the closely spaced E1(LO), A1(LO), and B1(high). Similarly, the triple group E2(high), E1(TO), and A1(TO) appear between 370 cm⁻¹ and 440 cm⁻¹. The peaks at about 218, and 621 cm⁻¹ are attributed to the Ag, Bg (1), and Bg (2) modes of Cu₂O due to the vibrations of oxygen atoms [23]. Finally, the single eigen frequencies 100 cm⁻¹ and 250 cm⁻¹ belong to the E2(low) and the B1(low) mode, respectively [24].

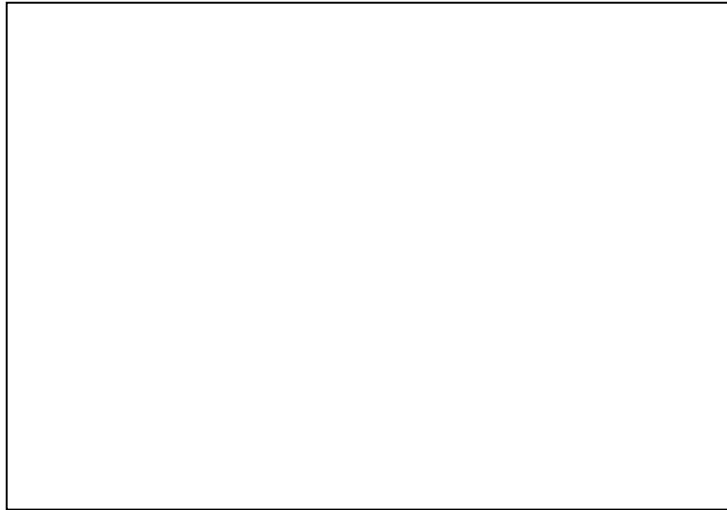


Figure 5.30 Raman spectrum of ZnO NRs/Cu₂O with a green (532 nm) laser as excitation source.

6.3. Characterization of ZnO/PbS core shell nanorods

During the initial stage, the bare ZnO NRs arrays were grown vertically on the ITO glass substrate with a hydrothermal growth process, their diameters are about 70–100 nm, as shown in Fig. 5.31.

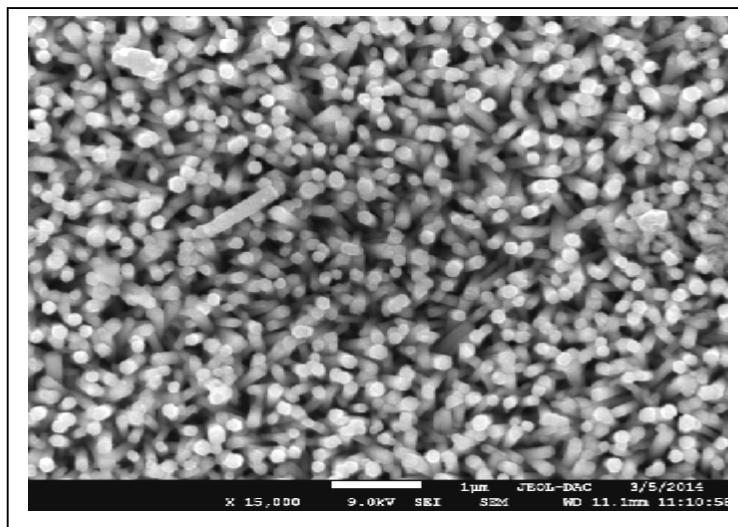


Figure 5.31 Top view SEM image of ZnO NRs arrays synthesized by the classical hydrothermal method.

Morphological changes are shown in Fig. 5.32 with different magnification after secondary growth process of PbS on ZnO NRs using ion exchange process.

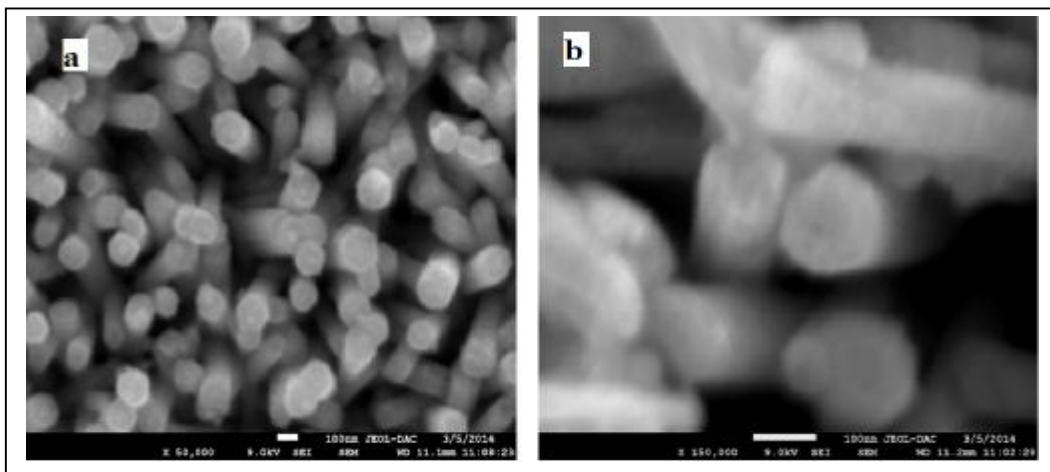


Figure 5.32 (a) SEM image of ZnO NRs with a diameter of about 70-100 nm after PbS coating. (b) The inset shows the magnified SEM image of the NRs.

It seems from Fig 5.32 (b) that PbS nanoparticles are deposited on the top and lateral of the ZnO NWs. In order to confirm the chemical composition of the obtained products, we have employed the EDX and XRD spectroscopy to analyze the synthesized film.

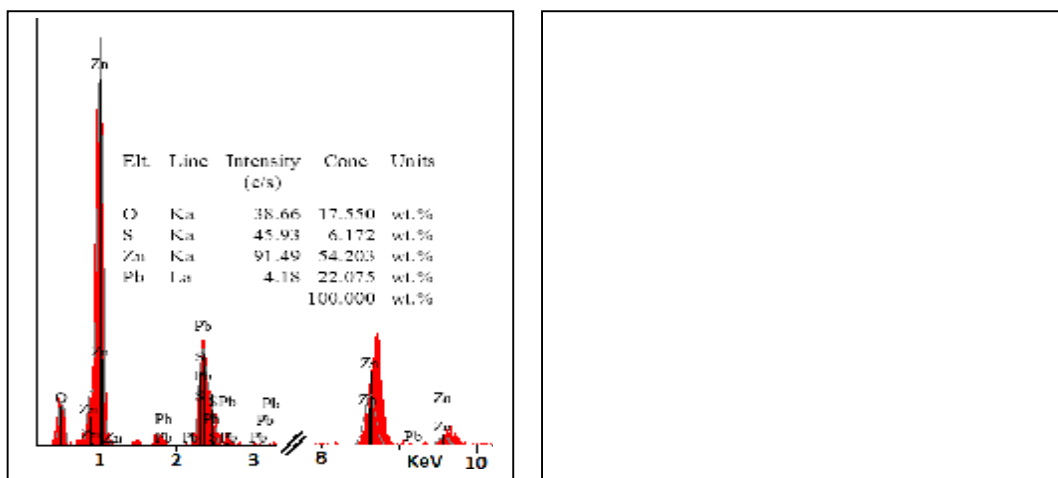


Figure 5.33 EDX (left) and XRD (right) spectrum of ZnO/PbS core shell nanorods.

The EDX results shown in Fig. 5.33 (left), indicate that the obtained ZnO/PbS CS NRs are mainly composed of Zn with 54.2%, O with 17.5%, Pb with 22% and S with 6.17% elements. The crystal structure of the prepared PbS sensitized ZnO NRs was confirmed by X-ray diffraction. It can be observed from Fig. 5.33 (right) that a typical wurtzite structure for ZnO was

formed. In comparison with standard powder diffraction pattern (PDF#65-3411), the very strong (0 0 2) peak reveals that c-axis is the fastest growth direction and the film presents rod structure, which agrees well with the SEM results. A small signal centered at 25.8° and a strong one at 31.2° corresponding to 111 and 200 reflections, are observed. The pattern was compared to the galena diffraction pattern (JCPDS File No.5-0592) which revealed that the PbS nanoparticles with cubic phase was formed in our structure. It has been reported that the PbS are typically in the cubic phase when prepared at about 450°C [25], but in this work, we fabricated the cubic phase PbS at room temperature [26, 27]. TEM technique has become an important characterization technique due to its high lateral spatial resolution and its capability to provide both image and diffraction information from a single sample. Therefore, TEM and high resolution transmission electron microscope (HRTEM) were used to further analyze the structure of the as grown ZnO/PbS CS.

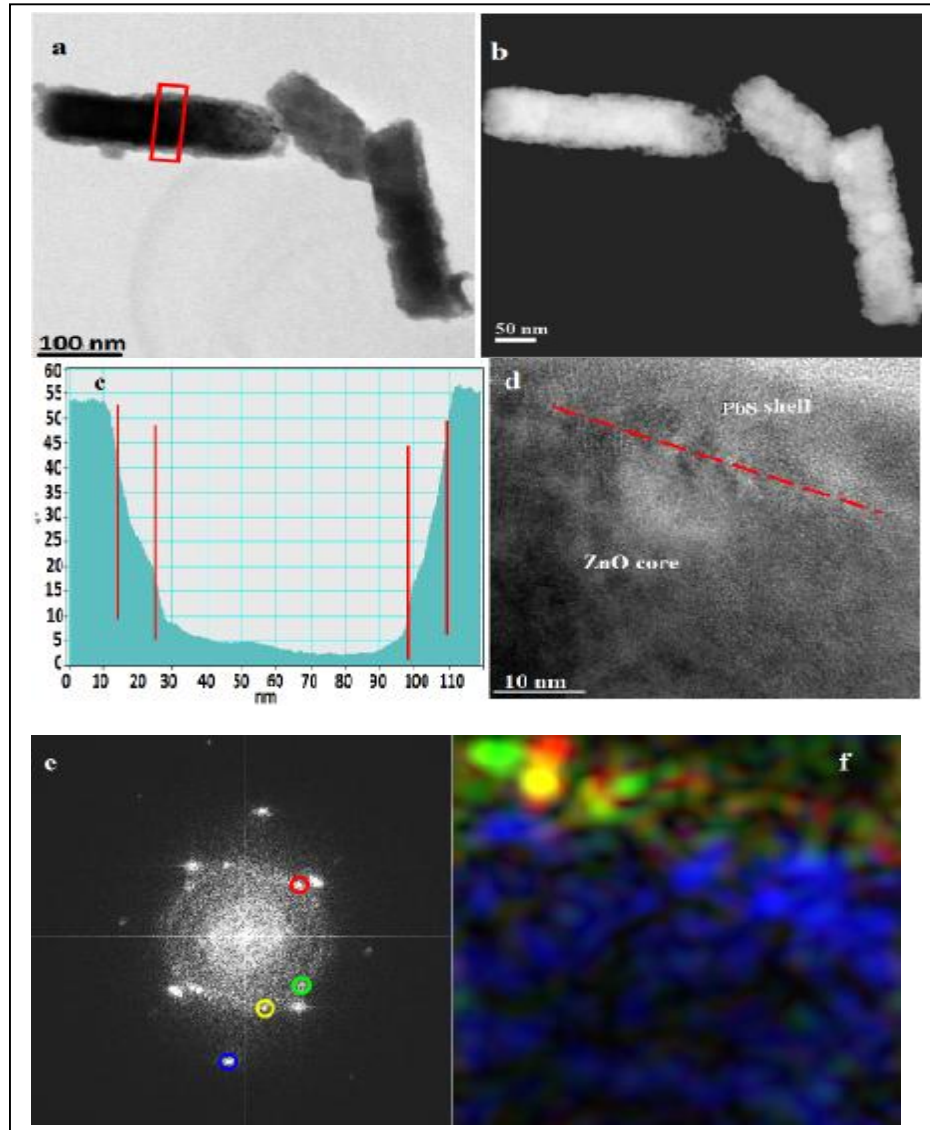


Figure 5.34 TEM characterization of ZnO/PbS core shell structure nanorods prepared by exchange ion process. (a) Bright field TEM image. (b) The high angle annular dark field HAADF-STEM image. (c) The line profile taken along the rectangle in red from (a). (d) The HRTEM image of ZnO nanorod core and PbS shell. (e) The Fourier Transform (FT) of selected-area of the core shell structured nanorods. (f) Map of the intensity obtained with the spatial frequencies circled in the FT with the same color.

By taking a conventional bright field TEM image of ZnO/PbS NRs CS as reported in Fig. 5.34 (a), one can observe that the dimensions and the appearance are very typical, with low aspect ratio. The image suggests that the rods are completely covered by a “shell” of a different material. The image from Fig. 5.34 (b) contains exactly the same rods but is taken with HAADF-STEM technique. This image shows that the rods are extremely rough. The line profile as shown in Fig. 5.34 (c), taken along the rectangle in red allows estimating the rod diameter and the shell

thickness, that are respectively around 75 and 12 nm. The inspection of the rod crystal structure by means of High resolution TEM analysis shows that the ZnO is single crystal while the shell layer is composed by PbS nanoparticles. In the HRTEM image of Fig. 5.34 (d), the red dashed line approximately indicates the separation line between the PbS shell and the ZnO rod. The Fourier Transform (FT), reproduces all the spatial frequencies, corresponding to the direct lattice periodicities present in the HRTEM image as shown in Fig. 5.34 (e). This technique allows identifying the ZnO NR as single crystal in the 01-11 projection. The presence of many reflections along a ring of radius 0.29 nm, corresponding to the most intense 200 reflection of PbS, tells us that the shell is composed by quantum dots randomly oriented. An average particle size of 4-5 nm can be estimated. In the frame of the Digital Micrograph software, it is possible, by selecting one reflection at a time in the FT and making the inverse FT procedure, to localize the particles that contributed to that reflection. By summing up the different images, the original HRTEM image can be reconstructed in false colors. An example of such reconstruction is shown in Fig.5.34 (f), where three regions that correspond to the reflections chosen in the FT are identified. The circle that selects the reflection in the FT has the same color of the identified region in the reconstruction.

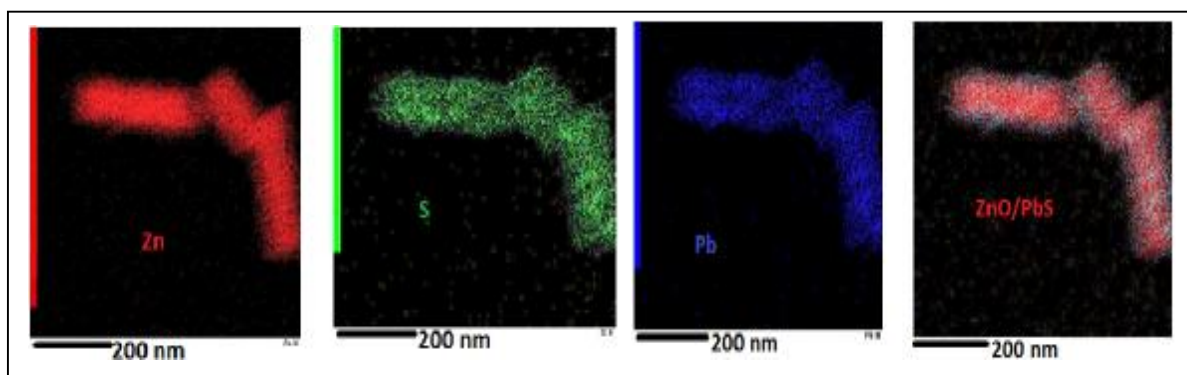


Figure 5.35 Elemental mapping images of Zn, S, Pb, and ZnO/PbS CS NR.

The distribution of the atomic species has been performed by the x-ray microanalysis, in the energy dispersion mode, by the x-ray mapping as shown in the Fig. 5.35. It is apparent that the S and Pb signals come from a larger region than the Zn signal. This is clear from the image where all the signals are superimposed. Further information about the surface defects of the ZnO NWs and ZnO/PbS CS NRs structure was obtained from the CL analysis as demonstrated in Fig. 5.36.

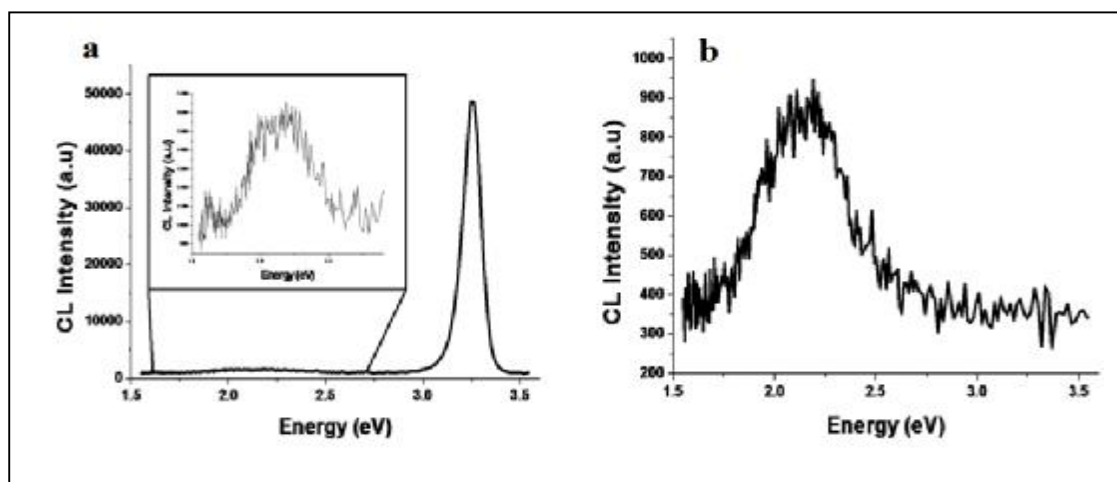


Figure 5.36 The CL spectra of: (a) Bare ZnO NRs and (b) ZnO/PbS CS NRs structure.

The ZnO NRs exhibit near band edge (NBE) UV emission at around 380 nm and a very low visible emission band in the green–yellow region as shown in Fig. 5.36 (a) indicating that our as-grown NWs have very good crystalline quality. This result is in good agreement with the XRD investigation. The UV band edge emission and green emission of ZnO nanocrystals have been reported by various researchers [28], and the color of emissions corresponds to various intrinsic or extrinsic ZnO defects and varies from one synthesis process to another. The observed NBE emission is due to free excitonic recombination, while green emission arises from the oxygen vacancy (V_o) states present on the surface [29]. The growth of a small PbS shell around these nanorods greatly influences their emission properties. Compared with the bare ZnO NRs, the surface modification with PbS shell leads to the quenching of the UV emission with a very low visible emission intensity around 2.1 eV. In comparison with conventional ZnO bulk structures, the nanorods can provide much more effective surface area for adsorption. Here, the surface adsorption property of ZnO NRs [30] could be modified by the diffusion of sulfide (S^{2-}) ions. This process might lead to adsorption of S^{2-} , particularly at special sites like edges and kinks or the oxygen ions may desorb. In all these processes, characteristic activation energies have to be overcome using temperature in the order of 50 °C. According to the experimental results described above, we propose that the possible formation mechanism of ZnO/PbS core shell nanorods relies on the ion exchange method. At the beginning of sulfidation reaction of ZnO nanorods in Na_2S solution, S^{2-} released from the decomposition of Na_2S reacts with the Zn^{2+} which slowly dissolved from the surface of ZnO nanorods [31] to produce ZnS

nanoparticles around the ZnO rods, because the solubility product constant (K_{sp}) of ZnO (6.8×10^{-17}) [32] is much larger than those of ZnS (3×10^{-25}) and PbS (10^{-28}). This implies that the arrays of ZnO nanorods can be used as sacrificial templates to synthesize more stable ZnS by anion exchange and further convert into PbS by cation exchange. In the second step, the ZnO/ZnS nanorods followed with partial conversion of ZnS to PbS through ion replacement of Zn^{2+} by Pb^{2+} in the ZnS shell.

The optical properties of nanocrystallites depend on their size and shape. Fig.5.37 shows the absorption spectra of ZnO NRs and ZnO/PbS NRs CS.

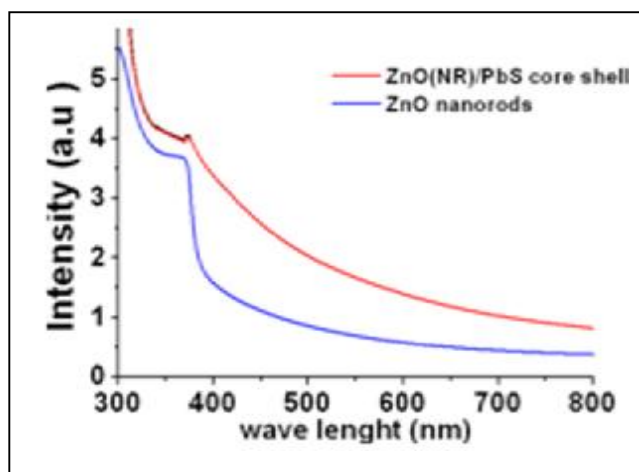


Figure 5.37 The absorption spectra of ZnO nanorods and ZnO/PbS nanorods core shell.

In this figure ZnO NRs absorb in the UV range at about 370 nm. The absorption wavelength for the ZnO/PbS CS NRs system was significantly red shifted from the one of ZnO NRs due to the addition of the PbS shell. The absence of a clear absorption peak in the spectrum can be due to the broad distribution of PbS QD sizes and strong scattering of the incident light by the non-uniform surface of the nanocrystal film. The absorption for the visible region is also increased a lot, ascribing to the narrow bandgap of PbS QDs [33]. This structure provides a material with good optical properties of the PbS QDs in the visible range.

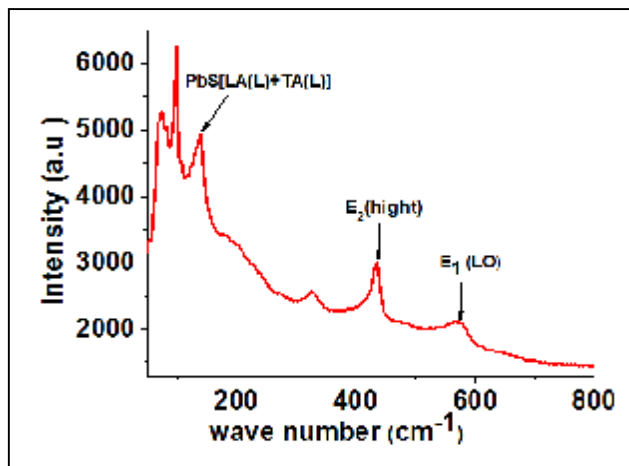


Figure 5.38 Room-temperature Raman spectra of ZnO/PbS core shell nanowire arrays.

Raman spectroscopy can provide valuable structural information of semiconductor nanostructures [34]. From the Raman spectroscopy results shown in Fig. 5.38, it can be clearly observed that there are three peaks located at 140 cm^{-1} , 437 cm^{-1} , and 581 cm^{-1} . The sharp, strong and dominant peak centered at 437 cm^{-1} is the nonpolar optical phonon E₂(high) mode of ZnO, which is a typical Raman active branch of wurtzite ZnO, and 581 cm^{-1} correspond to the ZnO multiplephonon (MP) scattering process and E₁ [longitudinal-optical (LO)] mode [35-36]. The sharp strong peak located at 140 cm^{-1} originates from the combination of longitudinal and transverse acoustic [LA(L)+TA(L)] modes of PbS [37].

6.4. Characterization of ZnO/CdS nanorods core shell

The ZnO surface can be considered as a catalyst for cadmium sulfide nucleation (heterogeneous nucleation). This is energetically preferred to the homogeneous one and can occur near equilibrium saturation conditions while homogeneous nucleation requires a supersaturated solution, and growth can occur close to the saturation concentration. In the case of heterogeneous nucleation, subcritical nuclei or even individual ions can adsorb onto the substrate because of both vander Waals and electrostatic interactions. It is known that CdS nucleation/growth mainly takes place through two different mechanisms: ion-by-ion (exchange ion) and hydroxide cluster. In the ion-by-ion mechanism, controlling the dissociation rate of sulfur precursors is crucial to promote heterogeneous nucleation instead of the homogeneous one. A rapid release of S²⁻ ions would invariably lead to CdS bulk precipitation ($K_{ps} = 10^{-28}$).

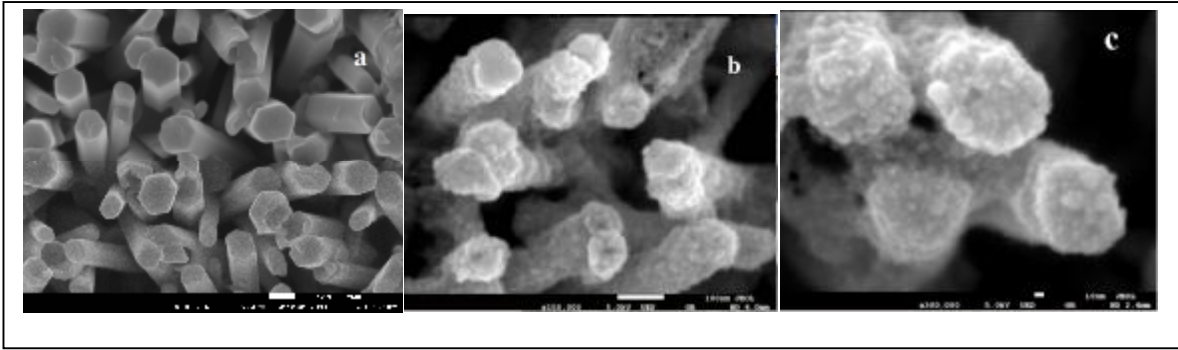


Figure 5.39 Top view of (a) bare ZnO nanorods, (b) after growth of conformal layer of nanocrystalline CdS. (c) a high magnification image of a ZnO nanorods coated with CdS nanoparticles

As described above, the ZnO/CdS core/shell nanorod arrays were fabricated by a facile two-step synthesis consisting of electrochemical growth of ZnO nanorod arrays followed by ion exchange method for depositing CdS nanocrystal shell layer. The morphology of the deposits was imaged by SEM. Figure 5.39 shows a SEM micrograph of ZnO nanorod arrays electrochemically grown onto an FTO substrate. The majority of the nanorods are vertically oriented to the substrate plane, and almost all of them show hexagonal faceted and smooth surfaces. The mean nanorod diameter was in the range 100–120 nm. The single crystallinity of the ZnO nanorods is evident from their faceted crystal habit and from XRD results (see below). Figure 5.39 (b-c) shows similar ZnO nanorod arrays after the CdS layer has been grown by the ion exchange technique. The ZnO nanorods in panel (b) do not retained their hexagonal geometry, but the roughened texture of the nanoscale CdS coating on these nanorods is also clearly visible. Moreover, the enlarged SEM image presented in figure 5.39 (c) revealed again, but in detail, that the surface of the nanorods became rough and grainy compared to the very smooth surface without the deposition of CdS (Fig. 5.39 (a)), and the diameters of the nanorod tips increased. So, these results suggest, that CdS nanocrystals could be successfully deposited onto the surface of the ZnO nanorods along their entire length, i.e. in a conformal way, to eventually form a ZnO/CdS core-shell structure. More structural details and the chemical composition of the ZnO/CdS nanorods were further examined by XRD and EDX, respectively as shown in Fig. 5.40.

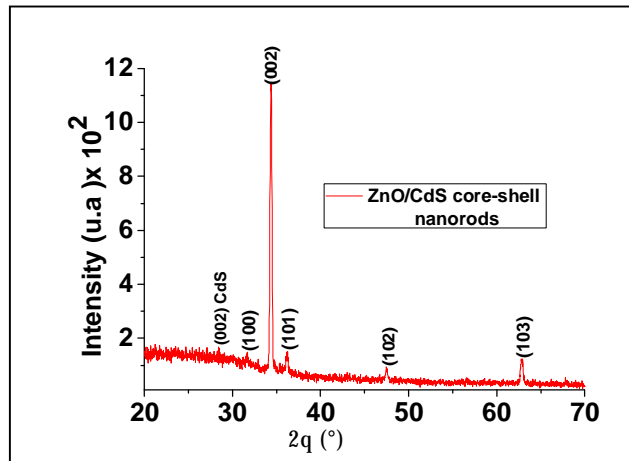


Figure 5.40 (a) XRD pattern and of ZnO/CdS core shell nanorods .

Figure 5.40 (a) shows a typical glancing-angle x-ray diffraction (GAXRD) pattern of a ZnO/CdS core/shell nanorod array sample. The x-ray diffraction peaks can be indexed to the hexagonal wurtzite ZnO structure (JCPDS file no. 05-0664 [38]) and cubic CdS structure (JCPDS file no. 01-089-0440 [39]). It can be appreciated that the obtained ZnO/CdS nanorod arrays share the structural characters of both ZnO and CdS because no other diffraction peaks were detected. Seven diffraction peaks corresponding to the (100), (002), (101), (102) and (103) planes of the ZnO hexagonal wurtzite structure, can be clearly identified in figure 5.40 (a). The large (0002) ZnO peak height again confirms that ZnO nanorods are highly crystalline with a hexagonal structure. On the other hand, only one diffraction peak, corresponding to the (002) plane of the cubic CdS phase, can be appreciated. This peak is small, suggesting that the thickness of the deposited CdS crystallites on the surface of the ZnO nanorods is very small. The EDX spectroscopy result shown in Fig. 5.40 (b) indicates that the obtained ZnO/CdS CS NRs are mainly composed of 73.8 % Zn, 23.3% O, 1.8% Cd and 1.1% S.

For more evaluation of ZnO/CdS core shell nanorods, optical properties, UV-vis, CL and Raman spectroscopy was used. As observed from Fig. 5.41 (b), the ZnO nanorods have a broad absorption in the UV region at 300–400 nm. The absorption intensity of the ZnO/CdS core–shell nanorod array increases after CdS nanoparticle deposition and its absorption is red-shifted to the range of 450–500 nm in the visible region. In order to determine the nature of transition and band gap of core–shell material, we have used the catodoluminescence (CL) spectroscopy and the results are given in the Fig. 5.41 (a).

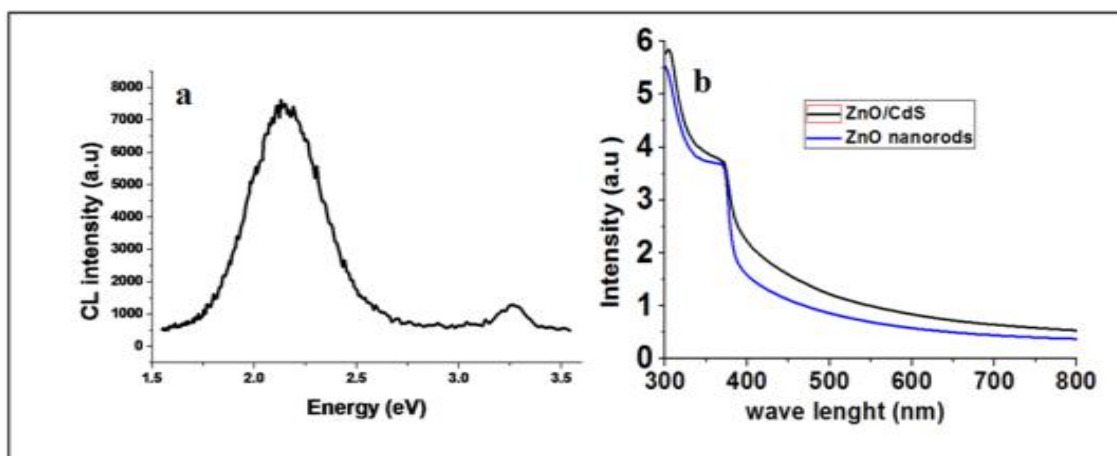


Figure 5.41 (a) CL of ZnO/CdS and (b) absorption spectra of bare ZnO and ZnO/CdS core shell nanorods

The CL spectra of ZnO/CdS nanorods core shell composite (Fig. 4.43 (a)) shows a common behavior with a UV peak centered at 380 nm (3.26 eV) caused by interband transition and a wide emission band, which covers almost the visible range, centered at 571 nm, corresponding to the green region. This strong and broad green emission peaked around 571 nm (2.1 eV) and a shoulder peak centered at 600 nm (600 nm), can be attributed to the defect states related emission band and the near band emission of CdS, respectively. These results could indicate that luminescence properties of the semiconductors are very sensitive to their structures and strongly dependent on the surface state and structural defects. According to the structural characteristics of the ZnO/CdS composites, the emission band shift in the CL spectrum could be attributed to the interaction between the two semiconductors of ZnO and CdS.

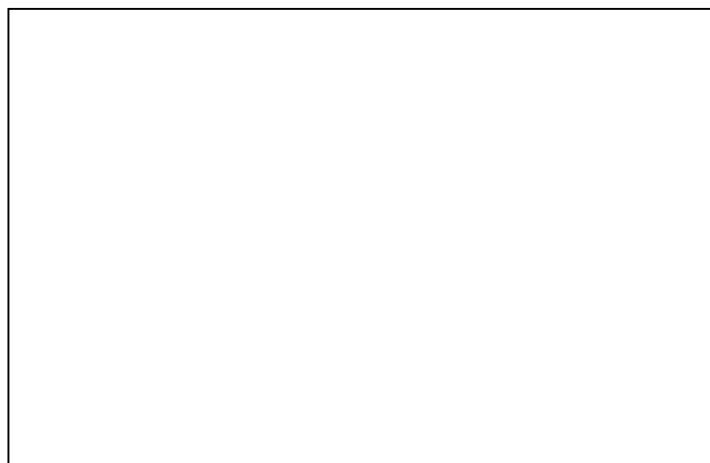


Figure 5.42 Raman spectrum of ZnO/CdS core shell nanorods deposited on ITO substrate.

The Raman spectrum of ZnO/CdS core shell nanorods deposited on ITO substrate was investigated as shown in figure 5.42 where the peak at 301 cm^{-1} corresponds to 1LO of CdS [40] and that at 438 cm^{-1} corresponds to E2 (LO) mode of ZnO [41].

7. Photoelectrochemical Cells

Next we assessed the photovoltaic performance of the ZnO/CdS, ZnO/PbS, ZnO/Cu₂O-CuO, core/shell nanorod arrays in a PEC system. In a PEC system, an appropriate redox couple in the electrolyte solution is used as the electron or hole acceptor in place of a metal or semiconductor contact [42, 43]. There are several advantages to use a liquid rather than a solid electrical contact to form a junction with the semiconductor when studying its photovoltaic behavior and to determine its optoelectronic parameters [42]. Among these advantages are the following: the ease by which the contact can be made and removed, and the complete contact made by the liquid, also making it suitable for rough and (as in the present case) nanostructured surfaces [42]. The PEC performance of ZnO/CdS, ZnO/PbS, ZnO/Cu₂O-CuO core/shell nanorod arrays was evaluated by recording the current as a function of applied potential in dark conditions and under simulated solar illumination in a 0.5 M K₂SO₄ aqueous solution in a typical three-electrode electrochemical cell, in which ZnO/CdS, ZnO/PbS, ZnO/Cu₂O-CuO core/shell nanorod arrays, Pt foil and SCE were used as the working electrode, counter electrode and reference electrode, respectively.

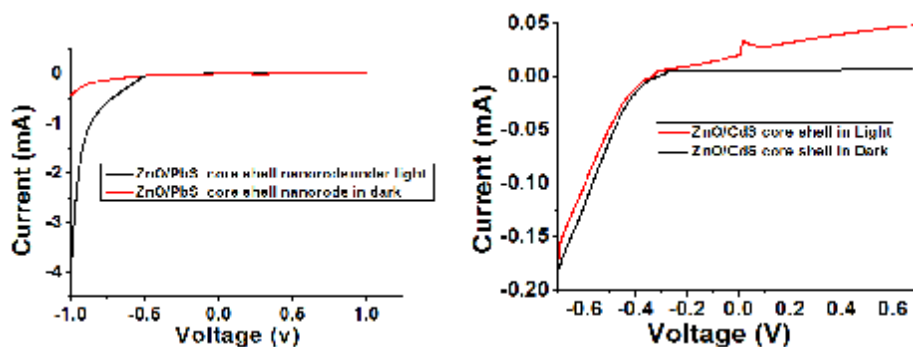


Figure 5.43 Current–voltage (I – V) characteristics of ZnO/CdS and ZnO/PbS core/shell nanorod array samples measured in a 0.5 M K₂SO₄ aqueous solution, in dark conditions and under simulated solar light illumination. Scan rate is 50 mV s^{-1} , Xenon light source power about 100 mW cm^{-2} .

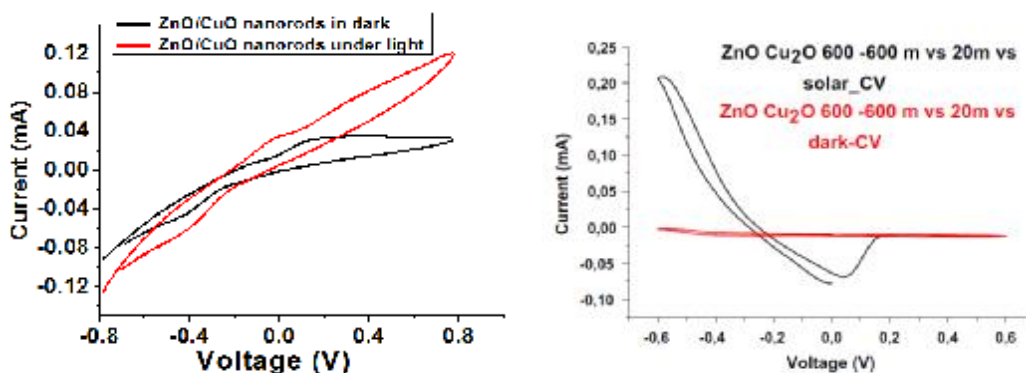


Figure 5.44 Current–voltage (I – V) (cyclic voltametric) characteristics of ZnO/CuO and ZnO/Cu₂O measured in a 0.5 M K₂SO₄ aqueous solution, in dark conditions and under simulated solar light illumination. Scan rate is 50 mV s⁻¹, Xenon light power source about 100 mW cm⁻².

Since the band gap of PbS, CdS, Cu₂O and CuO is relatively low (\approx 0.41 eV [43], 2.2 eV [44], 2eV [45] and 1.5 eV [46], respectively), it is essential to study photoelectrochemical properties of PbS, CdS, Cu₂O and CuO by coupling to a wide band gap semiconductor material (i.e. ZnO nanorods). ZnO is a wide band gap semiconductor material and absorb only a very small fraction of the visible light, therefore, the electrodes made from this material alone show a negligible photocurrent under visible light. The ZnO nanorods electrode consisted of nanosized crystallites which provided a high surface area to facilitate attachment of PbS, CdS, Cu₂O and CuO nanoparticles and absorb visible light. The band gap of the sensitizer (PbS, CdS, Cu₂O and CuO nanoparticles) increases due to size quantization effect. The repositioning of the conduction band of PbS, CdS, Cu₂O and CuO negative to that of ZnO is a direct result of quantum confinement. Under these conditions the charge injection takes place from the conduction band of sensitizer (PbS, CdS, Cu₂O and CuO) into that of ZnO nanorods. Once the photogenerated charges are injected, they transport through the metal oxide electrode and are subsequently collected at the FTO substrate.

The photocurrent of the electrode as measured under AM1.5 simulated light is: 4 mA, 0.17 mA, 0.1 mA and 0.2 mA for ZnO/PbS, ZnO/CdS, ZnO/CuO and ZnO/Cu₂O respectively which indicates that charge generation in the high band gap metal oxide phase under visible light is very low and significantly higher photocurrent density under the same illumination, suggesting the enhanced light absorption and charge injection after surface attachment of quantum dots on metal oxide surface.

In these kinds of heterojunctions, an n-type ZnO layer acts both as a host that chemically binds to the p-type Cu₂O which could help in efficient electron– hole separation. The number of

sensitizer nanoparticles loaded onto the n-type ZnO layer increases the sensitivity in the visible region. The prepared heterojunctions show improved photocurrent with respect to the literature results.

Conclusion

Zinc oxide nanorods have been synthesized by a simple chemical route using hexamine as a shape inducing reagent. CdS, PbS, CuO and Cu₂O nanoparticles were prepared using polyol method. The fabricated structures show a strong absorption in the UV-visible region and further analysis on the optical properties of the synthesized nanostructure confirms that it can be used as optoelectronic and nano-phonic devices.

General Conclusion

The materials investigated here in this thesis are CdS, PbS, CuO-Cu₂O and ZnO, which are the earth-abundant materials. A variety of ZnO nanorods and nanoparticles of CdS, PbS, CuO-Cu₂O nanostructures were prepared by a simple and low cost hydrothermal and polyol method. The structural, morphological, optical and photoelectronchemical properties of the as deposited nanostructures were investigated in detail. The effect of different hydrothermal conditions, especially the pH of the growth solution, growth temperature, growth time, and the precursor concentration, on the morphology and structural properties of ZnO nanorods were studied. The optimization of the growth conditions, realizing the size controllable growth and revealing the growth mechanism, has been presented for ZnO nanorods. This method preserves some main advantages that it is low temperature and does not require any harsh fabrication process on the target substrates which enable the use of nonconventional substrates such as plastic, polymer, fabric and paper. Low cost production is the main advantage for any product to compete in the market and ZnO nanorods being solution processable provides much potential to become the choice for cheap devices. In addition, devices with ZnO nanorods like heterostructure of ZnO nanorods/CdS, PbS, CuO-Cu₂O exhibit better performance due to a better interfacial contact, having fewer defects and improved absorption feature. Therefore, we have studied ZnO nanorods-based heterojunction photoelectrochemical property in this work. Based on the experimental results and discussions elaborated in the chapter 4, a few conclusions can be drawn for this thesis work:

- ü Large scale of ZnO nanorods, nanoparticles of CdS, PbS Cu₂O and CuO have been successfully synthesized using hydrothermal and polyol method and using innovative combination between the chemical route (hydrothermal) and exchange ions to prepare core shell p-n heterostructure.
- ü The effect of pre-annealing condition of ZnO seed layer on the growth of ZnO nanorods arrays was systematically studied. It shows that seed layer could lead to more uniform and well-aligned ZnO nanorods. In addition, increasing of annealing time and thickness of the seed layer leads to the increase of the ZnO nanorods diameter.

- ü The grown ZnO nanorods arrays were relatively well aligned with a preferential growth direction along [0002]. Dramatic change in the ZnO nanorods structure could occur by heating the obtained ZNRs (with one step preparation) at 350 °C (10 min). Adding seed NPs and subsequently applying hydrothermal growth with a DAP aqueous solution lead to the formation of core-shell and flower-like ZnO Instead of classical nanorods. Therefore, heating followed by a second seed step and hydrothermal process can lead to more complex ZNR structuring.

- ü ZnO with a band gap ~ 3.3 eV at room temperature has higher absorption efficiency at wavelength ~200nm- 380nm. Compared to ZnO, CdS, PbS and Cu₂O-CuO which have a much smaller band gap around 2.4 eV, 0.4 eV, 2-1.2 eV respectively, with a much higher absorption efficiency at wavelength ~ 300 nm- 600 nm. Thus, ZnO/Cu₂O-CuO, ZnO/CdS and ZnO/Pbs core-shell nanorods arrays exhibit much better absorption efficiency in visible region compared to pure ZnO nanorods arrays.

- ü The photovoltaic performance of ZnO/CdS, ZnO/PbS ZnO/Cu₂O-CuO core-shell nanorod arrays was evaluated in a PEC solar cell configuration with a K₂SO₄ electrolyte under simulated solar light. A 40-fold enhancement in photoactivity is observed using ZnO/PbS core/shell nanorods architectures compared to other samples.

This structure is of great importance because it enables fabrication of optoelectronic and nano-phonic devices with improved performance at very low cost. This design has also potential for cheap photovoltaic devices but to achieve all these goals further research is necessary. Efforts are still under way in our laboratory to use those nanostructured materials for the above mentioned purposes including photoelectrochemical cells.

The results presented here not only provide a method for large area fabrication of ZnO complex nanostructure and heterostructure with low cost and to implement in flexible devices but also open a way to fabricate optimized nanostructures of other nanomaterials on nonconventional substrates by the hydrothermal method.

REFERENCE

Chapter 1

- [1] J.G. Lu, P. Chang, Z. Fan, *R:Reports*, 52 (2006) 49-91.
- [2] S. Xu, Z.L. Wang, *Nano Research*, 4 (2011) 1013-1098.
- [3] S. Kishwar, M.H. Asif, O. Nur, M. Willander, P.O. L, *Nanoscale research letters*, 5 (2010) 1669-1674.
- [4] A. Zainelabdin, S. Zaman, G. Amin, O. Nur, M. Willander, *Crystal Growth & Design*, 10 (2010) 3250-3256.
- [5] A. Manekkathodi, M.-Y. Lu, C.W. Wang, L.-J. Chen, *Advanced Materials*, 22 (2010) 4059-4063.
- [6] N. Bano, S. Zaman, A. Zainelabdin, S. Hussain, I. Hussain, O. Nur, M. Willander, *Journal of Applied Physics*, 108 (2010) 043103-043105.
- [7] B. Postels, M. Kreye, H.H. Wehmann, A. Bakin, N. Boukos, A. Travlos, A. Waag, *Superlattice Microst*, 42 (2007) 425-430.
- [8] L. Schmidt-Mende, J.L. MacManus-Driscoll, *ZnO – nanostructures, defects, and devices*, *Materials Today*, 10 (2007) 40-48.
- [9] J.R. Sadaf, M.Q. Israr, O. Nur, M. Willander, Y. Ding, Z.L. Wang, *Nanoscale research letters*, 6 (2011) 513.
- [10] K. Gurunathan, A.V. Murugan, R. Marimuthu, U.P. Mulik, D.P. Amalnerkar, *Mater Chem Phys*, 61 (1999) 173-191.
- [11] G. Amin, M. Sandberg, A. Zainelabdin, S. Zaman, O. Nur, M. Willander, *J Mater Sci*, 47 (2012) 4726-4731.
- [12] G. John, *Richard Feynman: A Life in Science*, Dutton 1997-170
- [13] R. R. Allison, H. C. Mota, V. S. Bagnato and C. H. Sibata, *Photodiagnosis and Photodynamic Therapy* 5, 19 (2008).
- [14] O. M. Koo, Israel Rubinstein and Hayat Onyuksel, *Nanomedicine: Nanotechnology, Biology and Medicine* 1, 193 (2005).
- [15] W. A. Tisdale, K. J. Williams, B. A. Timp, D. J. Norris, E. S. Aydil and X. -Y Zhu,

Science 328, 1543 (2010).

[13] S. -L Jeng, J. -C Lu and K. Wang, IEEE Trans. Reliab. 56, 401 (2007).

[14] Guozhong Gao, Nanostructure & Nanomaterials Synthesis, Properties & Application, Imperial College Press (2004).

[15] Kittel, C. Introduction to Solid State Physics. John Wiley and Sons Inc., 8th edition, (2005).

[16] Hook, J. R. and Hall, H. E. Solid state Physics. John Wiley and Sons Inc., 2nd edition, (1995).

[17] Bastard, G. Wave mechanics applied to semiconductor heterostructures. Halsted Press, 1st edition, (1988).

[18] Norris, D. J. Semiconductor and Metal Nanocrystals: Synthesis and Electronic and Optical Properties, chapter Electronic Structure in Semiconductor Nanocrystals, 65–102. Marcel Dekker Inc. (2004).

[19] A. Euteneuer, R. Hellmann, R. Gobel, S. Shevel, V. Vozny, M. Vytrykhivsky, W. Petri, C. J. Klingshirn, J. Crystal Growth., 1998, 184/185, 1081.

[20] K. Shimakawa, A. Kolobov, S. R. Elliot, Adv. Phys., 1995,44,475.

[21] K. D. Kepler, G. C. Lisensky, M. Patel, L. A. Sigworth, A. B. Ellis, J. Phys. Chem., 1995,99, 16011.

[22] C. Donega, S. G. Hickey, S. F. Wuister, D. Vanmaekelbergh, A. Meijerink, J.Phys. Chem., B 2003, 107,489.

[23] B. O. Regan, M. Gratzel, Nature, 1991,353,373.

[24] M. Gratzel, A. J. Frank, J. Phys. Chem., 1982,86,2964.

[25] A. Gafeldt, M. Gratzel, Chem. Rev., 1995,95,49.

[26] S. Iijima, Proceedings of the IEEE Micro Electro Mechanical Systems (MEMS) 520 (1998).

[27] Y. Wu, R. Fan and P. Yang, Nano Letters 2, 83 (2002).

[28] C. Jagadish, S.J. Pearton, Elsevier, Amsterdam; London, 2006.

[29] A.B. Djurišić, A.M.C. Ng, X.Y. Chen, Prog Quant Electron, 34 (2010) 191-259.

[30] N.H. Alvi, K. Ul Hasan, O. Nur, M. Willander, Nanoscale research letters, 6 (2011) 130.

[31] A.B. Djurišić, Y.H. Leung, K.H. Tam, L. Ding, W.K. Ge, H.Y. Chen, S. Gwo, Applied Physics Letters, 88 (2006) 103107.

- [32] M. Willander, O. Nur, Q.X. Zhao, L.L. Yang, M. Lorenz, B.Q. Cao, J.Z. Pérez, C. Czekalla, G. Zimmermann, M. Grundmann, A. Bakin, A. Behrends, M. Al-Suleiman, A. El-Shaer, A.C. Mofor, B. Postels, A. Waag, N. Boukos, A. Travlos, H.S. Kwack, J. Guinard, D.L.S. Dang, *Nanotechnology*, 20 (2009) 332001.
- [33] A.B. Djurišić, Y.H. Leung, K.H. Tam, Y.F. Hsu, L. Ding, W.K. Ge, Y.C. Zhong, K.S. Wong, W.K. Chan, H.L. Tam, K.W. Cheah, W.M. Kwok, D.L. Phillips, 18 (2007) 095702.
- [34] Q.X. Zhao, P. Klason, M. Willander, H.M. Zhong, W. Lu, J.H. Yang, , *Applied Physics Letters*, 87 (2005) 211912.
- [35] K.H. Tam, C.K. Cheung, Y.H. Leung, A.B. Djurišić, C.C. Ling, C.D. Beling, S. Fung, W.M. Kwok, W.K. Chan, D.L. Phillips, L. Ding, W.K. Ge, *The Journal of Physical Chemistry B*, 110 (2006) 20865-20871.
- [36] M.H. Asif, S.M.U. Ali, O. Nur, M. Willander, U.H. Englund, F. Elinder, *Biosensors and Bioelectronics*, 26 (2010) 1118-1123.
- [37] S.M. Usman Ali, N.H. Alvi, Z. Ibupoto, O. Nur, M. Willander, B. Danielsson, *Sensors and Actuators B: Chemical*, 152 (2011) 241-247.
- [38] A.P. Moura, L.S. Cavalcante, J.C. Sczancoski, D.G. Stroppa, E.C. Paris, A.J. Ramirez, J.A. Varela, E. Longo, *Advanced Powder Technology*, 21 (2010) 197-202.
- [39] G. Filipič, U. Cvelbar, *Copper oxide nanowires: a review of growth*, *Nanotechnology*, 23 (2012) 194001.
- [40] Y. Li, Y. Wei, G. Shi, Y. Xian, L. Jin, *Electroanalysis*, 23 (2011) 497-502.
- [41] *Facile Synthesis of Colloidal CuO Nanocrystals for Light-Harvesting Applications*, *Journal of Nanomaterials*, 2012 (2012).
- [42] K.K. Dey, A. Kumar, R. Shanker, A. Dhawan, M. Wan, R.R. Yadav, A.K. Srivastava, *RSC Advances*, 2 (2012) 1387-1403.
- [43] S.-D. Seo, Y.-H. Jin, S.-H. Lee, H.-W. Shim, D.-W. Kim, *Nanoscale research letters*, 6 (2011) 397.
- [44] X. Gou, G. Wang, J. Yang, J. Park, D. Wexler, *J Mater Chem*, 18 (2008) 965-969.
- [45] J. Chen, K. Wang, L. Hartman, W. Zhou, *The Journal of Physical Chemistry C*, 112 (2008) 16017-16021.
- [47] Lide, D. R., ed. (2005). *CRC Handbook of Chemistry and Physics* (86th ed.). Boca Raton (FL): CRC Press. ISBN 0-8493-0486-5.

- [48] Vaughan, D. J.; Craig, J. R. (1978). *Mineral Chemistry of Metal Sulfides*. Cambridge: Cambridge University Press. ISBN 0-521-21489-0.;
- [49] C. Michael Hogan. 2011. Sulfur. *Encyclopedia of Earth*, eds. A. Jorgensen and C. J. Cleveland, National Council for Science and the Environment, Washington DC
- [50] Charles A. Sutherland, Edward F. Milner, Robert C. Kerby, Herbert Teindl, Albert Melin, Hermann M. Bolt (2005). Lead. in *Ullmann's Encyclopedia of Industrial Chemistry*. Weinheim: Wiley-VCH. doi:10.1002/14356007.a15_193.pub2.
- [51] Putley, E H; Arthur, J B (1951). "Lead Sulphide – An Intrinsic Semiconductor". *Proceedings of the Physical Society. Series B64*: 616. doi:10.1088/0370-1301/64/7/110.
- [52] Egon Wiberg, Arnold Frederick Holleman (2001) *Inorganic Chemistry*, Elsevier ISBN 0-12-352651-5
- [53] Fred Ibbotson (2007), *The Chemical Analysis of Steel-Works' Materials*, Read Books, ISBN 1-4067-8113-4
- [54] Paul Klocek (1991), *Handbook of Infrared Optical Materials*, CRC Press ISBN 0-8247-8468-5
- [55] Hugh MacDonald Smith (2002). *High Performance Pigments*. Wiley-VCH. ISBN 3-527-30204-2.
- [56] Uda, H; Yonezawa, H; Ohtsubo, Y; Kosaka, M; Sonomura, H (2003). *Solar Energy Materials and Solar Cells* 75 (1–2): 219. doi:10.1016/S0927-0248(02)00163-0.
- [57] Reisfeld, R (2002). *Journal of Alloys and Compounds* 341 (1–2): 56. doi:10.1016/S0925-8388(02)00059-2.
- [58] Moon, B; Lee, J; Jung, H (2006). *Thin Solid Films*. 511-512: 299. doi:10.1016/j.tsf.2005.11.080.
- [59] Goto, F; Shirai, Katsunori; Ichimura, Masaya (1998). *Solar Energy Materials and Solar Cells* 50 (1–4): 147. doi:10.1016/S0927-0248(97)00136-0.
- [60] U.S. Patent 4,086,101 Photovoltaic cells, J.F. Jordan, C.M. Lampkin Issue date: April 25, 1978
- [61] U.S. Patent 3,208,022, Y.T. Sihvonen, issue date: September 21, 1965
- [62] Wanrooij, P. H. P.; Agarwal, U. S.; Meuldijk, J.; Kasteren, J. M. N. van; Lemstra, P. J. (2006). *Journal of Applied Polymer Science* 100 (2): 1024. doi:10.1002/app.22962.
- [63] Mario Schiavello (1985) *Photoelectrochemistry, Photocatalysis, and Photoreactors: Fundamentals and Developments* Springer ISBN 90-277-1946-2

- [64] D. Lincot, Gary Hodes Chemical Solution Deposition of Semiconducting and Non-Metallic Films: Proceedings of the International Symposium The Electrochemical Society, 2006 ISBN 1-56677-433-0
- [65] Wells A.F. (1984) Structural Inorganic Chemistry 5th edition Oxford Science Publications ISBN 0-19-855370-6
- [66] Antonio Luque, Steven Hegedus, (2003), Handbook of Photovoltaic Science and Engineering John Wiley and Sons ISBN 0-471-49196-9
- [67] Reynolds, D.; Leies, G.; Antes, L.; Marburger, R. (1954). Physical Review 96 (2): 533. doi:10.1103/PhysRev.96.533.
- [68] C. Fouassier,(1994), Luminescence in Encyclopedia of Inorganic Chemistry, John Wiley & Sons ISBN 0-471-93620-0
- [69] Minkus, Wilfred (1965). Physical Review 138 (4A): A1277. doi:10.1103/PhysRev.138.A1277.
- [70] Smith, Roland (1957). Physical Review 105 (3): 900. doi:10.1103/PhysRev.105.900.
- [71] Akimov, Yu A; Burov, A A; Drozhbin, Yu A; Kovalenko, V A; Kozlov, S E; Kryukova, I V; Rodichenko, G V; Stepanov, B M; Yakovlev, V A (1972). Soviet Journal of Quantum Electronics 2 (3): 284. doi:10.1070/QE1972v002n03ABEH004443.
- [72] Agarwal, Ritesh; Barrelet, Carl J.; Lieber, Charles M. (2005). Nano Letters 5 (5): 917. doi:10.1021/nl050440u. PMID 15884894.
- [73] Karl-Heinz Schulte-Schrepping, in Ullmann's Encyclopedia of Industrial Chemistry, 2007 Wiley-VCH, Weinheim. doi:10.1002/14356007.a04 499.
- [74] H. Zhao et al, Thin Solid Films, Vol. 517, No. 7 (2009) pp. 2365-2369, [1] doi:10.1016/j.tsf.2008.11.041
- [75] P.K. Weimar, Proc. IRE, Vol. 50, No. 6 (1962) pp. 1462-1469, [2] doi:10.1109/JRPROC.1962.288190
- [76] R. M. Christie 2001 Colour Chemistry, p. 155 Royal Society of Chemistry ISBN 0-85404-573-2
- [77] Bjornberg A. (1963), Arch Dermatol. 1963 Sep;88:267-71. PMID 14043617
- [78] Sidney Perkowitz, 1998, Empire of Light: A History of Discovery in Science and Art Joseph Henry Press, ISBN 0-309-06556-9
- [79] W. Stanley Taft, James W. Mayer, Richard Newman, Peter Kuniholm, Dusan Stulik (2000) The Science of Paintings, Springer, ISBN 0-387-98722-3
- [80] Larry L. Barton 1995 Sulfate reducing bacteria, Springer, ISBN 0-306-44857-2

[81] Sweeney, Rozamond Y.; Mao, Chuanbin; Gao, Xiaoxia; Burt, Justin L.; Belcher, Angela M.; Georgiou, George; Iverson, Brent L. (2004). *Chemistry & Biology* 11 (11): 1553. doi:10.1016/j.chembiol.2004.08.022. PMID 15556006.

Chapter 2

- [1] Asahi, R., Morikawa, T., Ohwaki, T., Aoki, K., Taga, Y. *Science* 295, 627–627 (2002)
- [2] Maruska, H.P., Ghosh, A.K. *Solar Energy Mater.* 1, 237–247 (1979)
- [3] Salvador, P. *Solar Energy Mater.* 6, 241–250 (1982)
- [4] Henrich, V.E., Cox, P.A.: *The surface science of metal oxides*. Cambridge University Press, Cambridge (1994)
- [5] Kato, H., Kudo, A. *J. Phys. Chem. B* 106, 5029–5034 (2002)
- [6]. Howe, A.T., Hawkins II, R.T., Fleisch, T.H. *J. Electrochem. Soc.* 133, 1369–1375 (1986)
- [7] Pierret, R.F.: *Semiconductor Device Fundamentals*. Addison Wesley, Reading (1996)
- [8] Morrison, S.R. Plenum, New York (1980)
- [9] Reichman, J.: The current–voltage characteristics of semiconductor-electrolyte junction photo-voltaic cells. *Appl. Phys. Lett.* 36, 574–577 (1980)
- [10] Hagfeldt, A., Bjorksten, U., Grätzel, M. *J. Phys. Chem.* 100, 8045–8048 (1996)
- [11] Brus, L.E. *J. Chem. Phys.* 80, 4403–4409 (1984)

Chapter 3

- [1] Byrappa, K.; Yoshimura, M., *Handbook of hydrothermal technology*. Noyes Publications: Norwich, N.Y., 2001.
- [2] Demazeau, G., Solvothermal reactions. *J. Mater. Sci.* 2008, 43 (7), 2104-2114.
- [3] Yoshimura, M.; Byrappa, K. *J. Mater. Sci.* 2008, 43 (7), 2085-2103.
- [4] Feng, S. H.; Xu, R. R., *New materials in hydrothermal synthesis*. *Accounts Chem. Res.* 2001, 34 (3), 239-247.
- [5] Rabenau, A., The role of hydrothermal synthesis in preparative chemistry. *Angew. Chem. Int. Ed. Engl.* 1985, 24 (12), 1026-1040.
- [6] Yoshimura, M., Importance of soft solution processing for advanced inorganic materials. *J. Mater. Res.* 1998, 13 (4), 796-802.
- [7] Bacsá, R.; Ravindranathan, P.; Dougherty, J. P. *J. Mater. Res.* 1992, 7 (2), 423-428.

- [8] Liu, L. M.; Wang, X. Q.; Bontchev, R.; Ross, K.; Jacobson, A. J. *J. Mater. Chem.* 1999, 9 (7), 1585-1589.
- [9] Wang, X. Q.; Liu, L. M.; Bontchev, R.; Jacobson, A. J. *Chem. Commun.* 1998, (9), 1009-1010.
- [10] Yoshimura, M.; Suchanek, W. *Solid State Ion.* 1997, 98 (3-4), 197-208.
- [11] Herrero, M.; Benito, P.; Labajos, F. M.; Rives, V. *Catal. Today* 2007, 128 (3-4), 129-137.
- [12] Hu, X. L.; Yu, J. C., *Continuous. Adv. Funct. Mater.* 2008, 18 (6), 880-887.
- [13] Huang, J. F.; Xia, C. K.; Cao, L. Y.; Wu, J. P.; He, H. Y. *Am. Ceram. Soc. Bull.* 2007, 86 (11), 9201-9204.
- [14] Newalkar, B. L.; Chiranjeevi, T.; Choudary, N. V.; Komarneni, S. J. *Porous Mat.* 2008, 15 (3), 271-276.
- [15] Sreeja, V.; Joy, P. A. *Mater. Res. Bull.* 2007, 42 (8), 1570-1576.
- [16] Komarneni, S.; Roy, R.; Li, Q. H. *Mater. Res. Bull.* 1992, 27 (12), 1393-1405.
- [17] L.E. Scriven, in C. J. Brinker, D. E. Clark and D. R. Ulrich (eds.), *Better Ceramics Through Chemistry 111*, Materials Research Society, Pittsburgh, PA, 1988, pp. 717-729.
- [18] A.J. Hurd, in H. Bengna (ed.), *The Colloidal Chemistry of Silica (ACS Adv. in Chem. Series)* to be published.
- [19] L.D. Landau and B. G. Levich, *Acta Physicochim. U.R.S.S.*, 17 (1942) 42-54.

Chapter 4

- [1] Vayssieres L, Keis K, Lindquist SE, Hagfeldt A. *J Phys Chem B* 2001, 105:3350.
- [2] S. Chowdhury, D. Mohanta, G.A. Ahmed, S.K. Dolui, D.K. Avasthi, and A. Choudhury // *J. Luminescence* 114, p. 95 (2005).
- [3] S. Chowdhury, D. Mohanta, G.A. Ahmed, S.K. Dolui, D.K. Avasthi, and A. Choudhury // *Nucl. Instrum. and Meth. B* 240, p. 690 (2005).
- [4] D. Mohanta, S.S. Nath, A. Bordoloi, S.K. Dolui, and A. Choudhury // *J. Appl. Phys.* 92, p. 7149 (2002).
12. D. Mohanta, S.K. Dolui, and A. Choudhury // *Ind. J. Phys.* 75, p. 53 (2001).
- [5] Tsuji M., Nishizawa, Y., Matsumoto, K., Kubokawa, M., Miyamae, N., and Tsuji. *Materials Letters*, 2006, 60 (6), 834-838.

[6] Zhimao Yang, Shaodong Sun, Chuncai Kong, Xiaoping Song, and Bingjun Ding. Journal of Nanomaterials Volume 2010, Article ID 710584, 11 pages doi:10.1155/2010/710584.

Chapter 5

[1] Yao, B. D.; Chan, Y. F.; Wang, N. Appl. Phys. Lett. 2002, 81, 757–759.

[2] Seung H. Ko, Inkyu Park, Heng Pan, Nipun Misra, Matthew S. Rogers, Costas P. Grigoropoulos, and Albert P. Pisano. Applied Physics Letters 92, 154102, 2008.

[3] Bagnall DM, Chen YF, Zhu Z, Yao T, Koyama S, Shen MY, Goto T. Appl Phys Lett 1998, 73:1038.

[4] Cheng H-M, Chiu W-H, Lee C-H, Tsai S-Y, Hsieh W-F. J Phys Chem C 2008, 112:16359.

[7] Ashkenov N, Mbenkum B N, Bundesmann C, Riede V, Lorenz M, Spemann D, Kaidashev E M, Kasic A, Schubert M, Grundmann M, Wagner G, Neumann H. J. Appl. Phys. 2003, 93: 126.

[8] V. A. Fonoberov and A. A. Balandin, Phys. Rev. B 70, 233205 2004.

[9] V. A. Fonoberov and A. A. Balandin, Phys. Status Solidi C 1, 2650 2004.

[10] V. A. Fonoberov and A. A. Balandin, J. Phys.: Condens. Matter 17, 1085 2005.

[11] Y.F. Zhu, G.H. Zhou, H.Y. Ding, A.H. Liu, Y.B. Lin, Y.W. Huaian 223003, China. Superlattices and Microstructures 50 (2011) 549–556).

[12] M. Hangyo, S. Nakashima, Y. Hamada, T. Nishio, Y. Ohno, Phys. Rev. B 48 (1993) 11291–11297.

[13] Chuu D R and Dai C M 1992 Phys. Rev. B 45 11805.

[14] L.E. Brus, J. Chem. Phys., 79 (1983) 5566..

[15] J. Wang, A. Suna, W. Mahler, and R. Kasowski, J. Chem. Phys., 87, No. 12, 7315-7322 (1987).

[16] M.T. Nenadovic, M.I. C. omor, V. Vasic, O.I. Mic ic, J. Phys. Chem. 94 (1990) 6390.

[17] Zhimao Yang, Shaodong Sun, Chuncai Kong, Xiaoping Song, and Bingjun Ding. Journal of Nanomaterials Volume 2010, Article ID 710584, 11 pages doi:10.1155/2010/710584.

[18] Chi-Hsiu Chang and Yuh-Lang Lee. Applied Physics Letters 91, 053503 2007.

[19] D. W. Banheman et al. Journal of Photochemistry and Photobiology A: Chemistry, Volume 148, Number 1, 31 May 2002, pp. 283-293(11).

- [20] H. Chen, A.D. Pasquier, G. Saraf, J. Zhong, Y. Lu, *Semicond. Sci. Technol.* 23 (2008) 045004.
- [21] Yu T, Zhao X, Shen Z X, Wu Y H and Su W H 2004 *J. Cryst. Growth* 268 590,
- [22] M. Blosi,^a S. Albonetti ^b, M. Dondic, C. Martelli ^b, G. Baldi. *Journal of Nanoparticle Research*. 10.1007/s11051-010-0010-7).
- [23] Li, *Nano Lett.*, 2009, 9, 2331. H. Sekhar , D. NarayanaRao *J Nanopart Res* (2012) 14:976 DOI 10.1007/s11051-012-0976-4.
- [24] J. Serrano, F. Widulle, A. H. Romero, M. Cardona, R. Lauck, and A. Rubio, *phys. stat. sol. b* 235, 260 (2003)
- [25] P. Wang, L. Wang, B. Ma, B. Li, Y.J. Qiu, *J. Phys. Chem. B* 110 (2006) 14406.],
- [26] Liu, Zhifeng Liu , Yabin Li, Jing Ya, Lei E, Li An. *Applied Surface Science* 257 (2011) 7041–7046).
- [27] M. Mozafari, F. Moztafzadeh. *Micro & Nano Letters*, 2011, Vol. 6, Iss. 3, pp. 161–164. doi: 10.1049/mnl.2010.0203
- [28] Cao, X. B.; Zhao, C.; Lan, X. M.; Gao, G. J.; Qian, W. H.; Guo, Y. *J. Phys. Chem. C* 2007, 111, 6658.
- [29] K. Vanheusden, W. L. Warren, C. H. Seager, D. R. Tallant, J. A. Voigt, and B. E. Gnade, *J. Appl. Phys.* 79, 7983–7990 (1996)).
- [30] Xingfa Maa,^b Yanqin Wanga,¹ Mingjun Gaoa,¹ Huizhong Xua,¹ Guang Li ^c. *Catalysis Today* 158 (2010) 459–463)
- [31] X. M. Shuai and W. Z. Shen* 10.1021/jp2005716 | *J. Phys. Chem. C* 2011, 115, 6415–6422).
- [32] Jun Xu, Xia Yang, Hongkang Wang, Xue Chen, Chunyan Luan, Zongxiang Xu, Zhenzhen Lu, V. A. L. Roy, Wenjun Zhang, and Chun-Sing Lee, 10.1021/nl201934k | *Nano Lett.* 2011, 11, 4138–4143).
- [33] Lidan Wang, Dongxu Zhao, Zisheng Su and Dezhen Shen. *Nanoscale Research Letters* 2012, 7:106 doi:10.1186/1556-276X-7-106).
- [34] Y.F. Zhu, G.H. Zhou, H.Y. Ding, A.H. Liu, Y.B. Lin, Y.W. Superlattices and Microstructures 50 (2011) 549–556.
- [35] B.Q. Cao, W.P. Cai, H.B. Zeng, G.T. Duan. *Appl. Phys.* 99 (2006) 073516-1–073516-6.
- [36] N. Ashkenov, B.N. Mbenkum, C. Bundesmann, V. Riede, M. Lorenz, D. Spemann, E.M. Kaidashev, A. Kasic, M. Schubert, M. Grundmann, G. Wagner, H. Neumann, V. Darakchieva, H. Arwin, B. J. *Appl. Phys.* 93 (2003) 126-1–126-8.].

- [37] Y.F. Zhu, G.H. Zhou, H.Y. Ding, A.H. Liu, Y.B. Lin, Y.W. Dong. Superlattices and Microstructures 50 (2011) 549–556).
- [38] Powder Diffraction File JCPDS: Joint Committee for Powder Diffraction Studies File No. 05-0664 (hexagonal structure of ZnO)).
- [39] Powder Diffraction File JCPDS: Joint Committee for Powder Diffraction Studies File No. 01-089-0440 (cubic structure of CdS)
- [40] P. Nandakumar, C. Vijayan, M. Rajalakshmi, A.K. Arora, Y.V.G.S. Murti, Physica E 11(2001) 377–383.
- [41] J. Jie, G. Wang, Y. Chen, X. Han, Q. Wang, B. Xu, J.G. Hou, Appl. Phys. Lett. 86 (2005) 031909.
- [42] Chen Y W, Cahen D, Noufi R and Turner J A 1985 Sol. Cells 14 109–21
- [43] Ye H, Park H S, Akhavan V A, Goodfellow V W, Panthani M G, Korgel B A and Bard A J 2011 J. Phys. Chem. C 115 234–40
- [44] K. Inuk and W. W. Frank, J. Opt. Soc. Am., 1997, 14, 1639.
- [45] Jun Geng,ab Xiang-Dong Jiaac and Jun-Jie Zhu*a Received 7th May 2010, Accepted 22nd June 2010 DOI: 10.1039/c0ce00180e
- [46] Jayewardena C, hewaparama k p, wijewardena d l a, guruage h. [J]. Solar Energy Materials & Solar Cells, 1998, 56: 29–33.
- [47] Ryosuke Motoyoshi, Takeo Oku, Hiroki Kidowaki, Atsushi Suzuki, Kenji Kikuchi, Shiomi Kikuchi And Balachandran Jeyadevan . Journal of the Ceramic Society of Japan 118 [11] 1021-1023 2010.

Résumé

L'oxyde de zinc (ZnO) est un semi-conducteur à large gap direct (3,37 eV) qui possède de nombreuses propriétés intéressantes (piézoélectrique, optique, catalytique, chimique...). Un large champ d'applications fait de lui l'un des matériaux les plus étudiés de la dernière décennie, notamment sous forme nanostructurée.

Cette thèse est consacrée à l'élaboration de cellules photoélectrochimiques hétérostructurées sensibilisées à nanoparticules, composées d'une couche dense de germes de ZnO recouverte de nanobâtonnets de ZnO sensibilisés par nanoparticules de PbS, CdS, Cu₂O et CuO.

Les caractérisations structurales, morphologiques et optiques du ZnO nanobâtonnets et hétérostructures de ZnO/PbS, ZnO/CdS et ZnO/Cu₂O-CuO ainsi élaborées ont été réalisées par diffractométrie de rayons-X (DRX), microscopie électronique à balayage (MEB), microscopie électronique en transmission (MET), spectroscopie Raman, spectroscopie UV et catodoluminescence (CL).

La couche dense de germes de ZnO a été optimisée, afin qu'elle soit compacte, homogène et bien orientée. Les nanobâtonnets sont synthétisés par voie hydrothermale. L'influence de différents paramètres de synthèse sur la morphologie des nanobâtonnets ont également été testées. Deux méthodes permettant de modifier l'écart entre les nanobâtonnets ont également été mises au point. Les performances des cellules photoélectrochimiques varient en fonction de la longueur des nanobâtonnets, du nanoparticules utilisé, de la nature et la concentration des précurseurs.....Enfin, nous avons réussi à obtenir un rendement dépassant 4mA pour ZnO/PbS core-shell.

Mots clés : ZnO, hydrothermale, nanoparticules, nanobâtonnet, photoélectrochimie.

الملخص

عينات من أكسيد الزنك ذات بنية عصيات نانومترية و جزيئات من كبريت الرصاص و من كبريت الكاديوم و من أكسيد النحاس تم تحضيرها .

أولا : تم إعداد عصيات نانومترية باستخدام طريقة المعالجة الحرارية حيث اتخذت عصيات نانومترية لأكسيد الزنك بنية wurtzite و التي بلغ قطرها 100 نانومتر عموديا على الشريحة الزجاجية .

ثانيا : حضرت وصلة غير متجانسة من عصيات نانومترية من أكسيد الزنك حيث أحيطت بطبقة من كبريت الرصاص أو من كبريت الكاديوم أو من أكسيد النحاس وذلك باستخدام طريقة التبادل الأيوني. تؤكد نتائج المجهر الإلكتروني النافذ هذه النتائج .

إن الخاصية الضوئية للعينات تظهر بوضوح القدرة الهائلة على امتصاص الضوء في المجال المرئي بالإضافة إلى مردود الكهرباء الضوئية بالمقارنة مع النتائج المنشورة .

الكلمات المفتاحية : أكسيد الزنك , عصيات نانومترية , جزيئات نانومترية , كبريت الرصاص , من كبريت الكاديوم , من أكسيد النحاس.

Abstract

Fabrication and characterization of a heterojunction structured by CdS, PbS, CuO-Cu₂O/ZnO nanorods-array panels were presented. Firstly, ZnO nanorods-array panels were prepared by using a hydrothermal approach where wurtzite ZnO nanorods with a diameter of about 100 nm grew perpendicularly to glass substrate. Secondly, CdS, PbS, CuO-Cu₂O nanoparticles were deposited onto the surface of the ZnO nanorods-arrays by using exchange ions method, and the CdS, PbS shell/ZnO core heterojunction were thus obtained. Scanning electron microscopy and transmission electron microscopy results indicate that the CdS, PbS, CuO-Cu₂O nanoparticles can be uniformly deposited on the ZnO nanorods arrays and the thickness of the shell can be controlled through varying the number of the adsorption and reaction time. Optical property indicate that the as-fabricated heterojunction structure not only exhibits a high absorption of the incident light in visible region but also can show improved photocurrent with respect to the litterateur results.

Key words: ZnO, nanorods, nanoparticles, hydrothermal, CdS, PbS, CuO, Cu₂O.